

FEDERAL UNIVERSITY OF ESPÍRITO SANTO

TECHNOLOGICAL CENTER

POST-GRADUATE PROGRAM IN ELECTRICAL ENGINEERING

CAMILO ARTURO RODRÍGUEZ DÍAZ

DOCTORAL THESIS

**Optical Fiber Sensing for Sub–Millimeter
Intrinsically–Safe Liquid Level Monitoring**

VITÓRIA, ES, BRAZIL
2018

FEDERAL UNIVERSITY OF ESPÍRITO SANTO

DOCTORAL THESIS

**Optical Fiber Sensing for
Sub–Millimeter Intrinsically–Safe
Liquid Level Monitoring**

Author:

Camilo A. R. Díaz

Advisors:

Prof. Dr. Moisés R. N. Ribeiro

Prof. Dr. Anselmo Frizera

Prof. Dr. Paulo F. C. Antunes

*A thesis submitted in fulfillment of the requirements
for the degree of Doctor in Electrical Engineering*

in the

Telecommunications Laboratory (LABTEL)

Electrical Engineering Department

Vitória, ES, Brazil

2018

CAMILO ARTURO RODRÍGUEZ DÍAZ

Optical Fiber Sensing for Sub–Millimeter Intrinsically–Safe Liquid Level Monitoring

Thesis presented to the Post-Graduate Program in Electrical Engineering of the Federal University of Espírito Santo, as a partial requirement for the degree of Doctor in Electrical Engineering.

Approved on June 6, 2018

Prof. Dr. Moisés Renato Nunes Ribeiro – Advisor
Federal University of Espírito Santo

Prof. Dr. Anselmo Frizera – Co–Advisor
Federal University of Espírito Santo

Prof. Dr. Paulo Fernando da Costa Antunes – Co–Advisor
University of Aveiro

Prof. Dr. Jean Carlos Cardozo da Silva
Technological Federal University of Paraná

Prof. Dr. Marcelo Martins Werneck
Federal University of Rio de Janeiro

Prof. Dr. Maria José Pontes
Federal University of Espírito Santo

Prof. Dr. Carlos Eduardo S. Castellani
Federal University of Espírito Santo

Abstract

The popularization and fast growth of the optical fiber sensing technology has been stimulated in different fields where measurements of diverse physical and chemical parameters are required. Among these parameters, liquid level sensing plays an essential role in industry applications such as chemical processing, fuel storage, transportation systems, oil tanks/reservoirs, and wastewater treatment plants. In order to measure this parameter different sensing techniques based on acoustical, mechanical, electrical and electromagnetic technologies have been already proposed. Nevertheless, they suffer from intrinsic safety concerns in harsh environments, especially with corrosive, and explosive or flammable atmospheres.

Fiber optic based liquid level sensors (FOLLSs) can work in harsh environments with inherent advantageous features that only optical fiber offers, such as intrinsic safety, resistance to chemical corrosion, immunity to electromagnetic interference, electric isolation, small size, lightweight sensing heads, high accuracy and resolution, easy multiplexing, and capability for extremely remote monitoring without the need of electrical power at the measuring point.

In this context, this doctoral Thesis presents two specific optical fiber sensor technologies to measure liquid level. Both the Mach–Zehnder and Fabry–Perot interferometers are researched. The Thesis also focuses on uniform fiber Bragg grating (FBG). Since these technologies have different operation principle, the liquid level measurement was based on refractive index changes for the Mach–Zehnder sensor and based on hydrostatic pressure in the case of both the FPI and FBG sensors. Furthermore, analysis of temperature cross–sensitivity is performed with the aim to improve the pressure–based sensors performance.

Despite the FBGs provide high accurate measurements, the interrogation systems are the most important drawback for their large commercial application, due to their high cost. Therefore, a new and lower cost interrogation technique based on FPI micro–cavities was proposed as a final contribution.

Acknowledgements

I believe this work is not just a product of my own efforts, but whether the contributions, help and support of many people around me. In the First place, I would like to thanks to my advisor Prof. Dr. Moisés Renato Nunes Ribeiro, who always brought me new knowledge and new ideas during scientific discussions, with the aim to resolve conceptual and technical issues, leading to improve the quality of my manuscripts and presentations.

I wish to express my gratitude to my Co-Advisor Prof. Dr. Anselmo Frizera Neto, who encouraged me to pursue my Ph.D. degree at UFES. He aroused my interest in optical fiber sensors and introduced me at the LABTEL group, place where I met my advisor, began my researches and coursed a 75% of my Ph.D. studies. He was always available for everything I needed. I would also thank to Prof. Dr. Maria José Pontes, who gave me the opportunity to travel to Portugal, and to finish my doctorate studies in the Instituto de Telecomunicações (IT) and physic department at the universidade de Aveiro.

Special thanks to my Co-Advisor Prof. Dr. Paulo Fernando da Costa Antunes, who was a person that invited me and posteriorly support me at the IT. Thanks to him, I had the opportunity to research in the IT facilities and to participate in two research projects in the physics department at the universidade de Aveiro. Definitely, he is one of the most influential people that has improved my formation as a researcher. Furthermore, I would like to thank to the Prof. Dr. Paulo Sergio Andre de Brito, who also give the opportunity and support me at the IT. Actually, he was the first person to propose my sabbatical in the IT.

During my sabbatical I met several researchers who helped me to develop and implementing some ideas for this work. Thanks to Dr. Carlos Marques, Dr. Fátima Dominges, Dr. Nélia Alberto. In particular, I am very grateful with Dr. Cátia Leitão and MSc. Susana Novais for them special reception and friendship.

Finally, I want to thank my best friend Dr. Carlos Cifuentes who taught me the value of research, and to Ing. Arnaldo Leal-Junior who contributed substantially to my formation. I thank my parents, friends and specially to my wife Rosa Puentes for their patience, support, encouragement, understanding, and insistence enabled me to finish this Thesis.

My scholarship has been funded by the Coordination for the Improvement of Higher Education Personnel (CAPES) from Brazil and Petrobras.

Contents

Abstract	i
Acknowledgements	ii
List of Figures	x
List of Tables	xi
Abbreviations	xii
List of Symbols and Constants	xiv
Dedication	xv
1 Introduction	1
1.1 Motivation	1
1.2 Research Objectives and Contributions	5
1.3 Publications	7
1.4 Organization of the Thesis	9
2 In-Fiber Sensors: key concepts and state-of-the-art	12
2.1 Introduction	12
2.2 Definitions and Terminology	13
2.2.1 Light guiding in standard optical fiber	13
2.2.2 Fiber optic sensor classes	15
2.3 In-fiber Mach-Zehnder Interferometers	16
2.3.1 Mathematical model for MZI	17
2.4 In-fiber Fabry-Perot Interferometers	20
2.4.1 Mathematical model for FPI	21
2.5 Fiber Bragg Gratings	25

2.5.1	Mathematical model for standard FBG	25
2.5.2	FBG temperature cross-sensitivity mitigation	29
2.5.3	FBG recording	31
2.6	State-of-the-art of In-fiber Optical Sensors	32
2.6.1	In-fiber Mach-Zehnder interferometers	33
2.6.2	In-fiber Fabry-Perot interferometers	36
2.6.3	Fiber Bragg grating	38
2.7	Conclusion	42
3	Envelope-Based Technique for Liquid Level Sensors ...	43
3.1	Introduction	43
3.2	Operation Principle and Experiments	43
3.2.1	Experimental setup	44
3.3	Results	46
3.3.1	Traditional method	46
3.3.2	Proposed method	47
3.3.3	Spectrum analysis	50
3.3.4	Temperature analysis	54
3.4	Discussion	55
3.5	Conclusion	57
4	In-fiber FPI Micro-cavity	58
4.1	Introduction	58
4.2	Sensor Fabrication	58
4.2.1	The fuse effect	58
4.2.2	Micro-cavity fabrication	59
4.2.3	Strain and temperature characterization	62
4.3	Liquid Level Measurement	63
4.3.1	Diaphragm based FOLLS fabrication	63
4.3.2	Temperature dependence	64
4.3.3	Experimental setup	65
4.4	Results	66
4.4.1	Strain and temperature responses	66
4.4.2	Liquid level measurements	69
4.5	Discussion	71
4.6	Conclusion	71

5	FBG–embedded Diaphragms with Temperature Compensation	73
5.1	Introduction	73
5.2	Operation Principle and Sensor Design	73
5.2.1	FBG sensor	73
5.2.2	Diaphragm-based sensor fabrication	74
5.2.3	Sensor header fabrication	74
5.2.4	Modeling the FBG–embedded diaphragm	74
5.3	Experimental Setup	77
5.3.1	Liquid level measurement	77
5.3.2	Pressure measurement	78
5.4	Results	79
5.5	Discussion	84
5.6	Conclusion	85
6	Edge–filter Based FBG Interrogator Using an In–fiber FPI ...	86
6.1	Introduction	86
6.2	Operation Principle	87
6.3	Interrogator Experimental Implementation and Analytical Modeling	88
6.3.1	Analytical modeling	89
6.4	Experimental Apparatus for Characterization	91
6.5	Results	93
6.6	Discussion	96
6.7	Conclusions	98
7	Conclusions and Future Work	99
7.1	Summary	99
7.2	Future Work Perspectives	102
	Bibliography	104

List of Figures

1.1	Comparison between in-fiber approaches and requirements locating the Thesis' contributions.	5
2.1	(a) Step refractive index profile and geometrical of an optical fiber and (b) Scheme of the total internal reflection condition.	14
2.2	(a) Schematic of an MZI; (b) equivalent structure of the MZI in an arrangement of two different fibers: single mode fiber (SMF) and reduced core fiber (RCF).	17
2.3	Several structures of in-fiber MZI, where the dashed-dotted arrows represent the exited cladding modes or the sensor arm, and the dashed arrows represents the core mode or the reference arm.	18
2.4	Structure of an EFPI. (a) Silica medium cavity and (b) air medium cavity.	21
2.5	Schematic of the Transmission T and reflexion R waves in a Fabry-Perot Interferometer.	22
2.6	(a) transmitted and (b) reflected spectra as a function of the mirror's reflectance.	24
2.7	Operational principle of a FBG.	25
2.8	(a) Uniform FBG spectrum (b) reflectivity and FWHM as a function of the physical FBG length.	28
2.9	Wavelength shift of the Strain and temperature simulation of the uniform FBG centered at 1547 nm.	29
2.10	Basic setup to record FBG sensors.	32
2.11	MZIs based on the buoyancy effect (adapted from [85, 86]).	35
2.12	General description of the structure of the in-line MZI.	36
2.13	DEFPI liquid level sensor. (a) Elastic silicon layer diaphragm-based, (b) fused silica diaphragm-based, and (c) micro-cavity-based (adapted from [91, 92, 96]).	37

2.14	FBG-based liquid level sensors. (a) SRI-based, (b) pressure-based and (c) diaphragm-based FOLLSs (adapted from [1, 106]).	40
3.1	Fiber arrangement of three different fiber by the proposed sensor. . .	44
3.2	Schematic diagram of the interrogation setup.	45
3.3	(a) Transmission spectra and shift peak by increasing the water level; (b) peak centered at 1544.44 nm as a function of the water level. . . .	46
3.4	(a) Transmission spectra and envelope without liquid; (b) envelope shift due to different water level.	49
3.5	First peak of the spectrum envelope of 120 mm sensor length as a function of the water level.	50
3.6	(a) Spectrum and its envelope for a sensor length of 470 mm; (b) peak envelope centered at 1531.17 nm as a function of the water level. . . .	52
3.7	(a) Spectrum analysis for the wavelength shift and amplitude pattern; (b) amplitude changes for each individual peak.	52
3.8	The spectrum envelope initially centered at 1544.462 nm for different liquid levels highlighting its red-shift behavior.	53
3.9	Mean wavelength shift as a function of temperature variations with constant liquid level: (a) Peaks mean and (b) dips mean.	55
3.10	(a) Envelope spectra for several temperature values; (b) wavelength and amplitude variations of first envelope peak as a function of temperature variations with constant liquid level.	56
4.1	(a) Schematic of the setup used for the fuse effect ignition (adapted from [130])and (b) picture of recycled SMF destroyed after catastrophic fuse effect.	59
4.2	FPI micro-cavity fabrication process. Pictures took from the splicing machine FSM-40S. (a) Splicing process between a standard SMF and a fiber destroyed by the catastrophic fuse effect, (b) a cavity with drop shape after fusion splicing between the SMF and the recycled fiber, (c) splicing process between the cleaved cavity with drop shape and a standard SMF, (d) typical resulting FPI micro-cavity after splicing process.	61
4.3	Spectral characteristics of FPI sensors according to them physical size.	61
4.4	Strain setup.	63
4.5	Diaphragm process fabrication.	64

4.6	Diaphragm and the inputs of the simulation.	65
4.7	Equivalent strain on the fiber. Where the blue regions present lower strain and a red shift of the fiber color represent an increase of the strain.	66
4.8	Schematic of the liquid level setup used to test both configuration: (a) sensor immersed into the water tank and (b) sensor anchored at lateral tank wall.	67
4.9	Micro-cavity strain response: (a) Redshift spectra and (b) Peak and dip as a function of the applied strain.	68
4.10	Micro-cavity temperature response: (a) single and diaphragm configuration spectra for three different temperature values and (b) wavelength shift as a function of the applied temperature for FBG, FPI and FPI embedded into the diaphragm.	68
4.11	Wavelength shift as a function of liquid level for both configurations (a) and (b) Figure 4.8.	70
5.1	Structure of the proposed Sensor.	75
5.2	Direction of the applied pressure on the diaphragm and strain on the FBG.	76
5.3	Simulation of the liquid level sensor response from 50mm to 500mm level.	77
5.4	Schematic diagram of the experimental Setup.	78
5.5	Experimental Setup for pressure characterization.	79
5.6	Level variation from 500 mm to 50 mm by three different temperatures.	80
5.7	Sensor sensitivity of temperature over level.	80
5.8	Cross-sensitivity compensation of the temperature over the liquid level measure.	82
5.9	Characterization of maximum pressure value supported by the diaphragm-based sensor.	83
6.1	Setup for FPI-based low cost FBG interrogator. OPM: optical power meter, USB: universal serial bus, FBG: fiber Bragg grating, FPI: Fabry-Perot interferometer, TEC: thermoelectric controller.	87
6.2	In-line FPI micro-cavity: (a) FPI electronic microscopy image of x50, (b) backscattered spectrum of the FPI.	88
6.3	Spectrum of the proposed interrogation system, acquired by an OSA.	89
6.4	FPI simulation vs normalized spectra of the micro-cavity.	90

6.5	Simulation for the FBG strain variation (a) and (b) the corresponding FPI edge-filtering.	91
6.6	Temperature sensor header. FBG: Fiber Bragg grating, FPI: Fabry-Perot interferometer, PTFE: Polytetrafluoroethylene, OFS: optical fiber sensor, SMF: single mode fiber, TEC: thermoelectric controller.	92
6.7	Setup for strain characterization of the FBG sensor.	93
6.8	Temperature characterization of FPI and FBG.	94
6.9	Analytical and experimental results of Strain and temperature measurements with the proposed interrogation system.	95
6.10	(a) up temperature characterization with ASE compensation and (b) up and down temperature response using the proposed interrogator.	95
6.11	Strain comparison between two FBG sensors using the proposed interrogator.	96

List of Tables

3.1	Comparative of sensitivity and linearity of several peaks and dips.	47
3.2	Comparative of sensitivity and linearity of several envelope peaks and dips.	48
3.3	Comparative of sensitivity and linearity of several peaks and dips for temperature variations.	54
4.1	Dimension of the micro-cavities taken from both the electronic microscopy image and from the spectra.	62
4.2	Highest strain sensitivities for dips and peaks of the studied sensors in the form <i>mean</i> \pm <i>standard deviation</i>	69
4.3	Level rise and fall sensitivities of configuration (a) and (b).	70
5.1	Comparative of sensitivity and cross sensitivity of temperature and transverse pressure between several FOLLS.	84
6.1	Comparison of relevant parameters of several edge-filter schemes and the proposed approach.	97
7.1	Comparison of several parameters between the studied sensors.	102

List of Abbreviations

BBS	Broad Band Source
DEFPI	Diaphragm Extrinsic Fabry-Perot Interferometer
CFBG	Chirped Fiber Bragg Grating
EDF	Erbium Doped Fiber
EFBG	Etched Fiber Bragg Grating
EFPI	Extrinsic Fabry-Perot Interferometer
EMI	ElectroMagnetic Interference
FBG	Fiber Bragg Grating
FOLLS	Fiber Optic Liquid Level Sensor
FPI	Fabry-Perot Interferometer
FSR	Free Spectral Range
FUT	Fiber Under Test
FWHM	Full Width at Half Maximum
HCF	Hollow-Core Fiber
IFOS	Interferometric Fiber Optic Sensor
IFPI	Intrinsic Fabry-Perot Interferometer
LPG	Long Period Grating
MCF	Multi Core Fiber
MMF	Multi Mode Fiber
MZI	Mach-Zehnder Interferometer
OFDR	Optical Frequency Domain Reflectometry
OFS	Optical Fiber Sensor
OSA	Optical Spectrum Analyzer
OTDR	Optical Time Domain Reflectometry
PMF	Polarization Maintaining Fiber
POFBG	Polymer Optical Fiber Bragg Grating
RCF	Reduced-Core Fiber
RI	Refractive Index

SMF	Single Mode Fiber
SNR	Signal-to-Noise-Ratio
SRI	Surrounding Refractive Index
TCSMF	Thin Core Single Mode Fiber
TDM	Time Division Multiplexing
TFBG	Tilted Fiber Bragg Grating
TF	Thinned Fiber
UV	UltraViolet
WDM	Wavelength Division Multiplexing

List of Symbols and Constants

ω	angular frequency	rad
λ	wavelength	nm
λ_B	Bragg wavelength	nm
Λ	Bragg grating period	nm
ρ	liquid density	nm
ε	strain	
E	elastic modulus (Young modulus)	
ν_f	Poisson's ratio of the optical fiber	
h	liquid level	
θ_i	incident angle	rad
θ_c	critical angle	rad
θ	resultant angle from reflector mirrors	rad
α_{max}	maximum angle of a ray to enter the fiber	rad
γ	initial phase of plane electromagnetic waves	rad
r_{co}	radius of core fiber	μm
r	radius of the fiber	μm
n_{co}	core refractive index	
n_{cl}	cladding refractive index	
n	medium refractive index	
NA	numerical aperture	
V	V-parameter	
\vec{E}	electric field vector	
E	magnitude of electric field	N C^{-1}
k	Wavenumber	rad m^{-1}
I	intensity	W m^{-2}
L	sensor length	m
ϕ	phase delay between two electromagnetic waves	rad

δ	round-trip optical phase delay	rad
P_{11}	Pockels strain optic coefficient	
P_{12}	Pockels strain optic coefficient	
P_e	photo-elastic coefficient	
α	thermal expansion coefficient	
ξ	thermo-optic coefficient	
$\hat{\sigma}$	local detuning	
ϕ	grating phase	rad
v_n	fringe visibility	
σ	DC coupling coefficient	
ζ	detuning	
T	temperature	$^{\circ}\text{C}$
$\delta\bar{n}_{eff}$	refractive index perturbation averaged over a grating period	
c	Speed of light ($\sim 3 \times 10^8$)	m s^{-1}
g	acceleration of gravity (~ 10)	m s^{-2}

Dedicated to my wife Rosa Puentes and my family...

Chapter 1

Introduction

The popularization and fast growth of the optical fiber sensing technology has stimulated research in different areas, such as industrial, medical, aerospace, civil, and so on. Measurements of diverse physical and chemical parameters, such as liquid level, temperature, strain, pressure, deformation, refractive index, are required. Among these parameters, liquid level monitoring is an important parameter in industrial applications and it is the focus of this work. Hence, fiber optic liquid level sensors and novel interrogation techniques are presented in this Thesis throughout seven chapters.

1.1 Motivation

Liquid level sensing plays an essential role in industry applications such as chemical processing, fuel storage and transportation systems, oil tanks/reservoirs, wastewater treatment plants, among others. During years, this important parameter has been measured by traditional sensing techniques based on acoustic, mechanic, and electric technologies. Among this technologies electrical liquid-level sensors are widely utilized, however, they suffer from intrinsic safety concerns in harsh environments, especially with corrosive, and explosive or flammable atmospheres [1].

Mechanic solutions such as float sensors can handle with safety concerns with low cost devices. However, they suffer by poor resolution and their application is limited because of their vulnerability to mechanical damage and high maintenance cost. Moreover, weight and volume of the mechanical system must also be taken into consideration [2]. Radar-based sensors (using radio frequency or ultrasound waves)

are the usual solution, since the sensor head are not in direct contact with the liquid. The main drawback of this technology lies in the polluted atmosphere between the liquid and the sensor, which may induce errors in the measurement. Usually, dust and steam mixed in medium and temperature variations interfere in the reflected waves decreasing the sensors performance [2]. Besides, two relevant disadvantages are present in these traditional techniques, namely, the multiplexing capability and the long reach measurement.

As an alternative solution to liquid level measurement, optical fiber sensors (OFSs) have been the subject of intense research activity for more than four decades. The fiber optic based liquid level sensors (FOLLSs) offer numerous distinct advantages over the traditional sensing techniques. They can work in harsh environments thanks to their inherent features, such as intrinsic safety, resistance to chemical corrosion, immunity to electromagnetic interference (EMI), electric isolation (galvanic isolation). In addition, no electrical power needed at the measuring point, which are, small size, large bandwidth, lightweight sensing heads, high accuracy and resolution, easy multiplexing, and with enhanced capability for remote monitoring [3].

In recent years several FOLLS have already been proposed. Among those solutions, we can highlight the Interferometric fiber optic sensors (IFOS) and the ones based on fiber Bragg gratings (FBG) [1, 4, 5]. IFOS have attracted a lot of attention mainly due to their high sensitivity, large dynamic range, high accuracy, and their long distance sensing properties [6]. They can be classified into four types of fiber optic interferometers, namely Mach-Zehnder, Fabry-Perot, Michelson, and Sagnac [7]. As a matter of fact, FBG is the most popular OFS because its intrinsic sensing response to strain and temperature, inherent self referencing capability, linear output, high sensitivity, large dynamic range, and easily multiplexing along a single fiber [8].

IFOS and FBG sensors are usually monitored either by an optical spectrum analyzer (OSA) or a commercial FBG interrogator system. For real-time application in industry, the OSA is not suitable due to its resolution and sweep frequency; in addition to high cost, volume and weight [1]. On the other hand, commercial OFS interrogators (designed based on scanning laser or scanning filters) are able to probe the FBG spectrum with higher resolution. But, they become extremely expensive whenever hundreds scans per second are required [9].

Currently, the emerging technology of OFSs is in its early coexisting with electronic

sensing technologies which the users are already habituated. Therefore, it is an important challenge to demonstrate the superiority of the optical fiber sensors over the traditional techniques. Usually, users are not interested in the sensor technologies or techniques that are involved in the measurement. What they expected are sensor systems with good performance and reasonable price; except in the case for very specific applications where OFS are the only possible solution. Taking this into consideration, the OFS solution needs to be presented as a complete system including optical detection and signal processing electronics [10].

In this context, two relevant domains of optical fiber sensing technology are addressed in this work. First, the development of low cost interrogation techniques which implies processing signal techniques and alternative sensing schemes. Second, the development and implementation of OFSs for static and dynamic monitoring. Due to the large variety of OFSs, it is difficult to cover all of them in this Thesis report. Thus, only IFOS and FBG sensors were treated because their advantages previously presented. Among the IFOS the Mach-Zehnder and the Fabry-Perot interferometers, MZI and FPI, respectively, were addressed in the Thesis. There are also several kinds of FBG sensors such as uniform FBG, long period fiber gratings (LPG), chirped FBG (CFBG), and tilted FBG (TFGB). Since the uniform FBG is one of the most used OFSs, it was dedicated a special effort on develop a low cost interrogation system. It is important to stress once again that the main entry barrier for potential applications that could benefit from FBG is the cost of their interrogation units.

As mentioned before, the field of liquid level sensing is a very important topic in industrial applications and the participation of FOLLS is especially important for harsh environments. Therefore, liquid level measurement is the focus of this work. MZI, FPI and FBG sensors were used in order to measure this important parameter. Nevertheless, the interrogation techniques here proposed could be applied to other systems, besides liquid level measurement. In order to highlight this fact, by taking advantages of the FBG interrogation technique proposed in this work, dynamic measurement were also addressed as a final contribution of this Thesis.

Towards to measure liquid level with OFSs, several requirements need to be considered. In this work, they were divided into two groups as follow:

General requirements:

- Remote monitoring: since the researched FOLLSs are based on silica single mode fiber (SMF) and its typical attenuation is ~ 0.2 dB/km, it is expected tens of kilometers of remote monitoring.
- Intrinsically safe: this parameter is shared between the three sensors which not required high power optical sources, fulfilling this requirement. According to IEC60079-28 norm, the optical power must be lower than 15 mW [11] (See also IEC60825-1 [12]).
- Monitored liquid: in order to validate the sensors, water as the sensed liquid was selected, since its availability, homogeneous density, and easy utilization for laboratory experiments.
- Physical parameters related to liquid level: two strategies are addressed: refractive index changes due to its high sensitivity and axial strain related to hydrostatic pressure due to its simplicity.
- Liquid level resolution: it is expected to have sub-millimeter values. This parameter is related with the resolution of the interrogator device and the sensor sensitivity and stability.

Specific requirements:

- Simplicity: it is related with the fabrication process regarding the effort and/or infrastructure to have a minimally functional sensor.
- Cost effectiveness: it is related with the devices used to interrogate the sensors, usually OSA and FBG interrogators.
- Thermal cross-insensitivity: The temperature is an external factor which affects the measurement. Therefore, temperature cross-sensitivity needs to be mitigated in order to improve the sensors performance.
- Range: The measurement range is limited by the technology used and its spectral characteristics. Values around 100-fold the expected resolution are sought, which gives a 50 mm minimum measurement range if 0.5 mm liquid level resolution is defined.
- Linearity: The sensors linearity is expected to have a correlation coefficient higher than 0.95.

1.2 Research Objectives and Contributions

A detailed summary of the state-of-the-art related to FBG, MZI and FPI current sensors is reported in Chapter 2. Figure 1.1, summarizes the evaluation and relationship of the specific requirements above with characteristics from FBG, MZI and FPI current sensors. In addition, the research objectives of this Thesis are also depicted in the same diagram. As expected, the FBG is the in-fiber solution with the largest footprint in Fig. 1.1. This explains the widespread use of FBG as optical sensors. FPI has the second largest footprint but it lacks Simplicity to improve its overall performance. On the other hand, for the MZI technology Range and Linearity are important issues despite its simplicity. Finally, note that the main demand is for improving the cost effectiveness in all in-fiber sensors considered in this work. A more detailed description of each in-fiber approach along side the expected research contributions is presented as follows:

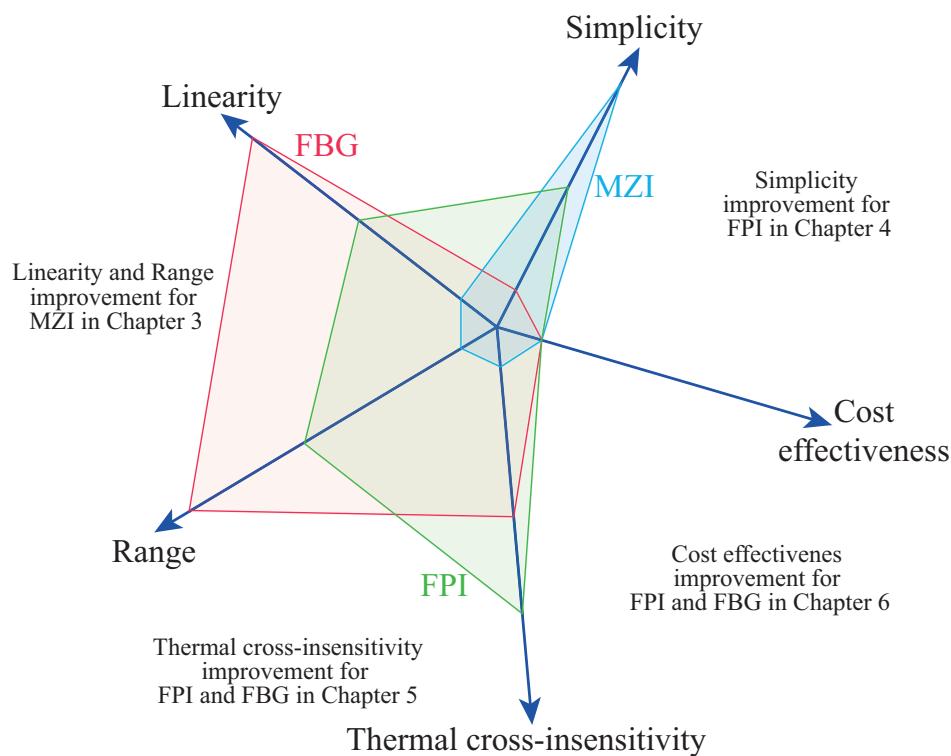


FIGURE 1.1: Comparison between in-fiber approaches and requirements locating the Thesis' contributions.

FBG: In order to fabricate the FBG a large apparatus is needed affecting its simplicity. Moreover, expensive interrogation devices are required also affecting its cost

effectiveness metric. However, Chapter 6 brings a cost-effective solution for static and dynamic interrogation of FBGs. Thermal cross-insensitivity in FBG is poor but it can be easily improved with a reference sensor as described in Chapter 5. The range for FBG diaphragm-based sensors can be conveniently adjusted according to the diaphragm thickness. Finally, FBG are well known for its linearity related with the axial strain.

MZI: In contrast with FBG, MZI sensor can be easily manufactured, however, its interrogation is still complex reducing its cost effectiveness metric. Thermal cross-sensitivity is an issue and its range is limited with poor linearity. This thesis push the last two requirements proposing a new interrogation technique for MZI in Chapter 3.

FPI: Although simple to fabricate, the current in-fiber FPIs requires expensive devices to fabricate them, this is why we assigned a medium simplicity to this devices. Chapter 4 proposes a systematic low cost FPI fabrication method. The FPI cost effectiveness is low since expensive conventional interrogator devices are used. The same technique proposed for FBG in Chapter 6 can be used to interrogate this sensors. As presented in Chapter 4 the thermal cross-insensitivity is the best when compared with other sensors, however in the diaphragm-based configuration its performance is reduced. Therefore the same technique applied for FBG in Chapter 5 brings benefits for the FPI liquid level monitoring. The range is lower that FBG since its robustness is lower, however by changing the thickness diaphragm it can be compensated. In single configuration (just the FPI) its linearity for axial strain is high, however in diaphragm configuration its performance is reduced.

The key contributions of this Thesis can be highlighted as follows:

1. The development of three optical fiber sensors based on Mach-Zehnder and Fabry-Perot interferometers and fiber Bragg gratings for liquid level monitoring [13, 14].
2. The proposition, implementation, and validation of a novel interrogation technique for MZI based on envelope spectrum analysis. This technique improved the sensitivity and allowed to increase the physical range of the measurement. Furthermore, it might be extended to another kind of sensor with similar spectral behaviour [13].

3. The proposition, implementation, and validation of diaphragm-based sensors with temperature compensation. By using a FBG-based temperature reference sensor it is possible to mitigate the temperature cross-sensitivity improving the overall sensors performance [14].
4. The proposition, implementation, and validation of a low cost interrogation system for FBG sensors. By using the FPI as an edge filter it is possible to translate the FBG spectral variations into optical power variation [15, 16].

1.3 Publications

The publications resulting from this Thesis are listed bellow:

1. **Journal** J. Martins, **C. A. R. Díaz**, P. André, P. F. C. Antunes, and R. André, "Liquid level monitoring using a fiber Fabry-Perot interferometer produced by the catastrophic fuse effect," **Under submission process**.
2. **Journal** – **C. A. R. Diaz**, C. Leitão, C. A. Marques, N. Alberto, M. F. Domingues, T. Ribeiro, M. J. Pontes, A. Frizera, P. F. C. Antunes, P. S. André, and M. R. N. Ribeiro, "IoToF: A Long-Reach Fully Passive Low-Rate Upstream PHY for IoT over Fiber", *IEEE Internet of things Journal*, **Submitted**, Mar. 2018.
3. **Journal** – **C. A. Díaz**, C. A. Marques, M. F. F. Domingues, M. R. Ribeiro, A. Frizera-Neto, M. J. Pontes, P. S. André, and P. F. Antunes, "A Cost-Effective Edge-Filter Based FBG Interrogator Using Catastrophic Fuse Effect Micro-cavity Interferometers", *Measurement*, vol. 124, pp. 486-493, Apr. 2018.
4. **Journal** – **C. A. R. Díaz**, A. G. Leal-Junior, P. S. B. André, P. F. d. C. Antunes, M. J. Pontes, A. Frizera-Neto, and M. R. N. Ribeiro, "Liquid level measurement based on FBG-embedded diaphragms with temperature compensation", *IEEE Sensors Journal*, vol. 18, no. 1, pp. 193-200, Jan. 2018.
5. **Conference** – **C. A. R. Díaz**, C. A. F. Marques, M. F. F. Domingues, M. R. N. Ribeiro, A. F. Neto, M. J. Pontes, P. S. André, and P. F. C. Antunes, "A cost-effective edge-filter-based FBG strain interrogator using catastrophic fuse effect microcavity interferometers," in *Proceedings SPIE*, vol. 10528, Jan. 2018, San Francisco, California, United States.

6. **Journal** – **C. A. R. Díaz**, C. Leitão, C. A. Marques, M. F. Domingues, N. Alberto, M. J. Pontes, A. Frizera, M. R. N. Ribeiro, P. S. B. André, and P. F. C. Antunes, "Low-cost interrogation technique for dynamic measurements with FBG-based devices", *Sensors*, vol. 17, no. 2414, Oct. 2017.
7. **Journal** – **C. A. Rodríguez**, M. R. N. Ribeiro, A. Frizera-Neto, C. E. S. Castellani, and M. J. Pontes, "Envelope-based technique for liquid level sensors using an in-line fiber Mach-Zehnder interferometer," *Applied Optics*, vol. 55, no. 34, pp. 9803-9809, Dec. 2016.

Other publications which have been the product of both the research in other directions and the interactions and collaborations with other researches during the development of this work are listed as follows:

1. **Journal** – A. Leal-Junior, A. Theodosiou, **C. Díaz**, Carlos Marques, M. J. Pontes, K. Kalli, and A. Frizera-Neto, "Polymer Optical Fiber Bragg Gratings in CYTOP Fibers for Angle Measurement with Dynamic Compensation", *Polymers*, vol 10, no. 6, Jun. 2018.
2. **Journal** – Arnaldo Leal-Junior, Anselmo Frizera, **Camilo Díaz**, Carlos Marques, Moisés Ribeiro, and Maria José Pontes, "Material features based compensation technique for the temperature effects in a polymer diaphragm-based FBG pressure sensor", *Optic Express*, **Accepted for publication**
3. **Journal** – Arnaldo G. Leal-Junior, **Camilo A. R. Díaz**, Anselmo Frizera, Carlos Marques, Moisés R. N. Ribeiro, and Maria José Pontes, "Simultaneous measurement of pressure and temperature with a single FBG embedded on a polymer diaphragm", *Optics and Laser Technology*, **submitted**, July 2018.
4. **Journal** – **C. A. Rodríguez**, A. Leal-Junior, C. A. Marques, C. Leitão, P. S. B. André, P. F. C. Antunes, M. J. Pontes, A. Frizera, M. R. N. Ribeiro, "Twist sensitivity enhancement of a distributed Bragg reflector laser by induced birefringence", **Under submission process**
5. **Journal** – A. G. Leal-Junior, A. Frizera, **C. R. Díaz**, M. R. N. Ribeiro, and M. J. Pontes, "FBG-embedded oblong diaphragms with extended dynamic range", *IEEE Sensors Letters*, vol 2, no. 2, pp. 1-4, Jun. 2018.

6. **Journal** – M. F. Domingues, **C. A. Rodriguez**, J. Martins, C. Tavares, C. Marques, N. Alberto, P. André, and P. Antunes, "Cost-effective optical fiber pressure sensor based on intrinsic fabry-perot interferometric micro-cavities", *Optical Fiber Technology*, vol. 42, pp. 56–62, May 2018.
7. **Conference** – M. de Fátima F. Domingues, **C. Rodriguez**, J. Martins, N. Alberto, C. Marques, P. André, P. Antunes, and M. F. Ferreira, "Cost effective in line optical fiber fabry perot interferometric pressure sensor", in *Advanced Photonics 2017 (IPR, NOMA, Sensors, Networks, SPPCom, PS)*, Optical Society of America, JTU4A, 2017, New Orleans, Louisiana, United States.
8. **Conference** – M. F. Domingues, J. Martins, **C. Rodriguez**, C. Tavares, N. Alberto, P. André, and P. Antunes, "Low cost intrinsic Fabry-Perot interferometric optical fiber strain and pressure sensor", in *III International Conference on Applications in Optics and Photonics (AOP 2017)*, May 2017, Faro, Portugal.
9. **Journal** – **C. A. Rodríguez**, M. R. N. Ribeiro, A. Frizera, and M. J. Pontes, "Interrogation of optical fiber based on the fusion of OFDR and TRA techniques", *Optical and Quantum Electronics*, vol 48, no. 4, p. 230, Mar. 2016.
10. **Workshop** – **C. A. R. Díaz**, M. R. N. Ribeiro, A. Frizera–Neto, and M. J. Pontes, "Incoherent OFDR for Distributed Sensor Interrogation", in *3rd Workinnova: Denmark - South America Workshop on Photonics Technologies*, vol. , pp. , Nov. 2014, Medellin, Colombia.

1.4 Organization of the Thesis

This Thesis is divided into seven chapters introduced as follows:

In this Chapter was presented the motivation of this work and its main goals. The publications and contribution are also introduced.

Chapter 2 summarizes all relevant concepts of optical fiber sensors focusing on the three sensors here studied. Definitions and terminology are addressed at the beginning. Following, mathematical models are presented for each sensor focusing on liquid level measurements. This information will be useful in the next chapters to

understand the operation principle of the optical fiber sensors as a liquid level sensors. The next three chapters are focused on the fabrication of each sensor and their application for liquid level measurement.

Chapter 3 presents a fiber optic liquid level sensor based on an in-line Mach–Zehnder interferometer. First, the operation principle of this cost-effective solution is exposed. The proposed setup is simple and inexpensive, which is based on a transparent glass pipe where it is housed the optical fiber sensor, and it is possible to change the liquid level. An external indicator is used as reference. Researching in the state-of-the-art, this kind of sensors are usually monitored by tracking one peak or dip of the optical spectrum. In this chapter is introduced a novel interrogation technique based on the envelope optical spectrum to measure liquid level changes. Two sensors with different lengths are constructed and validated with the proposed interrogation technique, enhancing the sensor sensitivity by more than an order when compared with the traditional interrogation technique.

Chapter 4 presents an in-fiber FPI as a sensor for liquid level measurement. Several techniques to fabricate the in-fiber Fabry–Perot interferometer have been already proposed in the literature, however, they are either expensive or complex for fabrication. In this chapter a cost-effective fabrication process is introduced, and the characterization for the constructed micro-cavities of strain and temperature are performed. Following, a diaphragm-based pressure sensor is implemented by embedding this optical fiber sensor into a polyurethane resin circular diaphragm where the FPIs with highest sensitivity were selected. The proposed sensor was tested in two different configurations with water as a liquid, in an acrylic reservoir. Both experiments were performed at room temperature.

Chapter 5 describes a similar approach to the previous chapter, but at this time, an uniform fiber Bragg grating sensor for liquid level monitoring is proposed. The diaphragm-based sensor fabrication is based on the same procedure as presented with the FPI micro-cavity. A mathematical model to describe the sensor behavior is presented which strongly agrees with the experimental results. The validation of the this sensor is performed in an industrial water heating/circulation plant, where both the liquid level and temperature can be tested. Due to FBG sensors are mainly affected for both temperature and strain variations, a compensation of temperature cross-sensitivity is performed enhancing the overall system performance.

Chapter 6 introduces a low-cost interrogation technique for FBG sensors. In Chapter 5 the FBG is monitored with a commercial FBG interrogator, nonetheless, interrogation systems are the most important drawback for the FBG large commercial application, due to their high cost. Therefore, the development of new, and lower cost, interrogation alternatives are essential. In Chapter 4 a FPI micro-cavity is used as a fiber optic liquid level sensor. In this chapter, this kind of micro-cavity is used as an edge-filter instead as a sensor. In this technique, FBG's spectral variations are straightforwardly translated into optical power variations and fast and inexpensive FBG interrogation is achieved.

Finally, in Chapter 7 are summarized and compared the three sensors studied in this Thesis. The main conclusions of this work and some perspectives and future research works are reported.

Chapter 2

In-Fiber Sensors: key concepts and state-of-the-art

2.1 Introduction

Optical fibers have been used in telecommunications systems since 1980 revolutionizing the communications field in the entire world, providing large amounts of information transmission with high velocities using nowadays carriers of 100 THz order along to distances of thousands of kilometers [17]. In the early 1960s the optical fiber had high losses around 1000 dB/km preventing its use in communications where the microwave systems had better performance. However, ten years after the losses decreased around 20 dB/km allowing the implementation of optical systems at a bit rate of 45 Mb/s with repeater spacings up to 10 km [18–20]. With the evolution of optical fiber fabrication techniques the losses have been drastically decreased, in addition to the advantages of technological developments to fabricate compact optical sources, new optical amplification schemes and new modulation techniques. Nowadays the communications systems based on fiber optics offer high bit rates along large distances i.e. 64 Tb/s in 340 km distance transmission [21–24].

As well as the optical fiber has been broadly used in optical communication systems, the research efforts also have been addressed to use it as a sensor since 1970 [25–27]. Parameters such as temperature, stress, strain, refractive index, pressure, liquid level, acceleration, relative humidity and almost any physical variable has been measured with optical fiber sensors (OFSs) due to the advantages that only they offers when compared with electronic sensors such as:

1. Electromagnetic immunity: the light is intrinsically immune to electromagnetic interference (EMI).
2. High resistance to high temperatures: the melting point of the silica is 1719 °C. Also OFSs can support a hundreds of °C depending on the technology used [28].
3. Galvanic isolation: No electric current travels along to the optical fiber, thus the OFSs are intrinsically safe, what makes them ideal for explosive environments [29, 30].
4. High resistance to corrosive environments: OFSs are able to support extreme conditions with high durability [31, 32].
5. Monitoring the sensors located at large distances: due to the low fiber attenuation (0.2 dB/km for standard SMF) the sensor can be located at large distances, specially in harsh and difficult-to-access environments.
6. Easy miniaturization: depending on the kind of sensor it is possible to construct OFSs of ten of μ meters volume [33, 34].
7. Multiplexing capabilities: the wavelength division multiplexing allows connecting several sensors in the same optical fiber, where each sensor can be associated to either the same variable or different variables.

On that direction, there are several types of OFSs which are based on different properties of the propagated optical signal such as intensity, phase, frequency, polarization or spectral contents. In this chapter, key concepts will be addressed, focusing on the study of the in-fiber MZI, in-fiber FPI, and FBG sensors.

2.2 Definitions and Terminology

2.2.1 Light guiding in standard optical fiber

In general terms, the optical fiber is a cylindric dielectric waveguide composed by a central core with radius r_{co} and refractive index n_{co} embedded in an outer cladding with radius r and refractive index n_{cl} , where $n_{co} > n_{cl}$ (Figure 2.1(a)). Due to the core region has a higher refractive index than the surrounding cladding region, the light beam is therefore trapped and guided into the core by means of the total internal

reflection principle, where the incidence angle (θ_i) at the core-cladding boundaries is large than the critical angle $\theta_c = \sin^{-1}(n_{cl}/n_{co})$. On the other hand, if $\theta_i < \theta_c$ the light beam will be refracted through the cladding (Figure 2.1(b)). Therefore, the fiber numerical aperture NA will define the angles of the incident light beam accepted by the fiber core, given by:

$$NA = \sin(\alpha) = \sqrt{n_{co}^2 - n_{cl}^2}, \quad (2.1)$$

where the full acceptance angle is given by 2α .

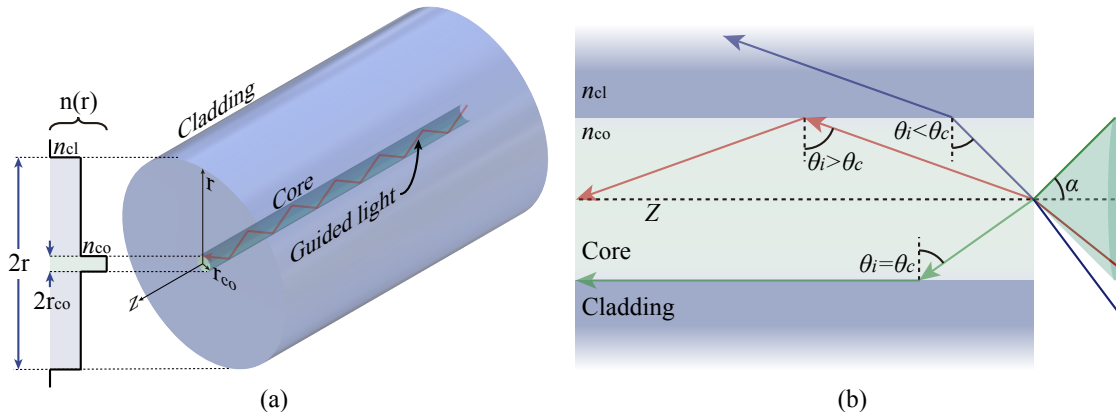


FIGURE 2.1: (a) Step refractive index profile and geometrical of an optical fiber and (b) Scheme of the total internal reflection condition.

Another important parameter used to specify the number of modes at a given wavelength (λ), mode cut off conditions, and propagation constants in an optical fiber, is the normalized frequency parameter also named the V -parameter, given by:

$$V = \frac{2\pi r_{co}}{\lambda} NA, \quad (2.2)$$

For $V < 2.405$, a singlemode is propagated through the fiber, otherwise the fiber complies the transmission of multimodes. For a large value of V , the number of modes is approximately $V^2/2$ [17]. Typical diameter values for a standard SMF are $\sim 10 \mu\text{m}$ and $\sim 125 \mu\text{m}$ for core and cladding, respectively. In the case of multi-mode fiber (MMF), there are two core diameters $\sim 50 \mu\text{m}$ and $\sim 62.5 \mu\text{m}$. The sensors here researched were implemented in SMF with some special characteristic. More details will be presented in the next chapters, where each one is focused to a specific sensor.

2.2.2 Fiber optic sensor classes

The OFSs can be classified into two general groups which are *distributed* and *quasi-distributed* sensors. The key idea is to use an optical fiber to measure one or several variables in multiples positions with a unique interrogator device, where the optical sensor measures intrinsically the spatial distribution of the measurand [35]. In other words, it is possible to conduct continuously and spatially resolved measurements along the whole length of the fiber. Techniques based on the time domain OTDR (Optical Time Domain Reflectometry), the frequency domain OFDR (Optical Frequency Domain Reflectometry), or backscattering such as Rayleigh, Raman and Brillouin have been broadly used [35–37].

The location of events using OTDR is determined by the time difference between emission and detection of backscattered light. This technique requires high peak-power pulsed laser and fast electronics in order to obtain a high resolution and long range [38]. On the other hand, OFDR relies on continuous-wave laser, which is modulated by either linear or step sweeping of RF signals [39], providing higher resolution, higher dynamic range and better signal-to-noise ratio (SNR) than OTDR. However, there are some advantages and limitations when both techniques are compared [40], i.e. resolution, measurement time, cost and complexity. The Raman based sensor is usually implemented for distributing temperature sensing due to the inherent optical intensity temperature dependence of the anti-stokes scattering component. In the case of Brillouin both scattering components, stokes and anti-stokes, are dependent on the strain and temperature [41]. More simple implementation for distributed localization of loss inducing perturbation along the optical fiber, based on backscattered and transmitted optical power have been already proposed and fusion techniques could be addressed in order to improve its resolution [33].

Among the quasi-distributed sensors technologies the fiber Bragg grating are by far the most used optical sensors to measure temperature or strain. Different techniques to record these sensors in Germanium-doped fiber or special fibers have been already proposed [42, 43], however, the most common technique to record standard FBGs is based on the phase mask technique, where a photosensitive fiber is exposed to an ultraviolet (UV) light through the phase mask, which generates an interference pattern, creating a permanent periodic refractive index changes in the core fiber, after some seconds of UV exposition. Varying parameters related with neither the

phase mask construction or the setup parameters used to record the FBG, its spectral characteristics can be modified, allowing e.g. to record several FBGs in the same fiber, which leads to an easy and inexpensive multiplexing scheme [8].

More details of the sensors studied in this work will be addressed in the next sections, where their operation principle is described, focusing in the liquid level measurement for each case, MZI, FPI and FBG.

2.3 In-fiber Mach-Zehnder Interferometers

The traditional structure of a MZI is illustrated in Fig. 2.2(a), where the optical power is splitted into two propagation arms. The reference arm is then isolated from external variations and only the sensing arm is exposed to changes of the surrounding media such as variations of temperature or strain. The signals from both arms are recombined at another coupler, which allows generating the interference signal according to the optical path length difference between the two arms [7]. An example of the equivalent MZI structure in optical fiber is depicted in Fig. 2.2(b). A simple in-fiber MZI arrange can be constructed by sandwiching a RCF segment between two SMF segments. Since, the RCF core is smaller than the SMF core segments, the optical beam is splitted into the reduced core and the cladding. Due to the core and cladding have RI slightly different are created the sensor and reference arms, which have the same physical length but optical path length different. This difference between paths creates the interference pattern in the beam combiner made by splicing the RCF with the second segment of SMF. There are two ways to induce changes in the interference pattern: (a) Changing the physical optical path by exposing the sensor to strain or temperature changes; (b) exposing the sensor region to the environment by stripping the acrylate protection layer of the sensitive component (sensor arm), the direct contact of the cladding with the surrounding medium is achieved. Therefore, if external RI changes are induced for example with liquid or gas, the effective refractive indices (ERIs) of the core and cladding modes are modified [44].

Several fabrication structures of in-line MZI are exposed in Fig. 2.3, where from (I) to (VII) are intrinsic-based MZIs and (VIII) and (IX) are extrinsic-based MZIs. The configurations here presented are composed by three components: in the extremities are the input and output beam light, usually, made with SMF. Second, the beam

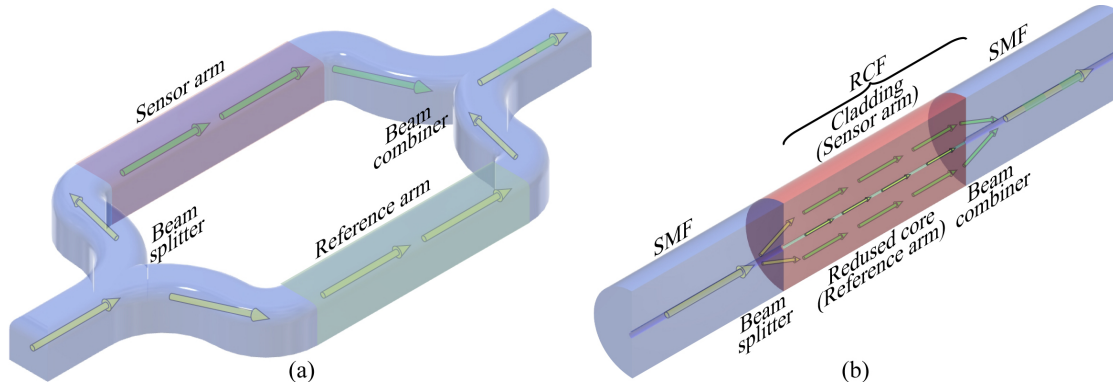


FIGURE 2.2: (a) Schematic of an MZI; (b) equivalent structure of the MZI in an arrangement of two different fibers: single mode fiber (SMF) and reduced core fiber (RCF).

splitter and beam combiner, allow to excite the cladding modes and combine such modes with the core mode, respectively, in order to generate the interference pattern. These components are elaborated with the same characteristics and can be constructed by: up-tapers (I) [44, 45], long period gratings (II) [46], multi-mode fibers (III) [4], down-tapers (IV) [47–50], core offset (V) [51, 52], small core SMF (VI) [53], collapsed air holes of PCF (VII) [54], large lateral offset (VIII) [55] and micro-cavity formed by using femtosecond laser to remove part of the core and cladding (IX) [56]. Finally, in the case of intrinsic MZIs the arms are composed by the core (reference arm) and the cladding (sensor arm). On the other hand, for (VIII) the cladding becomes the reference arm, and the air gap is the sensor arm. For (IX) the reference arm is the core and the sensor arm is the air gap. The extrinsic-based MZIs are very sensitives to RI or temperature changes but they can be constructed for very short interferometer lengths due to the large index difference between the air cavity and the optical fiber besides the optical losses [5].

2.3.1 Mathematical model for MZI

Optical phenomena such as polarization, interference and diffraction are based on the superposition of two or more electromagnetic waves in the same region of the space [57]. By assuming two plane electromagnetic waves propagating in the z direction with the same polarization, and the same angular frequency (ω), their electric fields \vec{E}_1 and \vec{E}_2 , can be represented by:

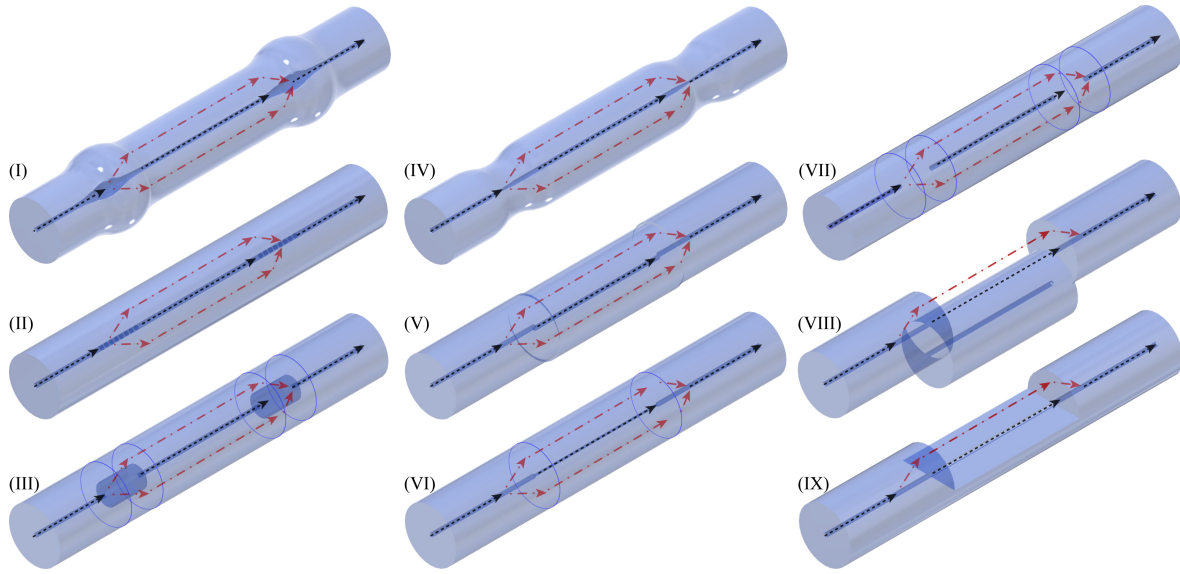


FIGURE 2.3: Several structures of in-fiber MZI, where the dashed-dotted arrows represent the exited cladding modes or the sensor arm, and the dashed arrows represents the core mode or the reference arm.

$$\vec{E}_1 = E_1 e^{i(\omega t - k_1 z + \gamma_1)} = E_1 e^{i(\omega t + \beta_1)} \quad (2.3)$$

$$\vec{E}_2 = E_2 e^{i(\omega t - k_2 z + \gamma_2)} = E_2 e^{i(\omega t + \beta_2)} \quad (2.4)$$

where $E_{1,2}$ represents the amplitude, $\gamma_{1,2}$ the initial phase, $k_{1,2} = n_{1,2} \frac{\omega}{c}$ the wave vector, where $n_{1,2}$ is the refractive index of the medium and c is the speed of light in the vacuum, t the time and $\beta_n = -k_n z + \gamma_n$, for $n = 1, 2$. According to the superposition principle, the resulting interference between two waves is obtained by:

$$\vec{E}_T = \vec{E}_1 + \vec{E}_2 = (E_1 e^{i\beta_1} + E_2 e^{i\beta_2}) e^{i\omega t} \quad (2.5)$$

Since the electromagnetic field oscillates at a very high frequency, it is not possible measuring its instantaneous value. Therefore, the current optical detectors estimate the average power per unit area and per unit time. The irradiance, also called intensity (I), is proportional to the squared amplitude of the electric field, therefore, it

can be written as:

$$I \propto \left| \vec{E} \right|^2 = \left(\vec{E}_1 + \vec{E}_2 \right) \left(\vec{E}_1 + \vec{E}_2 \right)^* = E_1^2 + E_2^2 + 2E_1E_2\cos(\phi), \quad (2.6)$$

where $\phi = \beta_2 - \beta_1$ is the phase difference. Therefore, the time-average intensity of the light is deduced as:

$$I = I_1 + I_2 + 2\sqrt{I_1I_2}\cos(\phi). \quad (2.7)$$

As above exposed, the MZI is based in the interference between two or more light beams (coming from their arms), which are combined producing the interference pattern. Therefore, the interference intensity I_{MZI} of the in-line MZI can be expressed by [58]:

$$I_{MZI} = I_{co} + \sum_m I_{cl,m} + \sum_m 2\sqrt{I_{co}I_{cl,m}}\cos(\phi_m), \quad (2.8)$$

where I_{co} and $I_{cl,m}$ are the light intensity of the core and cladding modes, respectively, ϕ_m is the relative phase difference between the core and the m th-order cladding modes, which considering air environment after its propagating through the sensor length (L) can be expressed as:

$$\phi_m = \frac{2\pi}{\lambda} (n_{eff}^{co} - n_{eff,m}^{cl}) L, \quad (2.9)$$

where n_{eff}^{co} and $n_{eff,m}^{cl}$ are the effective refractive index (ERI) of the core mode and m th cladding modes, respectively, and λ is the wavelength in vacuum. Therefore, changes over both the sensor length (L) or the environment which affects the ERI, will lead to the phase modification. If a three-layer waveguide configuration is considered, i.e. fixed sensor length but two different surrounding refractive index, namely, air and water [44], ϕ_m also will depends on the sensor arm length immersed into the liquid (\hat{l}). Thus, Eq. 2.9 can be rewritten as:

$$\phi_m = \frac{2\pi}{\lambda} \left\{ (n_{eff}^{co} - n_{eff,m}^{cl}) l + \left(n_{eff}^{\hat{co}} - n_{eff,m}^{\hat{cl}} \right) \hat{l} \right\}, \quad (2.10)$$

where $n_{eff}^{\hat{co}}$ and $n_{eff,m}^{\hat{cl}}$ are the ERI of the core mode and m th cladding modes in liquid, and $l = L - \hat{l}$. Note that Eq.(2.8) reaches its minimum when the relative

phase difference is odd multiples of π . So, applying the condition of interference minima $\phi_m = (2n + 1)\pi$, the wavelength of spectral minima λ_{min} can be deduced by

$$\lambda_{min} = \frac{2}{2n + 1} \left\{ \Delta n_{eff,m} l + \Delta \hat{n}_{eff,m} \hat{l} \right\}, \quad (2.11)$$

where n is an integer, $\Delta n_{eff,m}$ and $\Delta \hat{n}_{eff,m}$ are the effective index difference between the core mode and m th cladding modes in the air, and the core mode and m th cladding modes in the liquid, respectively.

The free spectrum range (FSR) can be defined as the wavelength spacing between two adjacent spectrum dips which determine the sensing range of the in-line MZI. From Eq.(2.11), the FSR can be approximated as [53]:

$$FSR = \lambda_{min}^2 \left\{ \Delta n_{eff,m} \hat{l} + \Delta \hat{n}_{eff,m} l \right\}^{-1}. \quad (2.12)$$

From Eq.(2.12) can be observed that the FSR is inversely proportional to the length of the sensor arm. This condition could hinder the application of such sensors to measure longer sensor lengths. In that case, the neighboring spectrum dips would be very close to each other making it impossible to track precisely which dip is being used as a reference for the measurements [59, 60].

2.4 In-fiber Fabry-Perot Interferometers

The Fabry-Perot interferometer also known as etalon was introduced in 1897 by two French physicists Charles Fabry and Alfred Perot which would eventually bear their name: the Fabry-Perot interferometer [61]. It can be considered as an optical resonator which consists of either plane or curved parallel reflecting surfaces (mirrors) separated in between at a distance l . The term etalon is often reserved for a plane-parallel plate of solid transparent material with reflecting surfaces on both sides, while interferometers (or cavities) are reserved for structures that consist of two parallel mirrors with an empty space in between [62]. The in-line term is referenced to construct the FPI structure with an optical fiber and they can be classified as intrinsic Fabry-Perot (IFP) or extrinsic Fabry-Perot (EFP) depending on the manner

how the FPI's cavity is constructed [63]. In the IFP configuration the cavity is contained within the fiber, thus, the light propagates into the fiber and the cavity with no contact of the surrounding medium, while in the EFP configuration, the cavity is external to the fiber, where the [5, 7].

During the years several means to fabricate the FPIs, and a wide range of applications have been reported [7, 64]. A simple structure of an etalon is presented in [63], where two sections of SMF are spliced to a short section of hollow-core fiber (HCF), as depicted in Figure 2.4(a). A EFPI with an air cavity is presented in [65]. Two SMF are aligned and positioned into a ferrule (hollow glass tube), with some distance of several hundred micrometers in between. The reflecting surfaces can be created from a simple cleaved SMF end face. In order to increase the fringe visibility, materials with high reflectivity such as gold or silver can be used to recover the SMF end faces [66]. Figure 2.4(b) depicts an EFPI structure, where both Lead-in and lead-out SMFs are centered and glued into a ferrule glass creating an air cavity between them.

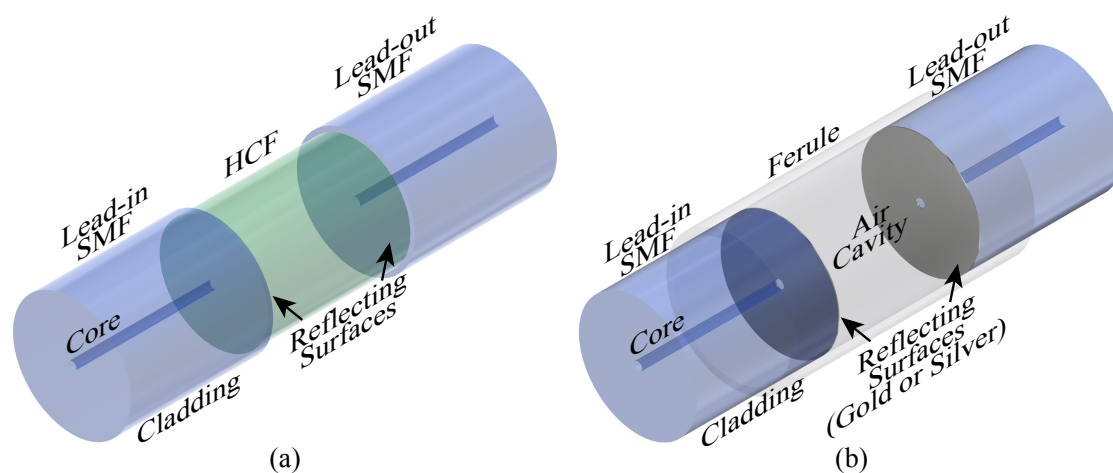


FIGURE 2.4: Structure of an EFPI. (a) Silica medium cavity and (b) air medium cavity.

2.4.1 Mathematical model for FPI

The FPI can be considered as an optical resonator which consists of a 2 plane-parallel (or curved) reflecting surfaces (mirrors) with reflectivity r separated with an empty space with refractive index n in between at a distance l and external refractive index

n' (Figure 2.5). Lets A_i be the incident plane monochromatic wave with incident angle θ_i , which is splitted in the first reflector into a reflected and transmitted waves, $\overline{A_1R_1}$ and $\overline{A_1B_1}$, respectively. This last transmitted wave, achieves the second reflector surface with an incident angle θ , which is splitted into a reflected ($\overline{B_1A_2}$) and transmitted ($\overline{B_1T_1}$) waves. This process of wave division remains inside the plate continues, and the total transmitted and reflected fields, T and R , respectively, can be calculated by adding the contributions from each of the either transmitted or reflected waves. In order to carry out this sum it is necessary to know their relative phases and amplitudes.

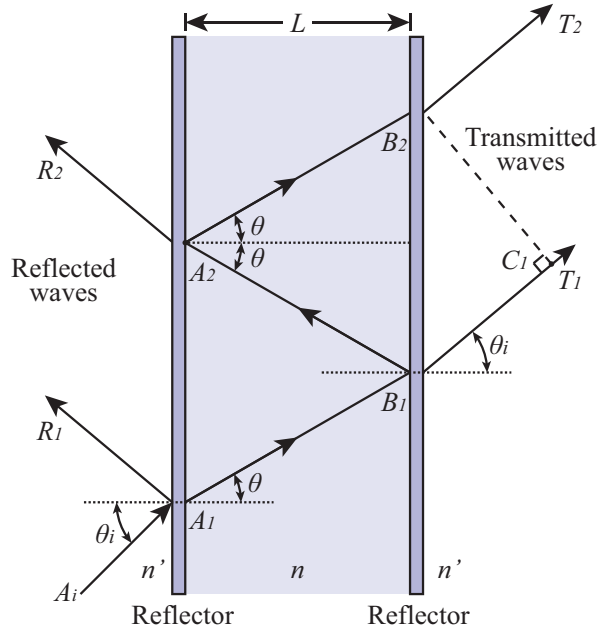


FIGURE 2.5: Schematic of the Transmission T and reflexion R waves in a Fabry-Perot Interferometer.

As observed in Figure 2.5, the transmitted waves T_1 and T_2 have the same wavefront along $\overline{B_1C_1}$, thus, the optical path length difference OPD between them can be defined as:

$$OPD = n (\overline{B_1A_2} + \overline{A_2B_2}) - n' \overline{B_1C_1}. \quad (2.13)$$

Since

$$\overline{B_1A_2} = \overline{A_2B_2} = \frac{L}{\cos(\theta)}, \quad (2.14)$$

and

$$\overline{B_1 C_1} = 2\overline{B_1 A_2} \sin(\theta) \cos\left(\frac{\pi}{2} - \theta_i\right) = 2\overline{B_1 A_2} \sin(\theta) \sin(\theta_i) \quad (2.15)$$

By applying the Snell's law $n_1 \sin(\theta_1) = n_2 \sin(\theta_2)$, and replacing Equations 2.14 and 2.15 in Equation 2.13 it is possible to obtain:

$$OPD = 2nL \cos(\theta). \quad (2.16)$$

Therefore, the round-trip optical phase delay between the backscattered signals is giving by:

$$\delta = \frac{4\pi nL \cos(\theta)}{\lambda}, \quad (2.17)$$

where $n \approx 1$ is the reflective index of the micro-cavity's material (air), λ is the wavelength under free space conditions or vacuum medium, and θ is the internal angle of incidence of the beam into the micro-cavity. Therefore, if the incidence is considered normal $\delta = 2kl$, where k is the wavenumber of propagation in the medium ($2\pi/\lambda$) and l is the distance between the reflecting surfaces. From Equation 2.17 it is observed that the phase delay depends on the wavelength, the refractive index and the cavity length.

Equation 2.18 and Equation 2.19 describes the portion of incident intensity (I_i) that is reflected (I_r) and transmitted (I_t) by the FPI, respectively.

$$\frac{I_r}{I_i} = \frac{4r \sin^2(\delta/2)}{(1-r)^2 + 4r \sin^2(\delta/2)} = R_{r,\delta}, \quad (2.18)$$

$$\frac{I_t}{I_i} = \frac{(1-r)^2}{(1-r)^2 + 4r \sin^2(\delta/2)}, \quad (2.19)$$

where r is the mirror's reflectance and no loss are considered.

Figure 2.6 depicted the transmission and reflection spectra for several values of r . The transmission peaks and reflected dips occur when $\delta = 2m\pi$, and vice-versa $\delta = (2m+1)\pi$, with m an integer.

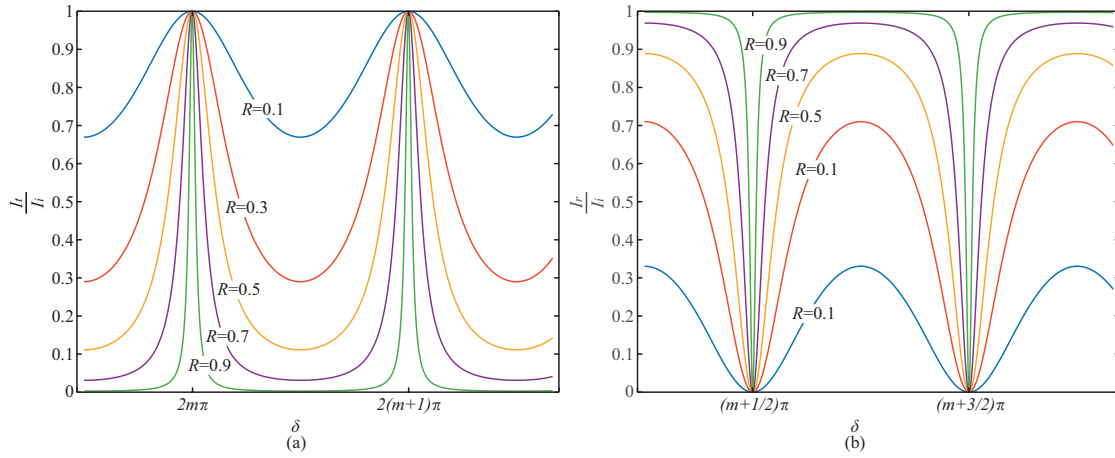


FIGURE 2.6: (a) transmitted and (b) reflected spectra as a function of the mirror's reflectance.

By taking Equation 2.17 the condition for minimum reflection (v_{min}) is given when $\delta = 2m\pi$. Therefore, it can be written as:

$$v_{min} = m \frac{c}{2nL \cos(\theta)}, \quad (2.20)$$

where $c = f\lambda$ is the velocity of light in vacuum, f is the optical frequency, and m is an integer.

The FSR can be defined as the wavelength spacing between either two adjacent spectrum dips in reflection mode, or the unity transmission (resonance) frequencies of the etalon, and is determined by:

$$\Delta v_{min} \equiv v_{min+1} - v_{min} = \frac{c}{2nL \cos(\theta)}, \quad (2.21)$$

which can be also expressed in terms of free-space wavelength, $\Delta\lambda$ as [67]:

$$|\Delta\lambda| = \left(\frac{|\Delta f|}{f} \right) \lambda = \frac{\lambda^2}{2nL} \cos(\theta) \quad (2.22)$$

2.5 Fiber Bragg Gratings

FBGs are nanometer periodical refractive index changes inscribed in an optical fiber core. When a broadband light spectrum is injected in the fiber, this optical signal will interact with the FBG, where the wavelengths that fulfill its resonance condition are reflected, while the others are transmitted (Figure 2.7). The reflected spectrum is centered at the Bragg wavelength whereas in the transmitted signal a suppression can be seen at the same wavelength [68]. The same operation principle can be observed in novel and more complex structures such as planar Bragg grating sensors [69, 70]. The FBGs provide highly accurate measurements, since wavelength is an unalterable property of the signal along the optical fibers. Therefore, optical power variations or polarization effects are not a concern for this sensors.

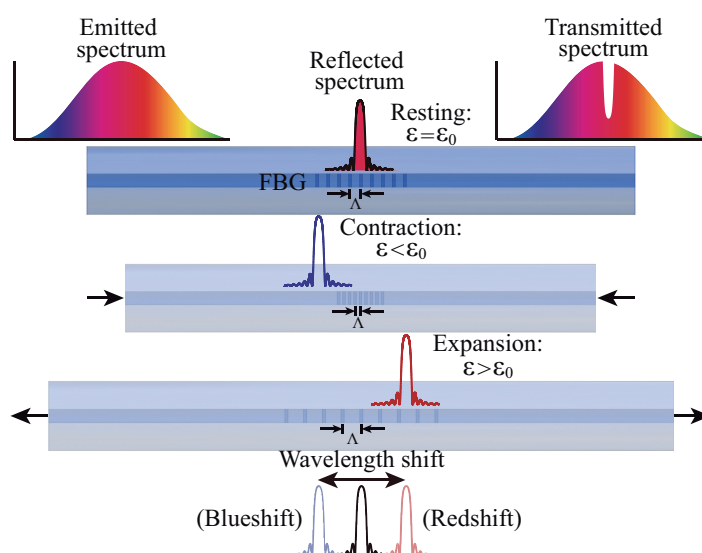


FIGURE 2.7: Operational principle of a FBG.

As presented in Figure 2.7, when the FBG is exposed to axial strain, i.e. contraction and expansion, a blueshift and redshift of the central Bragg wavelength, respectively, are expected. The same behavior is observed when the FBG is exposed to temperature changes. A more detailed analysis is presented as follow.

2.5.1 Mathematical model for standard FBG

In a FBG the Bragg wavelength λ_B is given by [71]:

$$\lambda_B = 2n_{eff}\Lambda \quad (2.23)$$

where Λ is the Bragg grating period and n_{eff} is the effective refractive index.

The wavelength shift occurs due to strain and temperature effects, affecting both Λ and n_{eff} , by elongation and thermal expansion effects, and through the elasto-optical and thermo-optic effects, respectively. Assuming a constant temperature, the relationship between principal strain components ε_x , ε_y , and ε_z and the Bragg wavelength shift is given by [72]:

$$\frac{\Delta\lambda_{B,x}}{\lambda_{B0,x}} = \varepsilon_z - \frac{n_0^2}{2} [p_{11}\varepsilon_x + p_{12}(\varepsilon_y + \varepsilon_z)], \quad (2.24)$$

$$\frac{\Delta\lambda_{B,y}}{\lambda_{B0,y}} = \varepsilon_z - \frac{n_0^2}{2} [p_{11}\varepsilon_y + p_{12}(\varepsilon_x + \varepsilon_z)], \quad (2.25)$$

where n_0 is the initial average refractive index, p_{11} and p_{12} are the Pockels strain-optic coefficients.

Due to the main deformation over the FBG sensor is in the axial direction, the Bragg wavelength shift difference between the normal components ($\Delta\lambda_{B,x} - \Delta\lambda_{B,y}$) only depends linearly on the transversal strain (ε_z). Besides, assuming that the optical fiber glass is isotropic, which implies $\varepsilon_x = \varepsilon_y = -v_f\varepsilon_z$, a simplified equation can be obtained by averaging Eq. 2.24 and Eq. 2.25 as:

$$\frac{\Delta\lambda_B}{\lambda_{B0}} = (1 - p_e)\varepsilon, \quad (2.26)$$

where $\varepsilon_z = \varepsilon$, and p_e is the effective photo-elastic coefficient given by:

$$p_e = \frac{n_0^2}{2} [p_{12} - v_f(p_{11} + p_{12})], \quad (2.27)$$

where v_f is Poisson's ratio of the optical fiber, and $p_e \approx 0.22 \cdot 10^{-6}$, $p_{11} \approx 0.113$, $p_{12} \approx 0.252$, and $v_f \approx 0.16$ are typical values for silica optical fiber.

By assuming no stress loading ($\varepsilon = 0$) the Bragg wavelength shift under temperature variations can be written as:

$$\frac{\Delta\lambda_B}{\lambda_{B0}} = (\alpha + \xi) \Delta T, \quad (2.28)$$

$$\alpha = \frac{1}{\Lambda} \frac{\partial \Lambda}{\partial T}, \quad (2.29)$$

$$\xi = \frac{1}{n_{eff}} \frac{\partial n_{eff}}{\partial T}, \quad (2.30)$$

where α is the thermal expansion coefficient of the optical fiber material (silica $\sim 0.55 \cdot 10^{-6} \text{ k}^{-1}$), ξ is the thermo-optic coefficient (varies from $\sim 3 \cdot 10^{-6}$ to $\sim 8.6 \cdot 10^{-6} \text{ k}^{-1}$) and ΔT is the temperature variation.

Finally, the Bragg wavelength variation ($\Delta\lambda_B$) as a function of both strain and temperature changes is defined as [71]:

$$\Delta\lambda_B = \lambda_B[(1 - p_e)\varepsilon + (\alpha + \xi)\Delta T], \quad (2.31)$$

The reflected amplitude spectrum for an uniform FBG sensor as a function of its grating length (L) and wavelength (λ) can be described by [73]:

$$R_{L,\lambda} = \frac{k^2 \sinh^2(\gamma L)}{\hat{\sigma}^2 \sinh^2(\gamma L) + \gamma^2 \cosh^2(\gamma L)}, \quad (2.32)$$

where k is the 'AC' coupling coefficient or local grating strength, $\hat{\sigma}$ is the general 'DC' self-coupling coefficient called the local detuning, and $\gamma = \sqrt{k^2 - \hat{\sigma}^2}$ if $k^2 > \hat{\sigma}^2$ or $\gamma = \sqrt{\hat{\sigma}^2 - k^2}$ if $k^2 < \hat{\sigma}^2$. The relation between them is given by:

$$\hat{\sigma} = \zeta + \sigma - \frac{1}{2} \frac{d\phi}{dz}, \quad (2.33)$$

$$k = \frac{\pi}{\lambda} v_n \delta n_{eff}^-, \quad (2.34)$$

$$\sigma = \frac{2\pi}{\lambda} \delta n_{eff}^-, \quad (2.35)$$

$$\zeta = 2\pi n_{eff} \left(\frac{1}{\lambda} - \frac{1}{\lambda_B} \right), \quad (2.36)$$

where $\frac{1}{2} \frac{d\phi}{dz}$ describes possible chirp of grating period, ϕ is the grating phase, $\delta \bar{n}_{eff}$ is the refractive index perturbation averaged over a grating period ('DC' index changes), v_n is the fringe visibility of the index change, σ is the DC coupling coefficient and ζ is the detuning.

Figure 2.8(a) depicts the normalized spectrum of a uniform FBG. The central Bragg wavelength is the maximum peak, as a result of the constructive interference between each contribution reflected signal for each grating. The FBG bandwidth can be determined by the wavelength spacing between the first reflection minimum on either side of the central peak. From Equation 2.32 to Equation 2.36 it is possible to observe that several parameters affect the FBG spectral characteristics. The FBG's physical length L is related with both the reflectivity and the spectrum Full Width at Half Maximum (FWHM). As presented in Figure 2.8(b) when the FBG length is increased its reflectivity increases and the FWHM is reduced. For values higher than 20 mm these functions saturate. In this case the fringe visibility was considered as maximum ($v_n = 1$) and $\delta \bar{n}_{eff} = 1 \cdot 10^{-4}$

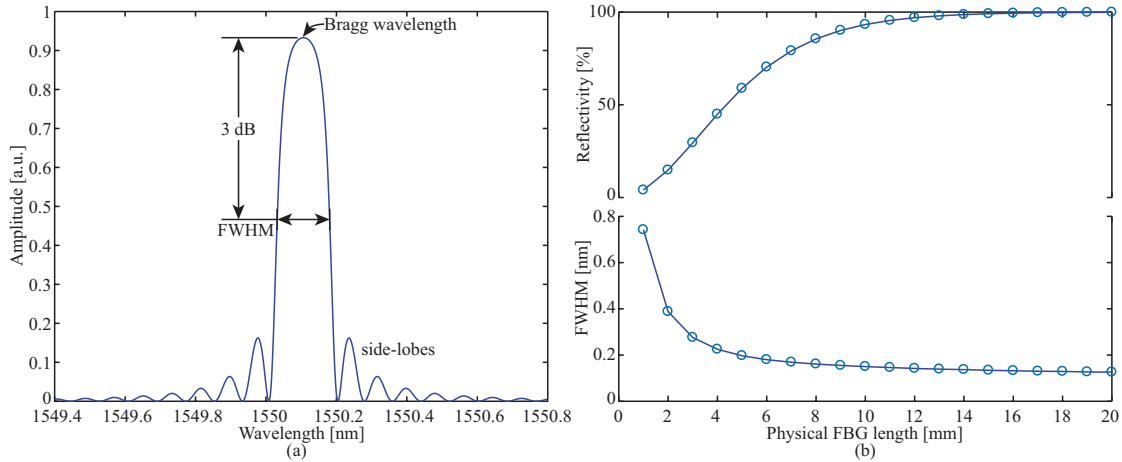


FIGURE 2.8: (a) Uniform FBG spectrum (b) reflectivity and FWHM as a function of the physical FBG length.

For uniform FBG n_{eff} and Λ are constants, ($\delta \bar{n}_{eff} = \text{constant}$), and $\phi = 0$. The parameters used in the simulations are, $L = 10$ mm, $n_{eff} = 1.458$, $v_n = 1$, $\delta \bar{n}_{eff} = 1 \cdot 10^{-4}$, and $\lambda_{B0} = 1546.92$ nm. Fig. 2.9 shows the wavelength shift as a function of the applied temperature and the applied strain (dots). Their 1st order fitting curve

(solid line) exhibits a sensitivity around $9.5 \text{ pm}/^{\circ}\text{C}$ and $1.235 \text{ pm}/\mu\text{Strain}$, respectively, as is expected by a silica FBG. The simulations were performed with both effects decoupled one each other. The strain simulation was performed from $0 \mu\text{Strain}$ to $1440 \mu\text{Strain}$ changed in $40 \mu\text{Strain}$ steps and the temperature simulation was performed from 5°C to 50°C changed in 5°C steps.

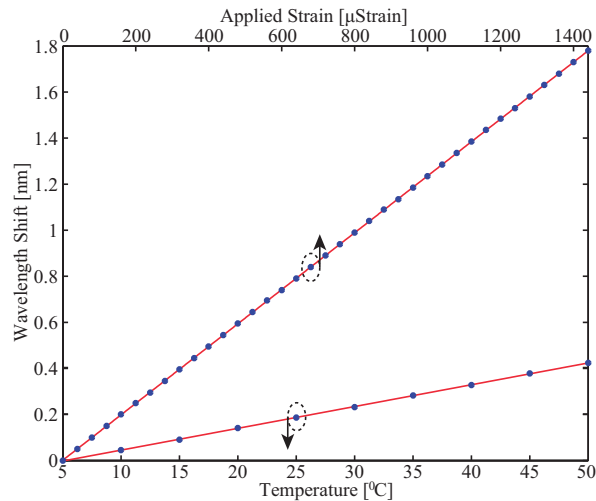


FIGURE 2.9: Wavelength shift of the Strain and temperature simulation of the uniform FBG centered at 1547 nm .

2.5.2 FBG temperature cross-sensitivity mitigation

As depicted in Equation 2.31, FBG sensors present a cross-sensitivity between the strain and temperature. If just temperature is required to measure, a simple strategy can be adopted by shielding the FBG from external perturbation [29]. On the other hand, if temperature cross-sensitivity effect needs to be decoupled to the measures, a more elaborated technique needs to be addressed. A well-known technique to handle with temperature effects, is the one based on the use of a second FBG sensor to measure the temperature changes, which in turn it is protected against external strain perturbations. An embedded FBG-based temperature sensor into the FOLLS head is reported in [74–76]. The same technique to decouple the temperature cross-sensitivity over strain and humidity using POFBG sensors is reported in [77, 78].

The terms $(1 - P_\varepsilon)\varepsilon$ and $(\alpha + \zeta)$ in Eq. 2.31 can be understood as the strain sensitivity ($k_{m,L}$) and temperature sensitivity ($k_{m,T}$), respectively. Thus, Eq. 2.23 can be rewritten to relate the initial Bragg wavelength measured ($\lambda_{B,0}$) and the temperature (Δ_T) and strain variation (Δ_ε) with the absolute Bragg wavelength variation as:

$$\lambda_{B,L} = k_{m,L}\Delta_\varepsilon + k_{m,T}\Delta_T + \lambda_{B,0}. \quad (2.37)$$

Additionally, a similar equation can be applied for the temperature sensor (Eq. 2.38). However, it is assumed that the strain does not interfere on the temperature measurements because it is decoupled of external stress.

$$\lambda_{B,T} = k_{f,T}\Delta_T + \lambda_{f,0}, \quad (2.38)$$

where $\lambda_{f,0}$ is the initial Bragg wavelength measured of the temperature sensor.

Both Eq. 2.37 and Eq. 2.38 can be written in matrix notation and the relationship between them can be obtained by:

$$\begin{bmatrix} \lambda_{B,\varepsilon} \\ \lambda_{B,T} \end{bmatrix} = \begin{bmatrix} k_{m,\varepsilon} & k_{m,T} \\ 0 & k_{f,T} \end{bmatrix} \begin{bmatrix} \Delta_\varepsilon \\ \Delta_T \end{bmatrix} + \begin{bmatrix} \lambda_{B,0} \\ \lambda_{f,0} \end{bmatrix}. \quad (2.39)$$

If the matrix coefficients, or sensitivities, are known, and the matrix \mathbf{K} is well conditioned ($\det(\mathbf{K}) \neq 0$), measurement of strain over temperature changes can be quickly determined by taking the inverse operation of matrix as:

$$\begin{bmatrix} \Delta_\varepsilon \\ \Delta_T \end{bmatrix} = \begin{bmatrix} k_{m,\varepsilon} & k_{m,T} \\ 0 & k_{f,T} \end{bmatrix}^{-1} \begin{bmatrix} \lambda_{B,\varepsilon} \\ \lambda_{B,T} \end{bmatrix} - \begin{bmatrix} \lambda_{B,0} \\ \lambda_{f,0} \end{bmatrix}. \quad (2.40)$$

As it will see in Chapters 4 and 5, a FPI and FBG embedded diaphragm sensors are able to measure liquid level. The above equations will be a useful tool to handle with temperature cross-sensitivity.

2.5.3 FBG recording

Several methods to record the FBG have been already proposed. The first observation was reported by Kenneth Hill in 1978, where an argon ion laser line at 488 nm was launched into the fiber. The backscattered optical beam product of the Fresnel reflexion at the fiber endface and the forward signal created an stationary wave, where the periodic interference pattern of peaks and valleys imprinted a permanent reflective index changes into the core fiber [79]. The launched beam is weakly reflected by each grating plane by Fresnel effect, where the each backscattered signals will join together. Constructive and destructive interference will occur depending whether the wavelength of the light beam meets the Bragg condition [42]. The changes in the core refractive index can be explained by an effect known as photosensitivity, where defects in the silica core leads to a molecular reconfiguration changing the density of the material, as well as the absorption, when it is exposed for example to ultraviolet (UV) radiation, due to electronic absorptions are in the deep UV wavelength regime [42]. Standard SMF has low Germania content leading to a low UV absorption. Hence, if it is used to record a FBG, the result will be a weak FBG when compared with germania-doped silica fibers. However, in order to improve the recording process two alternative techniques can be adopted: use a photosensitization methods (for example a hydrogenation), or use a 193 nm laser to the record the FBG [42].

The FBGs recorded in this work were based on the phase mask technique. The inscriptions of the FBG was performed in the Instituto de Telecomunicações (IT) at the Universidade de Aveiro. A photosensitive single mode fiber (ThorLabs GF1B) was used to engrave the uniform FBG sensors with a KrF UV Excimer laser emitting at 248 nm (BraggStar Industrial model from Coherent). The FBG was inscribed with 5 mJ energy pulses and a repetition frequency of 500 Hz, during 15 seconds. The setup is depicted in Figure 2.10. The kinematic mirrors allow to guide the beam light from the laser to the plano-convex optical lens, which focusing a diverging beam onto an adjustable mechanical slit. This device provide precise micrometer adjustment of two steel blades centered equally about a SM05-threaded through hole, that means, this device will define the quantity of light passing between the blades (window). In other words, it defines the physical length of the FBG. In order to create the interference pattern a phase mask is used [42]. Finally, the optical fiber is centered in front of the phase mask by mean of the 3-axis microblock compact

flexure stages, where the optical fiber is fixed over this stages with an adjustable fiber clamps. Usually all this setup is mounted on an optical table to avoid external vibrations.

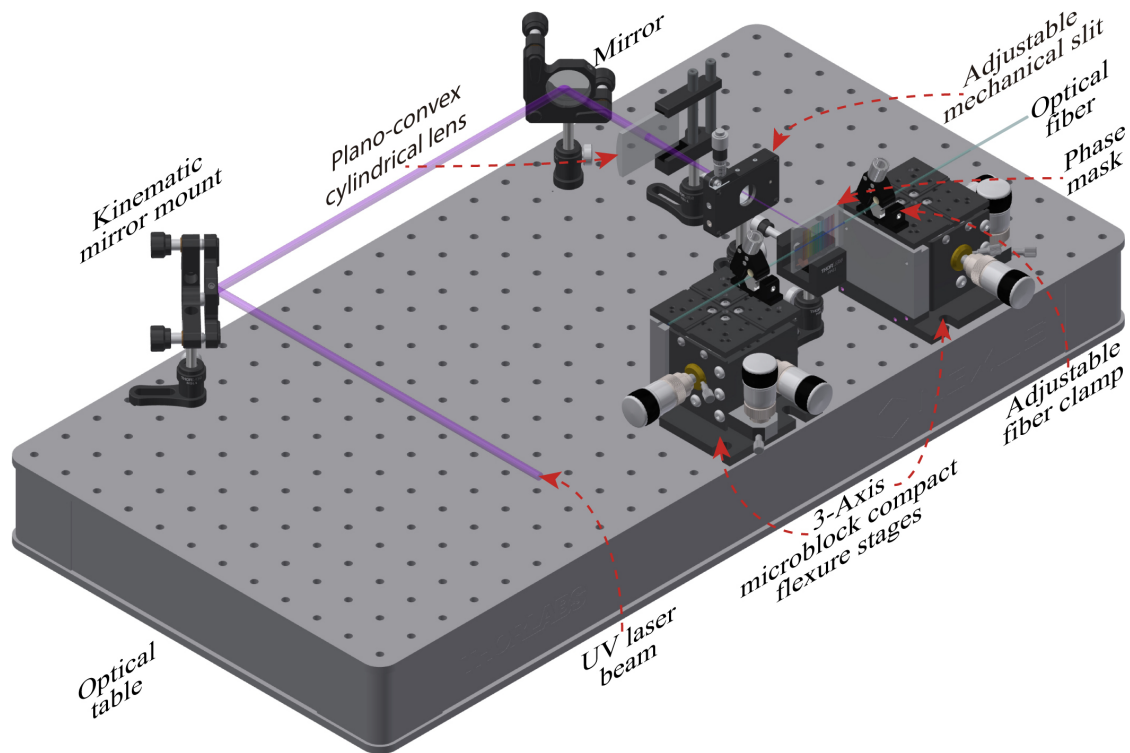


FIGURE 2.10: Basic setup to record FBG sensors.

2.6 State-of-the-art of In-fiber Optical Sensors

More than forty years have passed since the research of optical fiber sensors began. Since its early beginnings in the seventies until now, different ideas and techniques for measuring a wide variety of parameters which include temperature, pressure, level, strain, current, magnetic field, refractive index (RI), have been reported [27].

In the state-of-the-art investigations, there are several solutions to monitor liquid level based on novel structures of sensors but in general the interrogation techniques are based on the traditional schemes. They use the OSA or the FBG interrogator in order to monitor the spectra changes when the sensors are exposed to external perturbations. Therefore, alternative cost effective interrogations techniques and

processing signal are essential in the field of OFSs. Some relevant works in the literature related with this Thesis are discussed as follows.

2.6.1 In-fiber Mach-Zehnder interferometers

The in-line MZI based liquid level sensors, are structures in general of easy and cost effective fabrication. By mean of a commercial splice machine and different kinds of optical fibers they can be constructed. The principle of operation is based on the excitations of multiple cladding modes at the beginning of the optical fiber sensor which propagate within its cladding. Therefore, the cladding mode beam interferes with the core mode beam at the end of the sensor. Perturbation on either the surrounding refractive index (SRI) or the physical length of the OFS section generates changes in the interference pattern which are monitored in scattered mode and can be translated into liquid level changes.

A segment of thin core single mode fiber (TCSMF) without coating sandwiched between two standard single mode fibers SMFs is reported in [53]. Since the core diameter of SMF is much larger than that of TCSMF the cladding modes are excited at the first splice point. In order to interfere the cladding modes with the core mode, a second splice point is performed with another SMF fiber. A similar approach is presented in [4]. A section of a thinned fiber (TF) is spliced to a multi-mode fiber (MMF), these sections are, in their turn, spliced between two single-mode fibers (SMF). In this case, the MMF allows improving the fringe visibility due to more optical power is coupled into the cladding modes. In addition to measure liquid level, [4, 80, 81] expose the capability of these sensors to measure multiple parameters such as refraction index (RI), temperature and strain. References [51, 52, 81] have proposed a misaligned spliced joint to excite the cladding modes achieving higher sensitivity values.

There are several structures of sensors that allow to excite the cladding modes. The simplest way is splicing SMFs in the extremities of either a thin core fiber or an arrange of different fibers as already discussed. More structures are discussed as follow. References [60, 82] use multi-core fibers (MCF) instead TCSMF demonstrating the multipath MZI (m-MZI) has higher phase sensitivity and higher spectra visibility when compared with a two-path interferometer. [83] proposes a in-line MZI by

sandwiching a polarization maintaining fiber (PMF) between two SMFs. The sandwich structure is fabricated by waist enlarge fusion splicing. Two waist enlarged fiber tapers (up-tapers) at the extremities of the sensor is the mechanism to excites the cladding modes and create the interference pattern. As a result, liquid level measurements with high sensitivity are reported in [44]. Moreover, [45] shows the same technique for MZI and MI in-line sensors for RI measurements. A similar but expensive solution by combining femtosecond laser micromachine technique with fusion splicing is presented in [84].

Down-tapers executes the same task of the up-tapers in the in-line MZI. The difference between them is that in down-tapers the core and the cladding of the SMF are reduced instead increased [47, 48]. The SMF is heated and abruptly stretched to a small diameter such that the evanescent field partially extend from the core into the cladding exiting the cladding modes. Then, an in-line MZI can be built by cascading two abrupt tapers [49, 50]. Another technique to couple part of the light energy in the fiber core into the fiber cladding is performed through the use of LPG. It is known that an LPG is a refractive index modulation structure with the period of hundreds of micrometers. The light propagating in core mode will be coupled to the cladding modes at resonant wavelengths, resulting in several attenuation bands in transmission spectrum [46]. Therefore, by recording two LPGs separated each other it is possible to construct an in-line MZI. The first LPG will excites the cladding modes and the second LPG will mixed the core and cladding modes creating the interference pattern.

However, these sensors are becoming sensitive to both temperature and refractive index changes, thus [46] lets the LPGs out of the liquid to avoid temperature cross sensitivity. Propositions in [6, 85] present a simple solution based on the buoyancy effect for a dual-tapered fiber MZI reaching extremely high sensitive (Fig. 2.11(a)). The down-tapered based sensor is pasted onto a slice of uniform elastic plastic to form a sensing element of bending cantilever; a stick of polyamide adhered to the cantilever and drooped into the liquid tank. A more elaborated solution based on the buoyancy effect is presented in [86]. The in-line MZI is constructed by sandwiching a piece of photonic crystal fiber (PCF) between two SMFs. This sensor is attached with a special designed lever structure for liquid detection where the sensor sensitivity could be adjusted by using different ratio of two lever arms L1 and

L2 (Fig. 2.11(b)). In both cases, due to the sensors are not in contact with the liquid the temperature cross sensitivity between the liquid and the liquid level can be neglected. However, it is necessary perform the measurements in a controlled temperature environment. Furthermore, their implementation for higher liquid level measurements leads to cumbersome structures hindering their use in industrial environments.

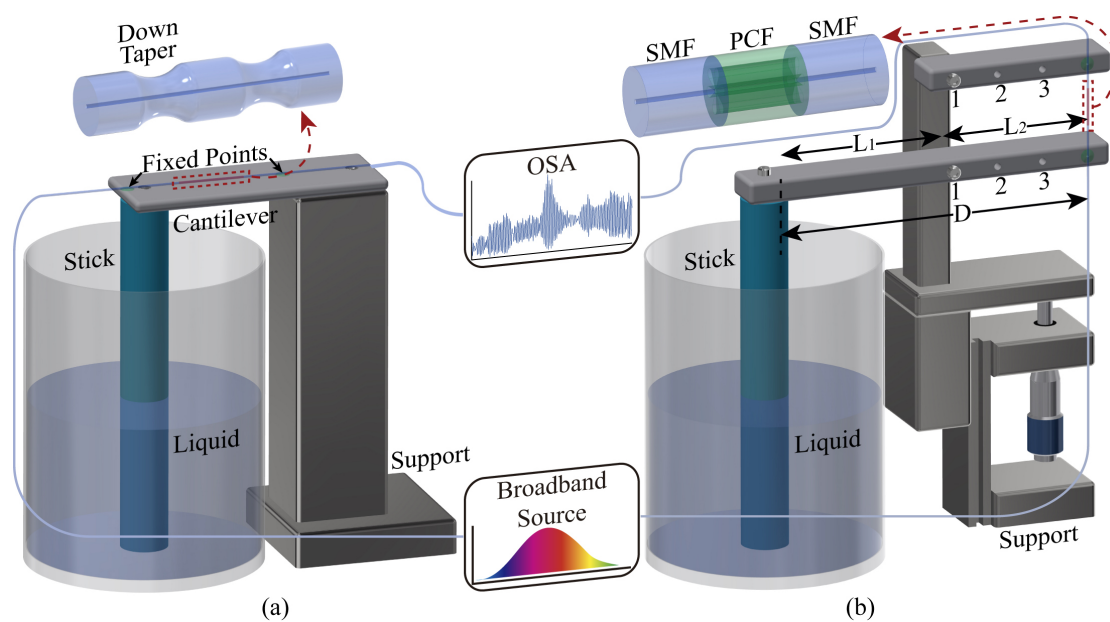


FIGURE 2.11: MZIs based on the buoyancy effect (adapted from [85, 86]).

All the structure sensors cited until now were detailed in Figure 2.3. Fig. 2.12 summarizes, several combinations of techniques and kind of fibers usually used to construct an in-line MZI. Commonly, a broad band source (BBS) is used to illuminate the in-line MZIs and an OSA is used to monitor the spectral shift in transmission mode. To allow the interaction of sensor head with the surrounding environment the coating (acrylate protection) is removed.

Finally, recent investigations show the potential of these structure sensors as a band-pass filter in ring fiber lasers [87]. Since a BBS is usually employed to illuminate the traditional in-line MZI sensors, it may cause lower intensity and thus lead to inaccurate measurement. Moreover, the 3 dB bandwidth of these sensors is large limiting their application in practice. A reliable candidate to handle with this issue is the ring fiber laser due to its unique properties of high optical intensity and narrower 3 dB bandwidth.

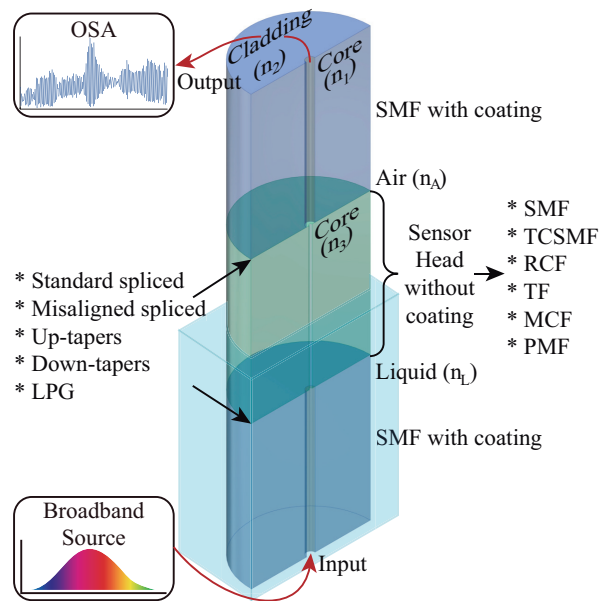


FIGURE 2.12: General description of the structure of the in-line MZI.

2.6.2 In-fiber Fabry-Perot interferometers

The FPI can be considered as an optical resonator which consists of a 2 plane-parallel (or curved) reflecting surfaces (mirrors) with reflectivity r separated with an empty space in between at a distance L . The term in-fiber is referenced to its fabrication into optical fibers. It can be largely classified into two big groups intrinsic or extrinsic, EFPI or IFPI, respectively. In the first group, the beam light goes from the fiber to the cavity which is constructed into the fiber itself. Otherwise, in the extrinsic configuration the beam light has contact with the surrounding environment. Several techniques to construct these sensors by numerous applications have been already reported [7, 88], instead, this Thesis is focused mainly on liquid level measurements.

Pressure sensors based on diaphragms EFPI (DEFPI) have been broadly used in industrial and biomedical fields due to its high sensitivity to micro-pressure, fast response, wide bandwidth, lightweight, long life time, and immunity to EMI [89]. Examples for liquid level monitoring have been previously proposed in [90, 91] where a DEFPI complex sensor head is presented (Figure 2.13(a)). A Fabry-Perot cavity is formed by a cleaved SMF end face, and an elastic silicon layer bonded by a convexity. A buffer unit that is made up of three incompressible oil cavities full of high pressure oil, allows to translate the external pressure changes, into uniform pressure in all directions over the silicon layer, leading to cavity length changes. A

similar structure with similar operation principle is presented in [92], where an all fused-silica structure for large-range measurements is composed by three main components, conform the sensor head: a lead-in SMF, a silica ferrule, and a thin silica diaphragm Figure 2.13(b). The three components are fused with CO₂ laser heating fusion bonding technology, which makes this method complex and expensive, when compared with the proposed technique in this work as it will see in Chapter 4. A similar approach is reported in [93]. The main advantages of these structures are the high sensitivity and the low cross-sensitivity temperature.

Lai et al. [94, 95] proposed a dual-pressure-sensor system comprising a FBG pressure sensor and a Fabry–Perot (FP) pressure sensor, where atmospheric pressure compensation is performed. The FP pressure sensor has a similar structure as [92]. A SMF is glued into a glass tube and a reflective diaphragm based on three-layer arrangement of polyimide, metal and SU-8 photoresist is constructed. In general way, diaphragm-based EFPI has a similar structure, with several forms to fabricate the diaphragm itself. On the other hand, the fiber can be glued or spliced with the ferrule glass, and the end fiber and the diaphragm reflecting surface can be fabricated with different reflectivity.

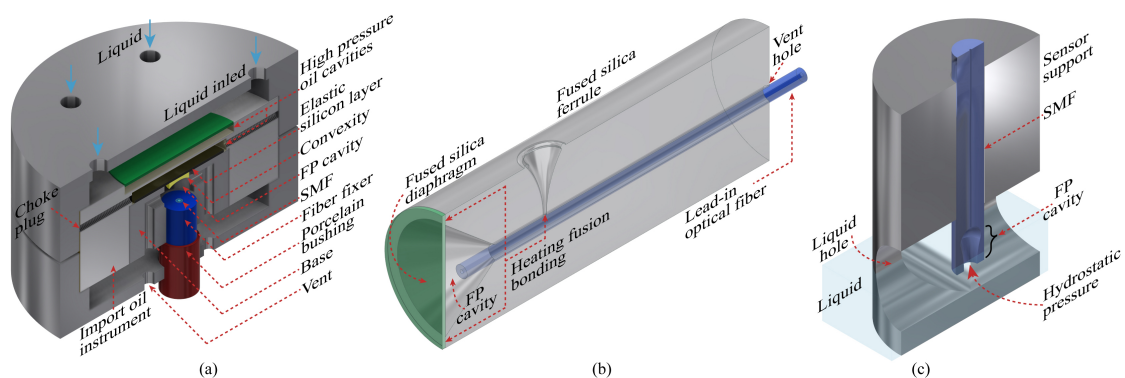


FIGURE 2.13: DEFPI liquid level sensor. (a) Elastic silicon layer diaphragm-based, (b) fused silica diaphragm-based, and (c) micro-cavity-based (adapted from [91, 92, 96]).

An alternative diaphragm structure to measure liquid level is presented in [97], where a SMF is spliced to a very tiny section of hollow core fiber (HCF) which defines the cavity length. In the HCF end face is coated a thin layer of a photopolymerizable liquid (monomer NOA65) that can be cured by ultraviolet (UV) light, closing the air cavity and creating the diaphragm face. After the sensor has been created, it is housed into a glass slide, which in turn is protected into a plastic bag to

avoid the NOA65 absorbing water vapor. As already exposed, diaphragm-based sensors measure the pressure inside liquids, and by simple mathematical relations, the level can be derived from the pressure measurements. This FPIs structure exhibits high sensitivity, However, they are difficult to fabricate, requiring expensive and complex systems. Domingues et al. [96], proposed a simple and cost effective sensor produced by the recycling of optical fibers destroyed through the catastrophic fuse effect. This sensor head is extremely simple. A SMF contents an open micro-cavity, which in turn is embedded in a metallic sensing head in order to enhance robustness (Figure 2.13(c)). In this sensor, instead to use a diaphragm reflecting surface to close the cavity, it is created an air-liquid interface exposing the micro-cavity end face directly to the liquid. Therefore, when the sensor head is immersed into liquid, the length cavity is reduced by the liquid hydrostatic pressure allowing a spectral modulation period.

2.6.3 Fiber Bragg grating

FBGs are optical fiber sensors which consist of a permanent periodic modulation of the core refractive index. When it is illuminated with a broad band source, the FBG will resonate with a specific wavelength which meets the Bragg resonance condition. As a consequence, the optical power with this specific wavelength is backscattered and the rest is transmitted. The inherent wavelength encoded output of these devices allows to encode the sensed information directly into a wavelength which is an absolute parameter. Therefore, dependence on the total source light, source power fluctuation, and losses in connections and couplers, are neglected. In addition, the wavelength encoded nature facilitates the sensor multiplexing [98]. There are several schemes to record this sensors and also several kinds of FBG sensors. The next discussion will cover relevant works in the state-of-the-art, however, silica standard FBG are the focus in this work.

Fiber Bragg grating (FBG) technology based on surrounding medium refractive index (SRI) measurement such as tilted or chirped FBGs (TFBG or CFBG, respectively) needs to be in direct contact with the liquid, and that way have a limited measurement level range due to the limitation on the grating physical length variation, and the same applies to the long period gratings (LPG). Chang et al. [99] presents an

etched CFBG. To improve the sensing sensitivity most of the cladding layer is removed, which allows exposing the evanescent wave to the surrounding medium, consequently, the sensor becomes extremely sensitive to SRI changes. Very low temperature cross-sensitivity and micro-meter liquid-level variation can be reached with this technique. Several applications for TFBG have been reported in [100]. The TFBGs couple the light from core modes to forward propagating cladding modes, where the high order modes generate a series of more dense loss bands in the transmission, which are sensitive to SRI. Mou et al. [101] presented an excessively TFBG, where the index fringes are excessively blazed, exhibits a strong birefringence property. Transmission of fast and slow axis modes are used to measure the water level, exhibiting similar behavior. As well as TFBG couples the cladding modes, the LPG has a similar behaviour. Since the cladding modes suffer from high attenuation, the transmission spectrum of a LPG consists of a series of attenuation bands centered on the core-cladding mode-coupling wavelengths [102]. It is well known that a standard FBG is not sensitive to SRI, however, if the cladding is corroded it is possible to become the FBG sensitive to SRI. An etched FBG is used in transmission mode in [103], where the minimum spectrum transmission value of FBG in air decreases while that of FBG in liquid increases, when the liquid level increases. All SRI sensors discussed above are able to measure liquid level with very high sensitivity in millimeter scales Figure 2.14(a) depicts a general structure for FBG-based SRI sensor used as a liquid level sensors.

Another approach to measure liquid level with FBG sensors for higher ranges than the SRI sensors, are the pressure-based FOLLS. Sengupta et al. [1] proposed an encapsulated etched FBG into a metal cylinder filled with silicon rubber which acts as an elastomer. The structure has two side hollows where the hydrostatic pressure is applied, leading to an axial strain over the FBG, given a measure of liquid level (Figure 2.14(b)). Embedded FBG into rubber-like material, allows translating the pressure over the sensor to wavelength shifts, therefore, several applications can be performed with this kind of structures, such as, monitorization of sea sand transport in coastal areas, dynamic vertical force monitoring for gate analyses, and so on [104, 105].

Diaphragm-based sensors also avoid to expose the FOLLS directly with the liquid when compared to SRI sensors, allowing for higher mechanical resistance [75, 94, 106, 107]. A diaphragm structure is constructed by sandwiching a FBG between

two carbon fiber composite diaphragms in [106] (Figure 2.14(c)). A pressure pump is used to simulate the liquid-level. No temperature cross-sensitivity is discussed. A similar structure sensor using a graphene diaphragm is tested in different configurations for the diaphragm and the FBG in [75]. Graphene sheets have high flexibility as well as superior heat and electrical conductivity. Thus, an ultra-thin graphene sheet used to fabricate the diaphragm improve significantly the pressure sensitivity. In this configuration a second FBG sensor is used to compensate the temperature cross-sensitivity. However, the process fabrication of the diaphragm is complex and expensive, when compared with the method presented by Marques et al. [107]. A cost-effective and high sensitivity FOLLS using a polymer optical fiber Bragg grating (POFBG) embedded in a silicone rubber diaphragm is easily constructed and validated for industrial applications [30]. The operation principle of diaphragm-based FOLLS is the same. The hydrostatic pressure over the diaphragm leads to an axial strain over the FBG sensor which in turn is translated into wavelength shift, allowing to measure the liquid level.

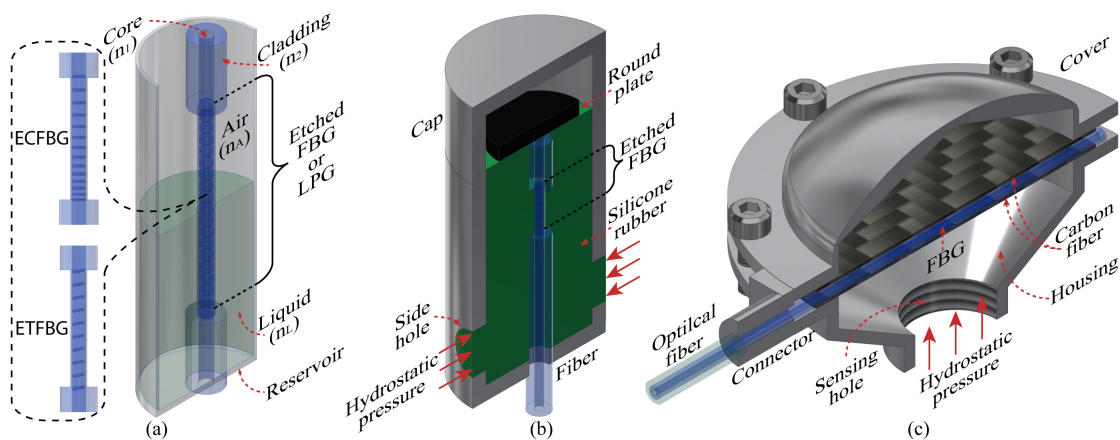


FIGURE 2.14: FBG-based liquid level sensors. (a) SRI-based, (b) pressure-based and (c) diaphragm-based FOLLSs (adapted from [1, 106]).

Interrogation techniques: An alternative technique for fast and inexpensive FBG interrogation is the frequency-to-amplitude conversion of edge-filtering, where the FBG spectrum goes through a slightly detuned broader filter. This role is usually performed by a Fabry-Perot filter. In this technique, FBG's spectral variations are straightforwardly translated into optical power variations [108, 109]. Standard FBG used as edge-filter shows high sensitivity [110–112]. A fast interrogation technique based on the fusion of both time and wavelength division multiplexing is reported

in [113], where matched FBGs-based technique is employed to interrogate several FBG sensors. The main advantages of this approach are no temperature cross-sensitivity and high sensitivity on the measurements. However, very limited dynamic range is an inherent characteristic due to the limited bandwidth offered by the matched FBGs used as edge-filter. Tilted FBG (TFBG) required a special treatment in order to get a high visibility [114]. Chirped FBG (CFBG) has higher bandwidth than standard FBGs improving the interrogation dynamic range [115]. Long period gratings exhibit large dynamic range which would limit measurement accuracy and specially the number of sensors which can be multiplexed [116–118]. In [119], it is proposed an interrogation scheme based on Erbium doped fiber (EDF) edge-detection filter, where issues related with temperature dependence are avoided. However, 10 m of EDF is required to create the filter and the dynamic range is limited to a specific spectral region (1545 nm to 1555 nm), where the slope filter is around 1 dB/nm. A tunable Mach-Zehnder interferometer (MZI)-based technique is presented in [120] and 1.5 m of MMF allows a free spectrum range (FSR) of 6 nm, with a visibility of 2.8 dB. The above techniques present edge-filters with low visibility leading to low sensitivity translated into poor signal-to-noise-ratio (SNR). A simple approach is presented in [121], in which an optical whispering gallery mode edge-filter is performed. An etched standard SMF is bended in small radius coupling the core mode to the cladding modes leading to an interference pattern between them. In this method it is expected a high sensitive to external refractive index changes because the fiber cladding (without coating protection layer) is completely exposed to external environment, which would lead to erroneous measurements as variations on the surrounding environment induce a spectrum dip shift. In addition, low sensitivity could be achieved because the large slope.

A trade-off between dynamic range and sensitivity is an inherent characteristic in the edge-filter schemes. However, filters with high visibility enhance the filter slope improving both the sensitivity and the optical SNR. A Fabry-Perot interferometer (FPI) is a good candidate to lead with this issues, nevertheless, tunable FPI are an expensive alternative when compared with the aforementioned schemes. Different techniques have been proposed to construct FPIs [122, 123]. Femtosecond (fs) laser micromachining method allows high accuracy but requires an expensive infrastructure. Diaphragm-based extrinsic FPI, or photonic crystal fiber-based fabrication are rather complicated and high cost methods. On that direction alternative solutions should be addressed.

2.7 Conclusion

In this Chapter were discussed key concepts of optical fiber sensors, which will be useful for the next chapters. First, a simple explanation of light guiding into fiber optics was introduced. Second, a general classification of OFS was addressed. Following, three sections were dedicated to explain the operation principle of the OFS and their mathematical models, which are useful tools for simulating and compare experimental results with the expected sensor response. Simulated information reveals spectral characteristics and sensor behavior, which allows to estimate several important parameters, i. e. sensor sensitivity, bandwidth, visibility, and dynamic range. Finally, a summary of the state-of-the-art related with fiber optical liquid level sensors is reported, which was focused on three specific optical fiber sensor technologies: in-fiber Mach-Zehnder and in-fiber Fabry-Perot interferometers and fiber Bragg gratings.

Chapter 3

Envelope-Based Technique for Liquid Level Sensors using In-Fiber MZI

3.1 Introduction

In this chapter a new structure of an in-line Mach-Zehnder interferometer fabricated with three different fibers for monitoring liquid level is presented. To interrogate the FOLLS a novel sensor interrogation technique based on the analysis of the overall spectrum envelope is proposed. The interference pattern created by the level sensor of 120 mm is evaluated with both the traditional (tracking either a peak or dip of the spectrum) and the proposed interrogation techniques. The result shows that the technique here proposed improves the sensitivity of the sensor by more than an order of magnitude. Furthermore, the new interrogation technique allows the length of an in-line MZI to be extended up to 470 mm maintaining high linearity and sensitivity.

3.2 Operation Principle and Experiments

The in-line MZI structure is shown in Figure 3.1 [59]. Three different fibers were spliced in order to construct the sensor arrangement. A SMF with core and cladding diameters of 10/125 μm is spliced to a reduced core fiber (RCF) with core and cladding diameters of 6/125 μm . This splice of different fiber segments has a core axial offset misalignment of 4 μm , which is made by simply setting the offset level of a default offset function of the commercial splice machine (Fujikura 70s), so that

the optical power coming from the first segment can be divided into the cladding (sensor arm) and core (reference arm) of the RCF segment. In this case, both the reference arm and the sensor arm have the same physical length but different optical paths, whereas the cladding mode detects variations of the refractive index of the surrounding environment and, as a result, interference pattern can be obtained depending on the incoming wavelength. The acrylic protection layer of the RCF is stripped in order to make it sensitive to the external medium, allowing its cladding to be in direct contact with the surrounding environment. The third segment is a multi-mode fiber (MMF) with core and cladding diameter of 50/125 μm . This element has a role to recombine both the core and cladding modes and generate interference patterns with higher contrast, this segment is spliced to the RCF segment with no misalignment. Finally, the MMF segment is spliced to another SMF in order to connectorize the sensor.

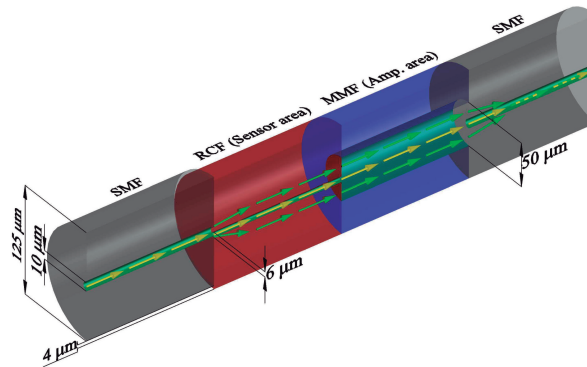


FIGURE 3.1: Fiber arrangement of three different fiber by the proposed sensor.

3.2.1 Experimental setup

The experimental setup is shown in Figure 3.2. A -2 dBm broadband source with a 3 dB bandwidth of 60 nm centered at 1550 nm is launched into the optical sensor which is placed inside an 600 mm glass pipe. The glass pipe has another input where the liquid to be measured (water) inserted or removed can be controlled. An external ruler allows to measure the liquid levels while an optical spectrum analyzer (OSA) with 30 pm resolution allows to observe the interference pattern created at the output of the sensor. By changing the liquid level, the relative phase displacement of the interfering core and cladding modes will produce a spectral shift in the

interference pattern, allowing the use of this information to detect the liquid level itself. The point to be addressed in this paper is how to interrogate such complex patterns, resulting from a core mode interfering with multiple cladding modes, to better relate their dynamics with liquid level variations.

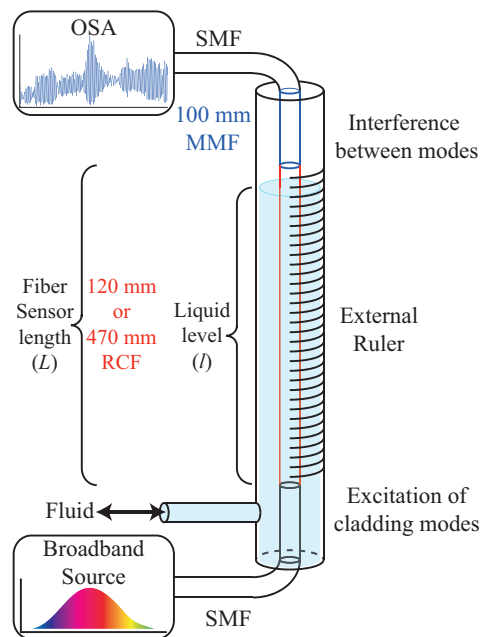


FIGURE 3.2: Schematic diagram of the interrogation setup.

In order to validate the proposed interrogation method, two experiments were performed. First, a sensor of 120 mm length was chosen and both the traditional method and the proposed method to interrogate the in-line MZI were applied. Second, a sensor of 470 mm length was chosen and only proposed method was applied. Both experiments were performed using water as the sensed liquid at room temperature $\sim 24^\circ\text{C}$.

The 120 mm sensor was selected for characterizing the temperature response. The water was heated in an external oven and then inserted into the pipette until the sensor was fully covered (level at 120 mm). This procedure was executed for each temperature measurement from 25°C to 75°C in steps of 5°C . It is important to notice that the liquid temperature was measured with a precision thermometer placed in the water when it was in the oven.

3.3 Results

3.3.1 Traditional method

Figure 3.3(a) shows the traditional method used to interrogate in-line MZI sensors. Usually, one specific dip or peak from the spectra is selected, which impose different the linearity and sensibility to the sensing process. The behavior of this dip or peak changes in wavelength according to changes in the sensor surrounding environment. The inset in Figure 3.3(a) shows a zoom on the shifts of the peak initially centered at 1544.47 nm when no liquid is present, shifting its position from right to left as expected [44], until the water fully fills the sensor (120 mm) giving a central peak at 1544.21 nm. Figure 3.3(b) shows the variation of the central wavelength of the selected peak as a function of the water level. The 1st order fitting curve $y = 1544.443 - 0.002x$ gives a sensitivity of 2 pm/mm and an acceptable sensor linearity with coefficient of determination $R^2 = 0.9234$. By increasing the fitting order the value of R^2 can be improved.

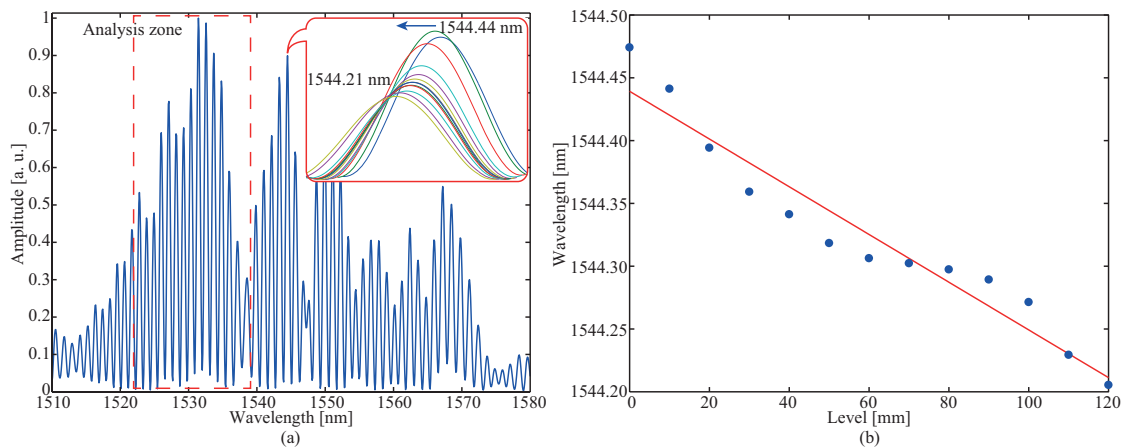


FIGURE 3.3: (a) Transmission spectra and shift peak by increasing the water level; (b) peak centered at 1544.44 nm as a function of the water level.

However, the sensor performance can be very sensitive to the chosen peak to be related to the liquid level. In order to analyze the behavior of different dips and peaks, similar measurements were performed finding similar trends in most cases. The criteria to select both the dips and peaks was the coefficient of determination higher than 0.9. The spectrum region analyzed was arbitrary selected from 1523 nm

to 1539 nm (Dashed square area in Figure 3.3(a)). The results of sensitivity for five different dips varying from 1.039 pm/mm to 2.299 pm/mm with R^2 factor from 0.902 to 0.945. In the same way, the results of sensitivity for five different peaks varying from 0.734 pm/mm to 1.752 pm/mm with R^2 factor from 0.904 to 0.967. Table 3.1 resumes the dips and peaks analysis.

TABLE 3.1: Comparative of sensitivity and linearity of several peaks and dips.

Wavelength Peaks [nm]	R^2	Sensitivity [pm/mm]	Wavelength Dips [nm]	R^2	Sensitivity [pm/mm]
1529.266	0.967	-0.828	1523.316	0.912	-1.097
1530.344	0.953	-0.734	1528.820	0.945	-1.039
1535.915	0.904	-1.627	1535.369	0.915	-1.691
1537.061	0.922	-1.584	1536.519	0.903	-1.906
1538.216	0.918	-1.752	1537.705	0.902	-2.299

3.3.2 Proposed method

The proposal method is depicted in Figure 3.4. To the best of our knowledge, this is the first time full envelope of the interference pattern in level sensing is reported. Figure 3.4(a) shows the spectrum obtained when using the same sensor of 120 mm but highlighting its envelope. Different methods to obtain the signal envelope can be used. One common algorithm is based on the detection of local maximum peaks (defined as a data samples which are larger than the two neighboring samples), and their interpolation. The algorithm here proposed is divided in two steps. First, the spectrum signal is normalized to avoid power fluctuations. Second, the maximum peaks are found and a cubic spline interpolation over local maxima separated by at least peak separation samples (np) is performed by using the envelope MATLAB function (Algorithm 1). Depending on the method of interpolation, the signal envelope error can be improved. For instance, spline interpolation allows to smooth the signal and the use of low degree polynomials can reduce the error [124].

In Figure 3.4(b) it is possible to observe that the signal envelope shift from left to right by liquid level form 0 to 120 mm with some changes in its amplitude but keeping the overall pattern similar. Different dips and peaks with similar behavior can be observed, suggesting that any of them could be chosen to sense the liquid level.

Algorithm 1 Envelope algorithm

```

1: Input: A spectrum amplitude vector  $Sp$  of size  $w$ 
2: Output: An envelope matrix of the spectrum  $Env$  of size  $w \times l$ 
3:  $sign$  : vector of sign changes
4:  $I_{Max}$  : vector of index local maxima
5:  $np$  : minimum peak separation samples
6: for  $j \leftarrow 1$  to  $l$  do
7:   read current
8:   normalize the amplitude
9:   Step1 find the sign changes of  $Sp$ :
10:   $sign \leftarrow -1$  if  $Sp_i - Sp_{i+1} < 0$   $\triangleright \forall i \in [1, 2, \dots, w]$ 
11:   $sign \leftarrow 1$  if  $Sp_i - Sp_{i+1} > 0$ 
12:  Step2 find the local maxima index:
13:   $I_{Max} \leftarrow w_i$  if  $sign_i = -1$  and  $sign_{i+1} = 1$   $\triangleright \forall i \in [1, 2, \dots, w]$ 
14:  Step3 remove peaks separated by less than  $np$ :
15:   $delete(I_{Max_i})$  if  $distance(I_{Max_i}, I_{Max_{i\pm 1}}) \leq np$   $\triangleright \forall i \in [1, 2, \dots, w']$ , where  $w' \leq w$ 
16:  Step4 perform the cubic spline interpolation:
17:   $Env_j \leftarrow interp1(I_{Max}, Sp(I_{Max}), w, spline)$   $\triangleright$  where  $interp1$  is an interpolation function
18: end for

```

The peak 1 highlighted in the rectangle region, presented the highest linearity coefficient among the peaks and it was selected for the measurements of water level. The sensitivity of the dips selected to analyze varying from 30.496 pm/mm to 33.452 pm/mm with R^2 factor from 0.913 to 0.977. Similarity, the sensitivity of the peaks varying from 30.243 pm/mm to 34.649 pm/mm with R^2 factor from 0.9 to 0.972, showing a high correlations between them and the water level. Table 3.2 shows the results of four dips and peaks analyzed from the envelope spectra presented in Fig. 3.4(b).

TABLE 3.2: Comparative of sensitivity and linearity of several envelope peaks and dips.

Wavelength Peaks [nm]	R^2	Sensitivity [pm/mm]	Wavelength Dips [nm]	R^2	Sensitivity [pm/mm]
1544.542	0.972	33.752	1538.825	0.927	31.032
1550.423	0.948	28.597	1547.772	0.977	33.452
1563.307	0.900	34.649	1555.162	0.913	30.496
1568.063	0.945	30.243	1560.972	0.929	32.293

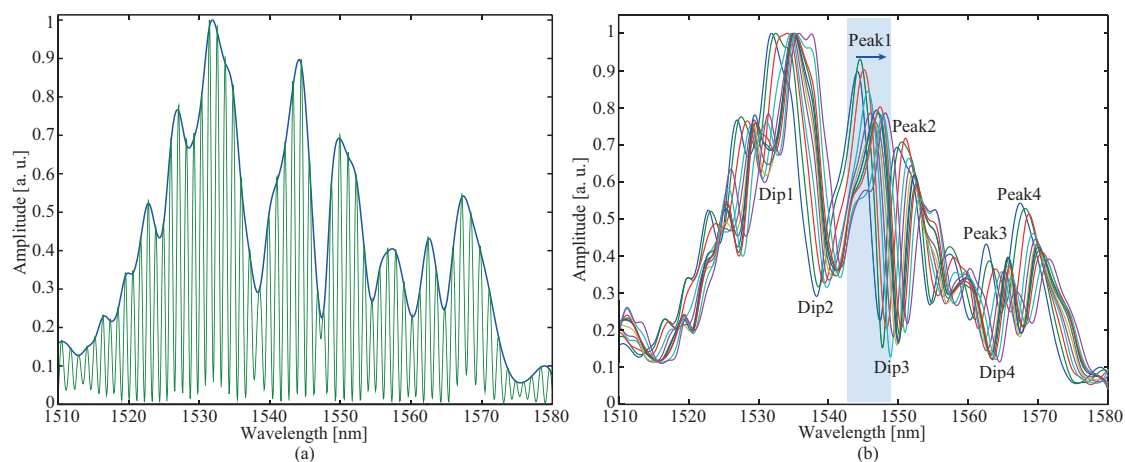


FIGURE 3.4: (a) Transmission spectra and envelope without liquid; (b) envelope shift due to different water level.

Figure 3.5 shows the wavelength of the first peak of the envelope spectrum as a function of the water level. Its 1st order fitting curve of $y = 1544.46 + 0.033x$ exhibits a sensitivity of 33.75 pm/mm with highest linearity among the envelope peaks with coefficient of determination of 0.971. Comparing the traditional method as been showed in Figure 3.3 (peak centered at 1544.47 nm) with the proposed method (Peak1 in Figure 3.5), an increment of sensitivity around 16 times higher has been achieved. By selecting other peaks of the spectrum in Figure 3.3(a) and comparing with the proposed method, the increment of sensitivity around 6 times higher can be achieved. The increment of sensitivity can be explain by the fact of the rate changes of amplitude are much higher by comparing with the wavelength shift used in the traditional method. So, this amplitude changes induces a faster wavelength shift of each envelope peak given higher sensitivity by comparing with a single peak spectrum.

In order to track both dips or peaks, a windowing technique was performed and each component was analyzed separately. Two parameters were obtained. The minimum or maximum value for dips or peaks respectively, and its wavelength which is related with the liquid level. The window dimension was selected according to the maximum shift of each dip or peak. Algorithm 2 shows the windowing process. Three important contributions can be found. First, less information or sampling rate is necessary to obtain the envelope spectrum, which implies simpler detectors. Second, due to only highest amplitude values are considered, the signal-to-noise

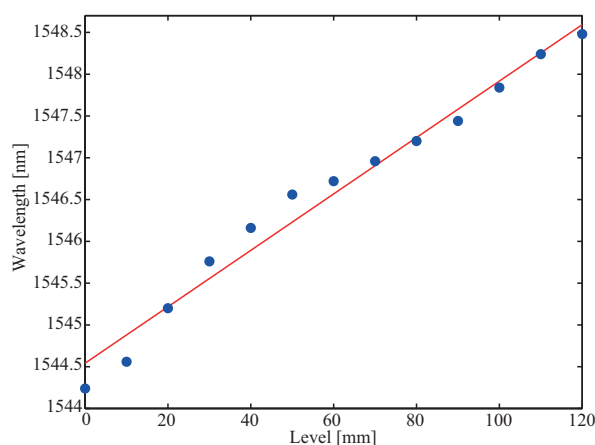


FIGURE 3.5: First peak of the spectrum envelope of 120 mm sensor length as a function of the water level.

ratio (SNR) is improved. Finally, the proposed algorithm has a low computational complexity, which could simplify its real time implementation.

Due to the fact that the fringes of the interference pattern get closer by increasing the fiber length, the traditional interrogation method limits the sensor to work only with short lengths. The proposed method based on the analysis of the spectrum envelope allows measurements to be done over longer lengths. This can be seen in Figure 3.6(a) where the spectrum and the envelope for a sensor of length of 470 mm is shown. The peak envelope centered at 1531.17 nm was used to measure the water level. This peak was chosen by experimentally comparing the sensitivities of all the peaks of the envelope and choosing the highest one which still maintained a high level of linearity. The result can be seen in Figure 3.6(b) where the obtained sensitivity is 17.17 pm/mm showing a R^2 factor of 0.996 confirming its high level of linearity.

3.3.3 Spectrum analysis

In order to explain the fact that the spectrum envelope peak centered at 1544.462 nm (Figure 3.5) shifts as opposed to the single peak spectrum shown in Figure 3.3, the spectrum section from 1540 nm to 1547 nm was selected. Figure 3.7(a) shows two important characteristics which are cyclic along the complete spectrum when the liquid level is increased from 0 to 120 mm. First, it is observed that the wavelength of each dip or peak shifts from right to left. Additionally, it can be seen that both

Algorithm 2 Level algorithm

```

1: Input: An envelope matrix  $Env$  of size  $w \times l$ , and a wavelength vector  $wl$  of size
    $w$ 
2: Output A wavelength shift vector  $Level$  of size  $l$ 
3:  $\omega_{L,R}$  : left and right window bound
4:  $I_{Max,Min}$  : vector of index local maxima or minima
5: for  $j \leftarrow 1$  to  $l$  do
6:   read current
7:   Step1 define the window ( $\omega_L \leq \omega \leq \omega_R$ ):
8:    $\omega \leftarrow Env_i - \omega_L$  to  $Env_i + \omega_R$   $\triangleright$  Where  $i$  is defined like the central wavelength
   by both peak or dip
9:    $Env_w \leftarrow Env * \omega$   $\triangleright \forall i \in [1, 2, \dots, w]$ 
10:  Step2 find the sign changes of  $Env_w$ :
11:   $sign \leftarrow -1$  if  $Env_{\omega_i} - Env_{\omega_{i+1}} < 0$   $\triangleright \forall i \in [1, 2, \dots, w]$ 
12:   $sign \leftarrow 1$  if  $Env_{\omega_i} - Env_{\omega_{i+1}} > 0$ 
13:  Step3 find the local maxima and minima index:
14:   $I_{Max} \leftarrow w_i$  if  $sign_i = -1$  and  $sign_{i+1} = 1$ 
15:   $I_{Min} \leftarrow w_i$  if  $sign_i = 1$  and  $sign_{i+1} = -1$   $\triangleright \forall i \in [1, 2, \dots, w']$  where  $w' \leq w$ 
16:  Step4 extract the wavelength information:
17:   $Level_{peak_j} \leftarrow wl(I_{Max})$  or  $Level_{dip_j} \leftarrow wl(I_{Min})$ 
18: end for

```

sensitivity and linearity of the sensor are depending on the dip or peak selected to measure the liquid level. It can be seen that P1 has higher sensitivity among all peaks visualized (upper blue-shift arrow). In addition to the wavelength blue-shift amplitude changes of the peaks are also observed, which are represented by dotted arrows. Each peak has a different amplitude pattern which can be increasing, decreasing or a combination of both.

Figure 3.7(b) shows the amplitude changes for each peak as a function of different liquid levels. It can be observed that P1 begins at 0.6 and as the liquid level increases to 50 mm it value decreases to 0.35. After that, its amplitude increases to 0.65 which is higher than its initial value. P2 begins at 0.7 and decrease to 0.35 as the liquid level increases to 100 mm, and after that its amplitude increases. P3 is always decreasing. Finally P4, P5 and P6, have a similar behavior, firstly increasing and after an increase on the liquid level of 10 mm, 20 mm and 70 mm respectively, their amplitudes decrease. As can be seen, P4 has the highest amplitude among the peaks for liquid levels in the range from 0 mm to 20 mm, which is replaced by P5 when the liquid level is in a range from 20 mm to 40 mm. After a liquid level of 40 mm P6

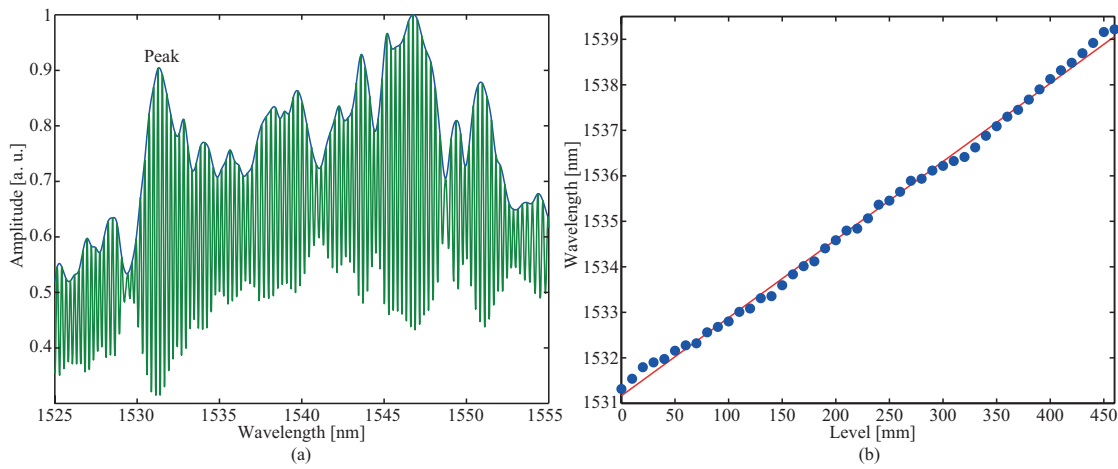


FIGURE 3.6: (a) Spectrum and its envelope for a sensor length of 470 mm; (b) peak envelope centered at 1531.17 nm as a function of the water level.

shows the maximum amplitude value. Since the envelope technique is based on the interpolation of the maximum local peaks, this relationship between the changes of each peak amplitude gives rise to the red-shift of the envelope showed in Figure 3.5.

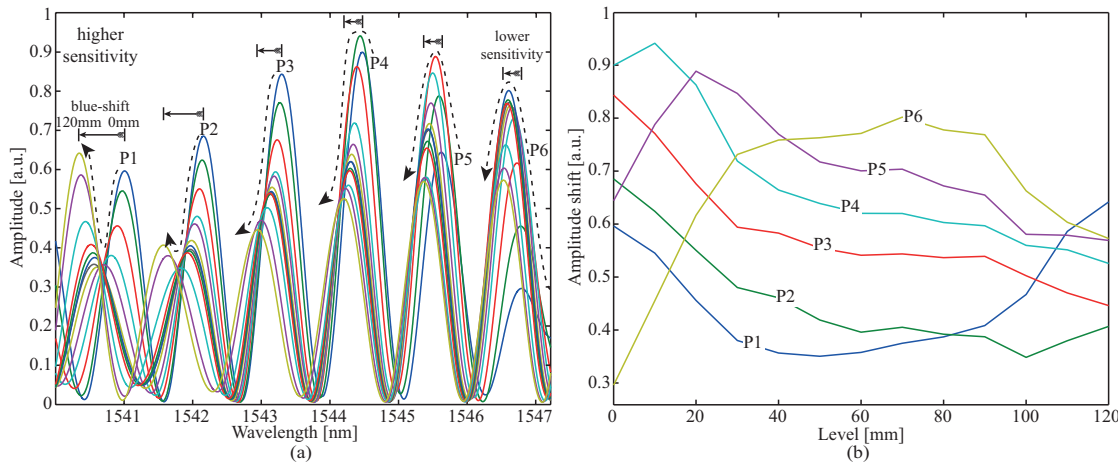


FIGURE 3.7: (a) Spectrum analysis for the wavelength shift and amplitude pattern; (b) amplitude changes for each individual peak.

Figure 3.8 shows the influence of each peak amplitude over the envelope spectrum. When the liquid level is at 0 mm it is observed that P4 has the maximum amplitude value among the peaks, and the interpolation between the peaks generates the overall envelope with a peak centered at 1544.24 nm. For liquid levels increasing from 0 mm to 20 mm, the amplitude of P1 to P4 decrease, while P5 and P6 experience an increase in their amplitudes, making P5 the highest peak in this range. By

interpolating the peaks we obtain the envelope with peak centered at 1545.21 nm. Finally, varying the liquid level from 20 to 40 mm, P1 to P5 decrease and P6 increases, resulting on the peak of envelope to shift to a wavelength at 1546.16 nm. As was mentioned before, this amplitude changes are cyclic for the whole spectrum, causing the observed red-shift in the envelope center peak to appear.

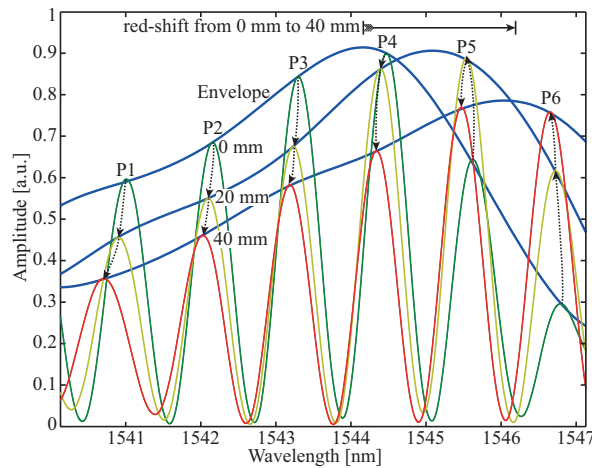


FIGURE 3.8: The spectrum envelope initially centered at 1544.462 nm for different liquid levels highlighting its red-shift behavior.

The behavior of the spectrum peak amplitudes can be attributed to the complex interaction between different modes, where each mode has a different light path, sensitivity and phase. Since all modes are recombined at the end of the sensor, and its cumulative phase is sensitivity to ERI changes (Equation (2.10)), or in other words water level changes, the superposition of the modes produce a multi-path interference and form a resultant spectrum with peaks of different amplitudes [60]. Moreover, by increasing the water level less higher order modes are expected to recombine at the end of the interferometer [44]. This is due to the fact that the ERI of the water is closer to the cladding ERI than the air ERI, enabling less higher order modes propagating forward into the liquid, affecting its spectrum amplitude [125].

By comparing the relative measurements between the peaks wavelength shift and the peak amplitude changes, it can be observed that the rate of peaks amplitude changes are higher and faster when the liquid level is increased. Unfortunately, the peaks amplitude changes are non linear and are dependent of the broadband source stability, precluding the use of each individual peak as a benchmark to measure the liquid level. Nevertheless, this amplitude changes are quasi-periodic throughout the total spectrum, and induce a wavelength shift of the envelope spectrum from

left to right as presented in the last section. Since the amplitude change rate is higher than the wavelength shift of individual peaks, the sensitivity of the sensor by using the envelope spectrum is improved.

3.3.4 Temperature analysis

Table 3.3 summarizes the results of different picks and dips sensitivities for temperature variations from 25 °C to 75 °C with constant liquid level. As observed in Table 3.3, the behavior of all peaks and dips is very similar. The standard deviations for linearity and sensitivity measurements based on peaks are around 0.003 and 0.531 pm/°C, respectively. In the case of dips, similar values were found (0.007 and 1.162 pm/°C) for the previously mentioned standard deviations. As expected, the temperature changes induce a redshift peaks/dips instead blueshift peaks/dips when compared with the liquid level sensitivity (Table 3.1) [81, 126].

TABLE 3.3: Comparative of sensitivity and linearity of several peaks and dips for temperature variations.

Wavelength Peaks [nm]	R^2	Sensitivity [pm/°C]	Wavelength Dips [nm]	R^2	Sensitivity [pm/°C]
1533.64	0.966	21.38	1533.08	0.961	19.78
1534.76	0.966	21.38	1534.20	0.966	21.38
1535.80	0.958	22.11	1535.24	0.958	22.11
1537.01	0.962	22.25	1536.36	0.958	22.11
1538.12	0.964	22.55	1537.56	0.976	22.84

Figure 3.9 depicts the mean wavelength shift as a function of temperature variations for peaks and dips analyzed in Table 3.3. The averaged sensitivity achieved with the new linear regression for peaks and dips is 21.93 pm/°C and 22.06 pm/°C, respectively, and the correlation coefficient in both cases is 0.966. The error bars represent the standard deviation and the dots the mean value of peaks and dips. Therefore, by selecting the highest liquid level sensitivity in Table 3.1 (-2.299 pm/mm), the achieved error for temperature changes is ~ 9.595 mm/°C. That implies an error of 7.93% in liquid level measurement. However, with the proposed approach in this chapter, the error can be reduced drastically since the envelope analysis leads a considerable liquid level sensitivity improvement as was already presented.

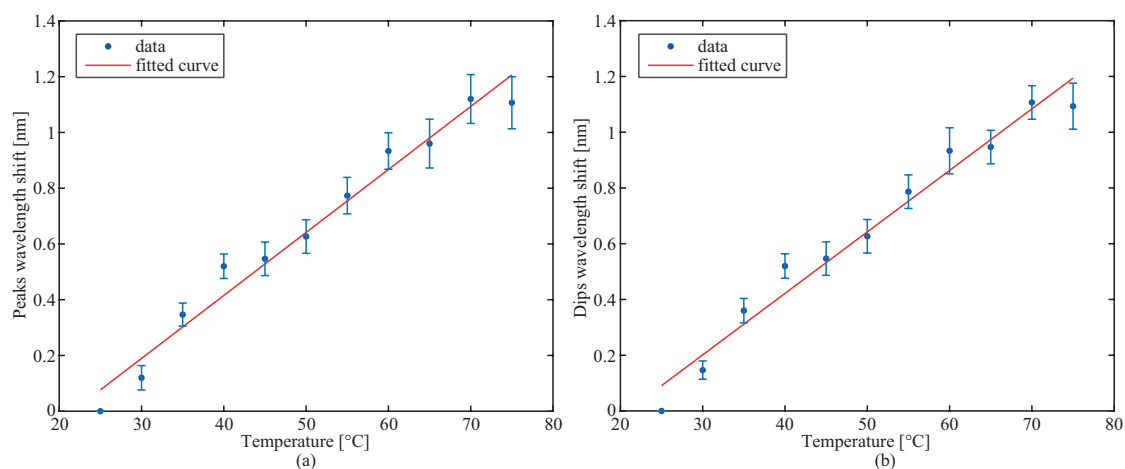


FIGURE 3.9: Mean wavelength shift as a function of temperature variations with constant liquid level: (a) Peaks mean and (b) dips mean.

The last assumption is only valid if the temperature changes do not affect the envelope shape. To verify this, the analysis of the envelope spectra under temperature effects is presented in Figure 3.10. The envelope spectra variations are depicted in Figure 3.10(a), where an inset of the first peak (used to measure liquid level centered at 1544.542 nm) shows a small wavelength shift. Figure 3.10(b) depicts the wavelength and amplitude variations as a function of temperature variations. It is clear the wavelength shift is not linear and a maximum variation is around 900 pm. From 25 °C to 40 °C no significant wavelength variations are observed, however, the amplitude decreases. For higher values, fluctuations in both signals are observed. If the temperature cross-sensitivity of ~ 18 pm/°C is considered, the error induced in the liquid level by temperature variations is around 0.562 mm/°C, that means an error of 0.468% for a length sensor of 120 mm.

3.4 Discussion

The advantages that can be highlighted in this kind of IFOS are its easy and cost-effective fabrication process, which uses a commercial fusion splicing machine and three different kind of fibers SMF, MMF and RCF to construct the sensor arrange. As presented in Chapter 2, no special optical fiber is mandatory to use in the sensor region (in this case RCF), however, the RCF allows coupling more optical power to the cladding improving the sensor's sensitivity. Besides, the MZI-based IFOSs offers

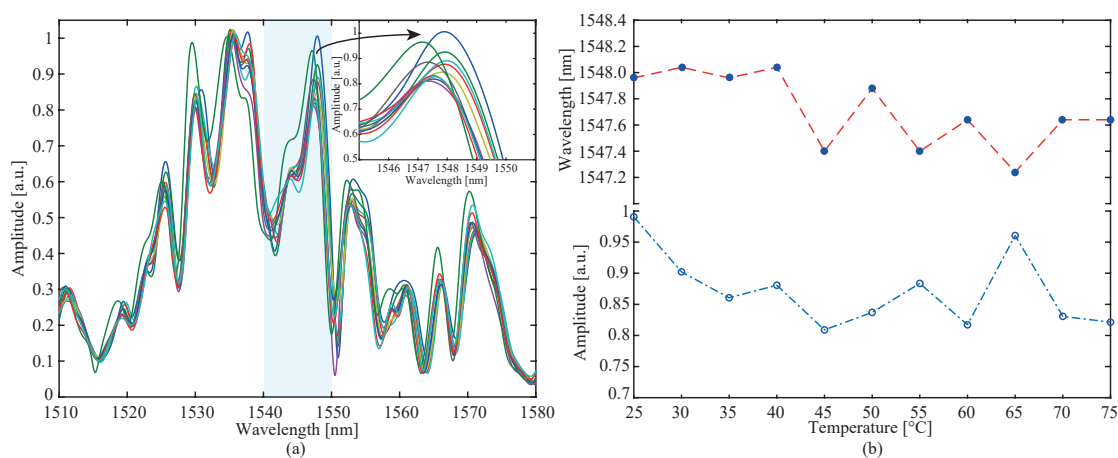


FIGURE 3.10: (a) Envelope spectra for several temperature values; (b) wavelength and amplitude variations of first envelope peak as a function of temperature variations with constant liquid level.

higher sensitivity when compared with other FOLLS such as based on FPI and FBG and shows high linearity becoming them in a good candidate for liquid level monitoring. On the other hand, some disadvantages of this IFOL can be addressed: disagreeing with [44] this kind of sensors are not suitable for large range of liquid level measurements, from meters, up to hundreds of meters because: I) The sensor length is limited for the laser coherence reducing the liquid level sensing. II) The sensitivity is decreased exponentially when the physical sensor length is increased. III) The traditional method to interrogate this sensors is not suitable for longer lengths since the the FSR is reduced and the observation window of a single peak/dip would not be wide enough to allow distributed level sensing over the whole sensor length. IV) The visibility or contrast (amplitude modulation) of the interference pattern of the whole spectrum is reduced when the sensor length is increased precluding the implementation of the proposed based-envelope spectrum interrogation technique. The optical power loss can be attributed to the fact that the surrounding liquid (water) has refractive index closer to the cladding, which leads to power leaking of the cladding modes. V) Moreover, the sensor need to be exposed directly to the liquid which can leads to erroneous measures if the liquid impregnates the IFOLS. VI) Furthermore the optical fiber sensor robustness is reduced due to the acrylate protection is striped. Finally, the light polarization is a factor that affects the sensor response, so, two possible solutions can be addressed. First, a polarization-maintaining fiber could be used in the sensor section [83]. Second, a simple way to avoid this issue is using a non-polarized optical source making the sensor immune to polarization

changes [81]. In addition, no low cost interrogation system have been proposed in order to interrogate this kind of sensors. Usually an OSA is used to monitor the spectrum changes, which is not suitable for real-time applications in industry since its high cost, weigh and volume and its trade-off between resolution and sweep frequency.

3.5 Conclusion

This chapter presented a novel sensor interrogation technique based on the full envelope analysis of the interference pattern produced by an in-line MZI. This technique allowed both to enhance the sensitivity of standard MZI sensors and to use longer sensors. In comparison with traditional interrogation techniques that take into account the evolution of the wavelength of only one peak or dip, the proposed method increased the sensitivity by at least an order of magnitude and also allowed sensor the be experimentally demonstrated for about 4 times longer. Sensitivities of 33.75 pm/mm were obtained for a sensor with 120 mm and a maximum sensor length of 470 mm was achieved still maintaining high linearity and presenting a sensitivity 17.17 pm/mm. In addition, the temperature cross-sensitivity was analyzed, where an liquid level error induced by temperature variations was estimated around 0.004%. The proposed interrogation technique could be implemented in different sensors with similar spectral behavior.

Chapter 4

In-fiber FPI Micro-cavity

4.1 Introduction

As presented in Chapter 2 the optical fiber has several protection layers. When the last one before achieving the cladding is removed (acrylate protection) the optical fiber sensor robustness is considerably reduced even more when the OFS needs to be in direct contact with the liquid as presented in Chapter 3. However, the based interferometric sensors present high sensitivity and easy and cost effective fabrication. In this direction, a second interferometer sensor for liquid level measurements is presented in this chapter. A commercial fusion splice machine (Fujikura 50S), a standard SMF (SMF-28, Corning) and a fiber (SMG-652, Corning), which was recycled after destroyed by the catastrophic fiber fuse effect [127–129], were used to create the in-fiber FPI micro-cavity. The fabrication process is simple and inexpensive by comparing it with other FPI micro-cavities [122, 123]. In order to measure liquid level, the micro-cavity was embedded into a diaphragm epoxy resin.

4.2 Sensor Fabrication

4.2.1 The fuse effect

The fuse effect observed for the first time in 1987 by Kashyap [42][19,20], is a destructive phenomenon which is produced due to local high power leakage in a tight bend or dirty/damage optical connector, where it is induced a local temperature increment up to the core fiber vaporization, triggering a catastrophic chain reaction [127].

Usually, optical power values higher than 1.0 W are enough to produce this effect, which is characterized by a bright white spot resulting from the hot plasma in the ignition zone, following by its propagation in direction to the optical source, where the fuse discharge propagation velocity is dependent of the optical power density [127]. This catastrophic effect is finished when the optical source is turn off. As a result, an irreversible destruction of the optical fiber core, and sometimes of the cladding and acrylate layer protection can be produced. Leakage loss can cause the polymer coating to catch fire, as a result of absorption. The destruction core is characterized by a periodic formation of cavities, where them shape, size and distance between holes, depend on the kind of laser CW or pulsed used [42].

In order to produce the fuse effect in the fiber SMG-652, under controlled conditions, a wavelength 1480 nm Raman fiber laser (IPG, Model RLR-10-1480) at 3 W of optical power was used [127–129]. As presented in Figure 4.1(a) the fuse effect ignition is started with a metallic sheet in the extremity of the fiber. Due to it propagates from the fusion zone to the laser direction, a dummy SMF was used between the fiber under test and the laser to protect it. The damage optical fiber after the catastrophic fuse effect is showed in Figure 4.1(b). In this case, the micro-metric periodic hollow voids in the optical fiber core are around $6.4 \mu\text{m}$ length and $5.9 \mu\text{m}$ high.

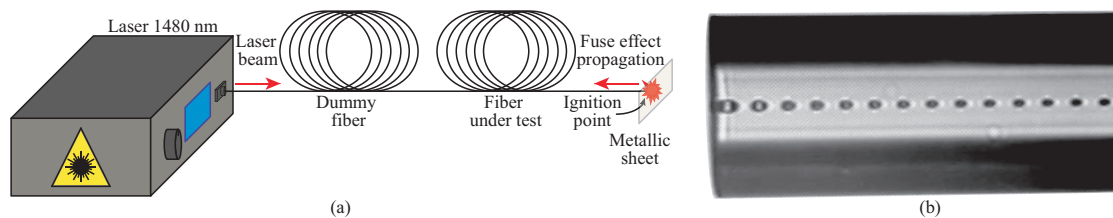


FIGURE 4.1: (a) Schematic of the setup used for the fuse effect ignition (adapted from [130]) and (b) picture of recycled SMF destroyed after catastrophic fuse effect.

4.2.2 Micro-cavity fabrication

In order to fabricate the micro-cavity with the recycled optical fiber after destroyed by the catastrophic fuse effect, the methodology presented in Figure 4.2 was adopted [129]. All the photographs were obtained from the splicing machine during the process fabrication, where X and Y represent the orthogonal directions of the fiber. The first step is the fusion splicing between a standard SMF and a fiber damaged by

the fuse effect (Figure 4.2(a)). The surfaces of both fibers are cleaned and cleaved, and the parameters in the splicing machine have been optimized to an arc power level of 20-bit (~ 20 mA), during 3 seconds. As a result, a large cavity with drop shape (in the best of cases) is obtained (Figure 4.2(b)). This cavity shows an expansion in the core as well as in the cladding after the fusion spliced process. The next step is to cleave this cavity and splicing it with a second standard SMF as depicted in (Figure 4.2(c)). In order to facilitate the identification of the location bubble and its cleaving process a microscope was used. During the process fabrication it was observed that this step has a big influence over the resulting micro-cavity shape (Figure 4.2(d)). Thus, if the cleaved bubble is small, as a result a small micro-cavity will be obtained. However, the micro-cavity size can be increased by exposing the bubble to additional arcs, due to the gas volume is proportional to the temperature, in each arc exposition an expansion of the micro-cavity is achieved, thus the FSR can be controlled. On the other hand, the visibility is strongly dependent on the mirrors shape (transversal walls of the cavity) which usually are concave structures, thus, for maximum visibility the cavity length L needs to be approximatively equal to the curvature radius of the two surfaces on the ellipsoidal cavity [131]. By selecting the correct splicing machine parameters, namely, the position of the first splice and the number and intensity of the arc discharges, it is possible to control the cavity size and shape, and therefore to produce similar micro-cavities. As depicted in Fig. 4.2(d), the resulting bubble is an ellipsoid. The distance from the SMF acrylate protection to the fusion splicing is around 15 mm in both sides. The presented methodology was repeated around fifty times, getting volume cavities from 0.3×10^5 to $5.8 \times 10^5 \mu\text{m}^3$.

The spectra of three sensors (acquired with a interrogator with 1 pm resolution) and them respective electronic microscopy image of x50 are depicted in Fig. 4.3. In each image is represented one of the three geometric characteristics by the arrows, where L_I is the length of the cavity in the axial direction, H_I is the transversal cavity hight and W_I is the cavity adjacent wall width, which generally is almost the same in both sides. As expected, for longer micro-cavities the FSR is reduced, which agrees with equation 2.22. On the other hand, the spectra amplitude is a function of the surface's reflectivity which is the same for all the sensors. Spectra 1 and 3 shows a visibility ~ 8 dB, however, the spectrum 2 presents a 20 dB visibility. This fact can be attributed to the shape of the reflecting surfaces where neither more optical power will be more reflected because the mirror shape is less curved increasing the spectra

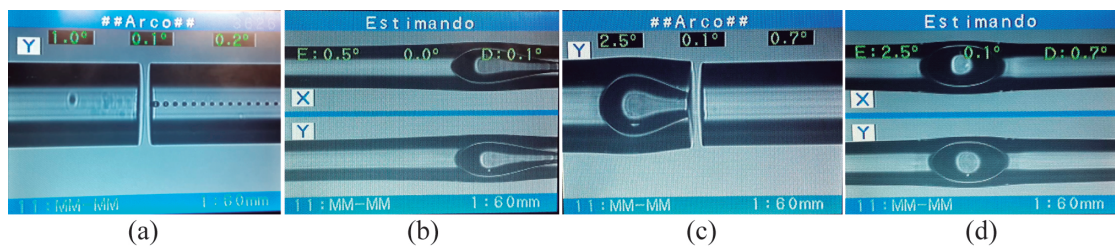


FIGURE 4.2: FPI micro-cavity fabrication process. Pictures taken from the splicing machine FSM-40S. (a) Splicing process between a standard SMF and a fiber destroyed by the catastrophic fuse effect, (b) a cavity with drop shape after fusion splicing between the SMF and the recycled fiber, (c) splicing process between the cleaved cavity with drop shape and a standard SMF, (d) typical resulting FPI micro-cavity after splicing process.

visibility, or more optical power will be more dispersed around the bubble due to the curved mirrors increasing the optical power losses.

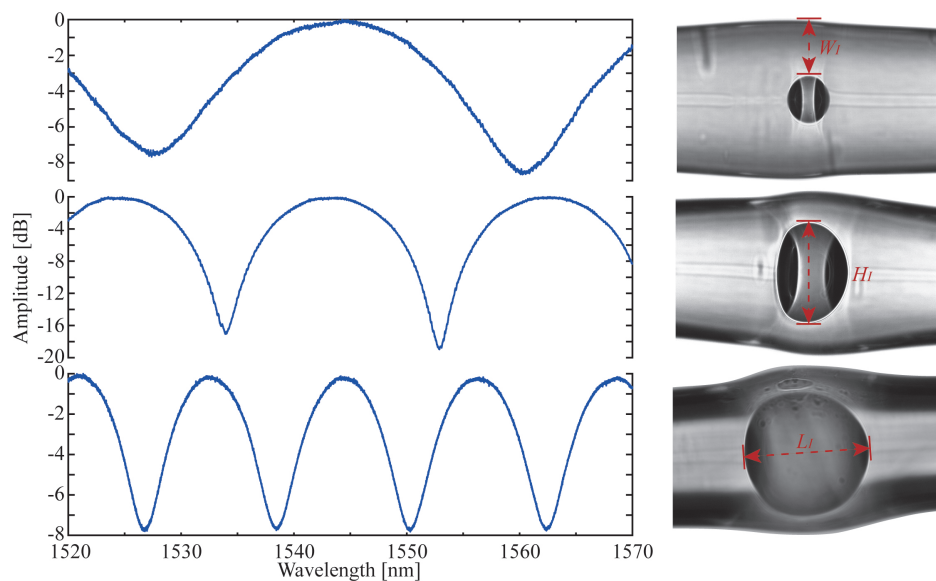


FIGURE 4.3: Spectral characteristics of FPI sensors according to their physical size.

Table 4.1 summarizes geometric properties of the 16 sensors analyzed, where it is compared the micro-cavities axial dimensions acquired from the microscopic image (L_I) and the obtained from the FSR (L_S) from the spectra analysis, according to the equation 2.22. In order to simplify the acquisition of bubbles dimensions an image processing tool was developed. As it can be observed, the error between axial dimension L_I and L_S is $\sim 2.8 \pm 2.266\%$. It can be attributed to the microscope focus

which can induces more distortion over the image, which in turn increase the error calculation. In the case of sensor 4 it was not possible to compare this parameters because the interrogation range (from 1520 nm to 1570 nm) limited the FSR visibility.

TABLE 4.1: Dimension of the micro-cavities taken from both the electronic microscopy image and from the spectra.

Sensors	W_I [μm]	H_I [μm]	L_I [μm]	L_S [μm]	error [%]	FSR [nm]
1	33.794	107.911	86.789	89.379	2.897	13.440
2	64.728	67.829	51.976	52.104	0.245	23.055
3	52.343	85.156	55.859	57.961	3.626	20.725
4	86.986	42.123	31.335	-	-	-
5	29.604	122.028	103.699	102.850	0.822	11.680
6	73.002	67.123	109.589	114.400	4.205	10.500
7	81.762	51.861	38.728	36.457	6.229	32.950
8	73.872	65.261	75.515	75.622	0.141	15.885
9	55.033	81.843	65.554	65.967	0.626	18.210
10	56.264	87.813	63.325	65.020	2.606	18.475
11	47.303	98.314	76.404	78.232	2.336	15.355
12	55.928	90.939	59.507	63.391	6.127	18.950
13	41.150	109.36	123.708	132.96	6.958	9.035
14	94.988	39.863	36.560	36.685	0.340	32.745
15	49.691	106.541	68.795	70.331	2.184	17.080
16	37.488	119.419	92.432	94.661	2.354	12.690

4.2.3 Strain and temperature characterization

After fabricated the FPIs micro-cavities, the strain characterization was performed with the setup depicted in Fig. 4.4. The backscattered spectra were monitored with a FBG interrogator (SM125-500, Micron Optics) with 1 pm resolution at room temperature (~ 21 °C). The sensor is centered and pretensioned before glued its fiber extremities with Cyanoacrylate in the supporting structures (Fixed and moving platforms), which are separated one each other 250 mm. In each anchorage point the fiber acrylate protection was removed in order to improve the addition between the optical fiber and the platforms. The longitudinal strain was performed up to $635 \mu\epsilon$ in steps of $25.4 \mu\epsilon$, which corresponds to a maximum relative strain of $2540 \mu\epsilon$ in

steps of $98 \mu\epsilon$, according to $\mu\epsilon = \Delta\epsilon/L$, where L is the distance between anchorage points and $\Delta\epsilon$ is the increment step. The complete cycle (strain and back) was repeated three times.

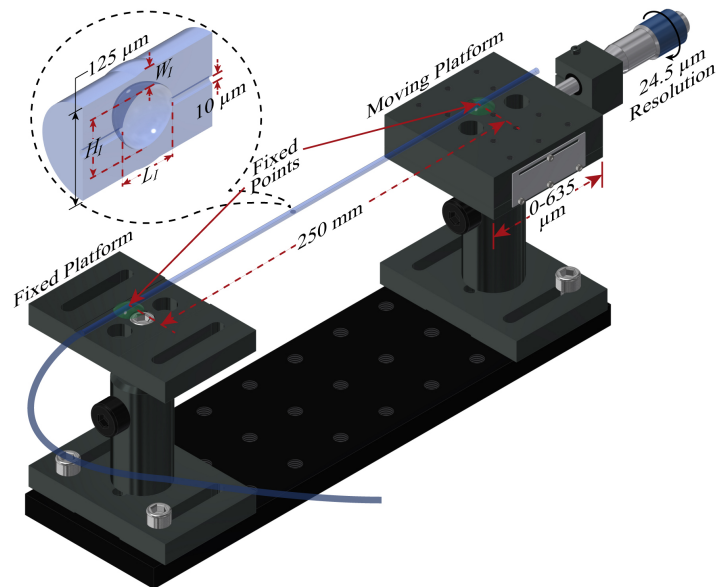


FIGURE 4.4: Strain setup.

To characterize the temperature response of the FPI micro-cavities a thermal chamber (Challenge Angelantoni Industrie, Model340) and the same interrogator was used. Among the sixteen sensors, 1 to 3 were selected with the criteria of highest strain sensitivity. The temperature was increased from 5°C to 40°C in steps of 5°C after stabilized (around 30 minutes after set the temperature step). As a temperature reference sensor, a FBG was also characterized together with the FPIs.

4.3 Liquid Level Measurement

4.3.1 Diaphragm based FOLLS fabrication

The micro-cavity itself in its current format is not able to measure the liquid level changes, therefore, a pressure sensor based on an epoxy diaphragm resin is proposed. The sensor fabrication was carried out with a similar process to the one presented in [107] (see Figure 4.5). First, the FPI sensor is both centered and prestressed into a container (plastic mold) which has the same dimensions of the epoxy resin

diaphragm (1.1 mm wall height and 50 mm internal diameter). As aforementioned, after fabricating the micro-cavity, the striped coating layer protection in the sensor region is ~ 30 mm. Near the transition from the resin to the outside, the acrylate protection is preserved to improve the mechanical resistance between the diaphragm and the fixed fiber extremities. The internal surface of the container is completely flat and smooth in order to guarantee a uniform texture. Finally, the epoxy resin (Liquid lensTM - Advanced 2) was applied keeping the mold undisturbed for 24 hours.

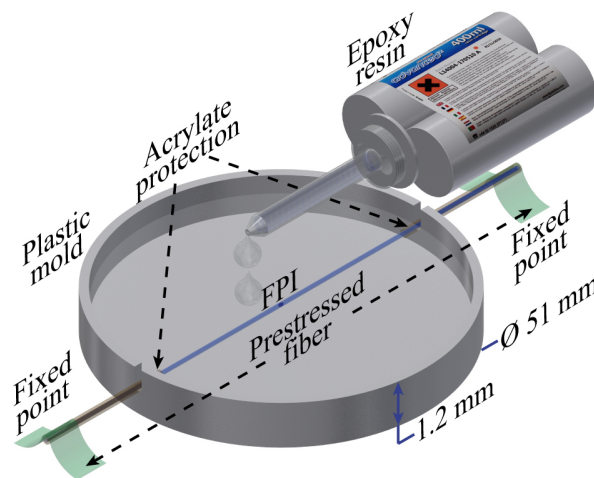


FIGURE 4.5: Diaphragm process fabrication.

In order to define the position of the sensor into the diaphragm, a finite element analysis was performed with Ansys software. A pressure of 9800 Pa (1 m of water column) was used as the input to observed the diaphragm deformation. The diaphragm and the simulation inputs are presented in Figure 4.6.

The equivalent strain (Von Mises) on the fiber is presented in Figure 4.7, where it is possible to observe that the strain on the fiber occurs at the whole diameter of the diaphragm. As expected, a higher deformation on the hole region (diameter of 19mm) is evidenced and the maximum deformation occurs at the central position, suggesting the best point to place the sensor.

4.3.2 Temperature dependence

Although the micro-cavity was already characterized for temperature, a new characterization is necessary to carry out in the diaphragm-based configuration. The same

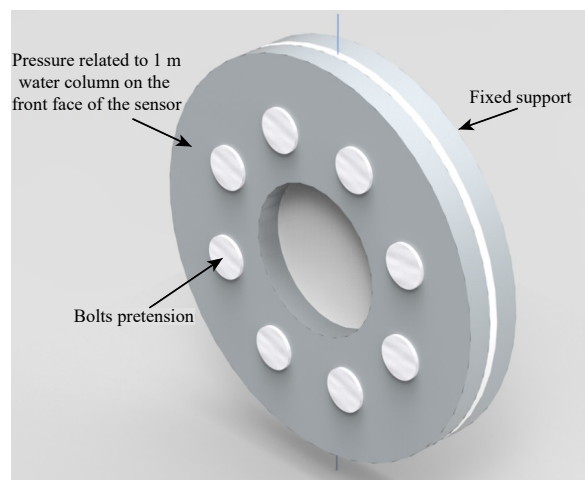


FIGURE 4.6: Diaphragm and the inputs of the simulation.

thermal chamber and the same parameters previously presented in Section 4.2.3 are used in this stage. The diaphragm material temperature characterization is an important parameter which has a big influence over the temperature response of the optical sensor. Depending on the diaphragm material the sensitivity is considerably increased, specially in rubber-based diaphragms [14, 75].

4.3.3 Experimental setup

In order to validate the FOLLS two configurations were analyzed Fig. 4.8. On the one hand, the diaphragm-based sensor was anchorage between a Polytetrafluoroethylene (PTFE) structure and a metallic support with 60 mm external diameter and 19 mm internal hole diameter. The PTFE mold has a cylindric cavity with 19 mm internal hole diameter and 3.7 mm deep. To avoid the buoyancy effect the structure was glued with Cyanoacrylate to another heavier metallic circular structure and was immersed in the center of the liquid reservoir (configuration (a)). On the other hand, the diaphragm-based sensor was anchored in a lateral wall of the reservoir, where there is a hole of 19 mm (configuration (b)). Both experiments were performed independently one each other at temperature room (~ 21 °C) in an acrylic structure of 165 mm side and 960 mm hight.

The water column imposes a pressure over the diaphragm. When the liquid level is increased the pressure applied on the diaphragm is increased too. This pressure changes are translated into longitudinal strain in the optical fiber, leading to an axial

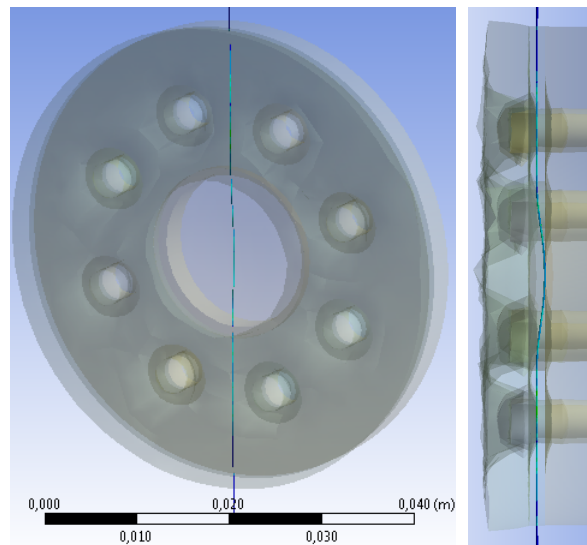


FIGURE 4.7: Equivalent strain on the fiber. Where the blue regions present lower strain and a red shift of the fiber color represent an increase of the strain.

strain over the micro-cavity, which in turn, generates changes in the backscattered optical spectrum. To analyze the sensitivity of the proposed FOLLS, the liquid level was increased from 0 mm to 900 mm in steps of 20 mm, in an up/down cycle. The temperature was monitored by a FBG temperature reference sensor, which was installed as near as possible to the FOLLS into a metallic pipe in order to avoid external mechanical perturbation.

4.4 Results

4.4.1 Strain and temperature responses

When the micro-cavities are exposed to strain a redshift spectra can be observed. Depending on the FSR it is possible to analyze several dips or peaks, however, the interrogation range is limited by the interrogator device used (from 1520 nm to 1570 nm). Fig. 4.9(a) depicts the redshift spectrum of the sensor 2 for 0, 980 and 1960 $\mu\epsilon$. As observed, in this case it is possible tracking two dips and peaks, which have the same behaviour with similar sensitivities. Fig. 4.9(b) depicts the wavelength shift as a function of the longitudinal strain for both peak and dip highlighted in the square regions of Fig. 4.9(a). As a result, the fitted curve (solid line)

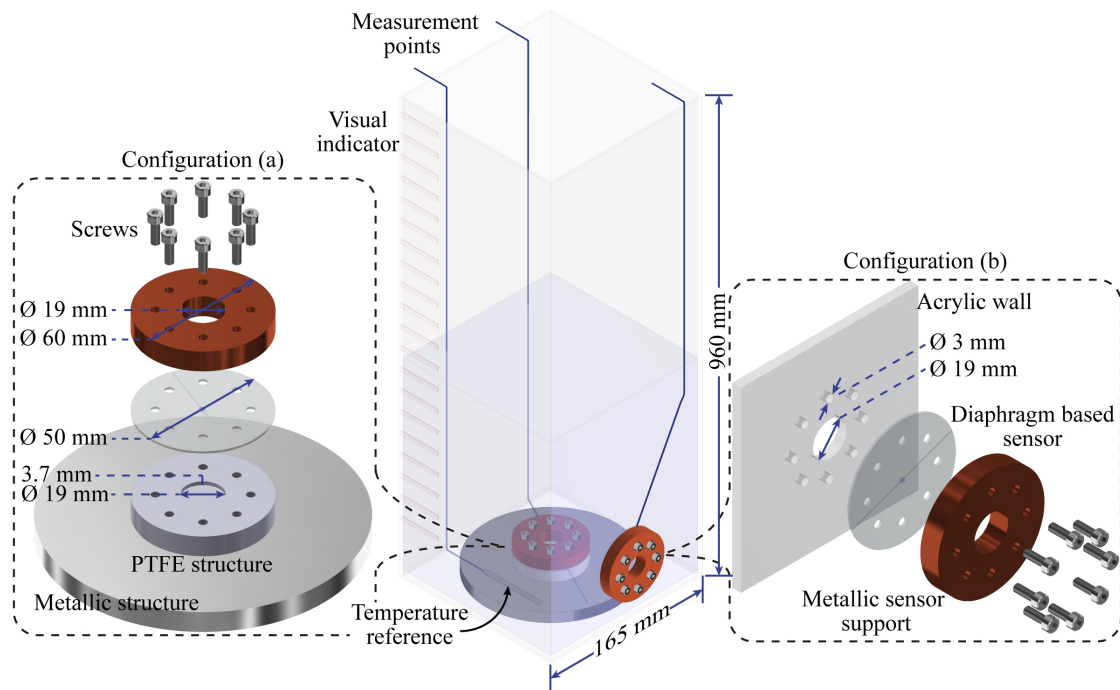


FIGURE 4.8: Schematic of the liquid level setup used to test both configuration: (a) sensor immersed into the water tank and (b) sensor anchored at lateral tank wall.

shows a high linearity response with sensitivity of $3.158 \text{ pm}/\mu\epsilon$ and a coefficient of determination R^2 higher than 0.999 for the dip centered at 1556.385 nm . In the case of the peak centered at 1544.802 nm , higher sensitivity was achieved ($3.343 \text{ pm}/\mu\epsilon$) with lower coefficient of determination ($R^2 = 9.993$).

From the analyzed region spectra the highest sensitivity of dips and peaks is depicted in Table 4.2. For the group of sensors analyzed, the fitted curves reported a R^2 higher than 0.999 showing them high linearity with an error less than 0.4% in the most of the cases. As expected, the peaks showed similar sensitivity but higher error due to them lower selectivity in frequency.

When the micro-cavity is exposed to temperature changes, minimum redshift spectrum is observed with the temperature range analyzed (From 5°C to 40°C). This FPI micro-cavities conveniently shows low temperature sensitivity compared to FBGs [129], however, an optical power variations are observed. On the other hand, if the micro-cavity is embedded into the resin diaphragm, the sensitivity is drastically increased. When the rubber diaphragm is exposed to temperature changes, the thermal expansion of the material imposes an axial strain over the embedded OFS which results in

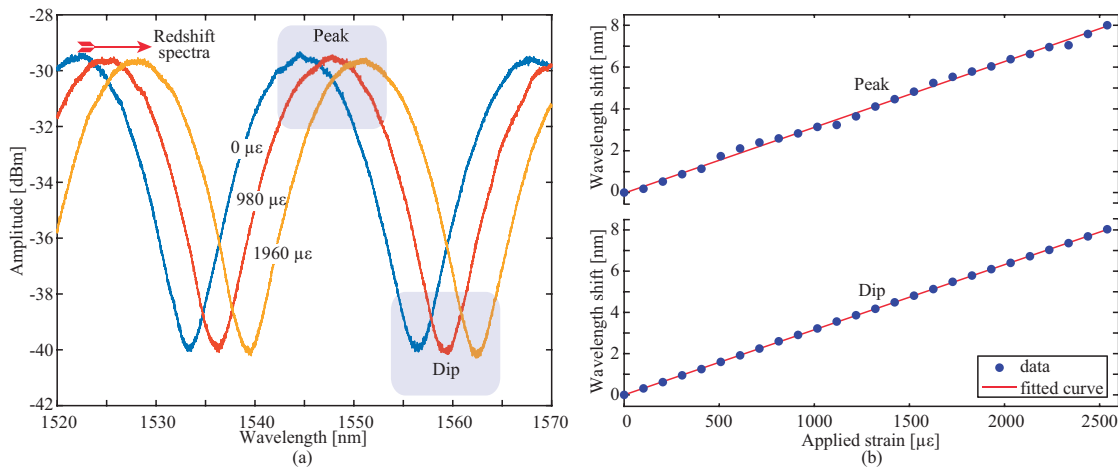


FIGURE 4.9: Micro-cavity strain response: (a) Redshift spectra and (b) Peak and dip as a function of the applied strain.

a redshift spectrum as a result of the temperature increment. Figure 4.10(a) depicts the spectra of the temperature characterization of sensor 2 in simple configuration or embedded into the diaphragm. Figure 4.10(b) shows the wavelength shift as a function of the temperature for the FBG, FPI and FPI plus diaphragm, where the obtained sensitivities are ~ 9.0 pm/ $^{\circ}$ C, ~ 2.4 pm/ $^{\circ}$ C and ~ 61 pm/ $^{\circ}$ C, respectively.

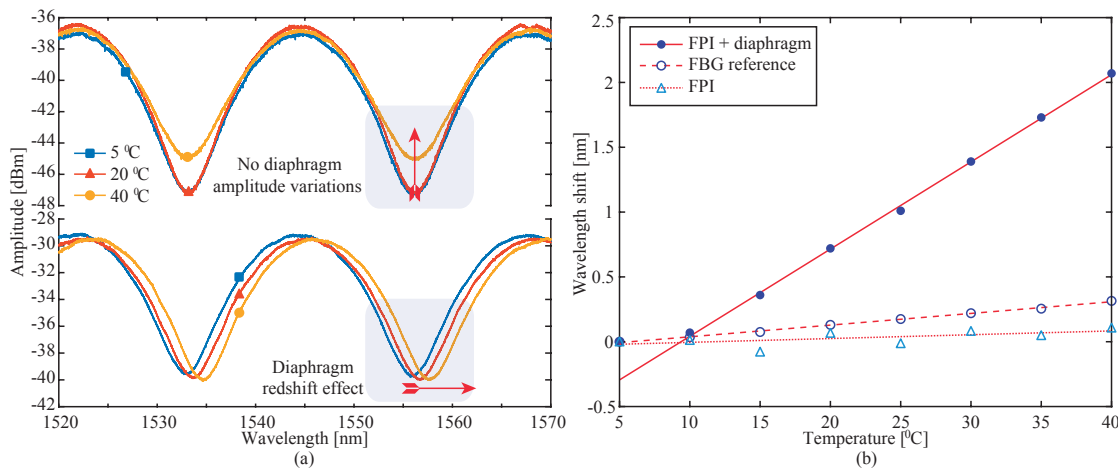


FIGURE 4.10: Micro-cavity temperature response: (a) single and diaphragm configuration spectra for three different temperature values and (b) wavelength shift as a function of the applied temperature for FBG, FPI and FPI embedded into the diaphragm.

TABLE 4.2: Highest strain sensitivities for dips and peaks of the studied sensors in the form $mean \pm standard\ deviation$.

Sensors	Dip [pm/ $\mu\varepsilon$]	Peak [pm/ $\mu\varepsilon$]
1	3.188 ± 0.004	3.140 ± 0.043
2	3.158 ± 0.008	3.146 ± 0.445
3	3.308 ± 0.003	3.343 ± 0.112
4	2.878 ± 0.059	3.018 ± 0.971
5	3.037 ± 0.006	3.091 ± 0.048
6	1.634 ± 0.004	1.639 ± 0.019
7	2.814 ± 0.098	2.720 ± 1.325
8	2.677 ± 0.013	2.636 ± 0.094
9	2.778 ± 0.003	2.749 ± 0.047
10	2.692 ± 0.002	2.679 ± 0.071
11	2.534 ± 0.008	3.004 ± 0.224
12	2.808 ± 0.004	2.814 ± 0.639
13	2.447 ± 0.018	2.441 ± 0.047
14	2.340 ± 0.130	2.325 ± 0.626
15	2.736 ± 0.041	2.853 ± 1.252
16	2.533 ± 0.008	2.477 ± 0.007

4.4.2 Liquid level measurements

The liquid level responses of both configurations are depicted in Figure 4.11. Among the dips analyzed of sensor 2, the highest sensitivity were selected to measure the redshift spectra minima as a function of the liquid level. During the experiments, temperature variations (Δ_T) were monitored with the FBG sensor reference, achieving values up to 9 °C and 4 °C in up and down cycles, respectively. With this information it is possible to mitigate the temperature cross-sensitivity, by implementing the same matrix used for FBG sensors (Equation 2.40). After the temperature compensation the configuration (a) and (b) exhibited a mean sensitivity of ~ 1.83 pm/mm and ~ 4.7 pm/mm, respectively. As expected, in the configuration (a) the sensor showed lower sensitivity when compared with configuration (b). This fact can be attributed to the diaphragm deformation in direction to the PTFE cavity, which reduce the cavity volume increasing the internal pressure, which in turn imposes resistance to the diaphragm deflection. On the other hand, in configuration (b) the diaphragm deflects freely under atmospheric pressure.

Table 4.3, summarizes the level rise and fall sensitivities of both configurations. In

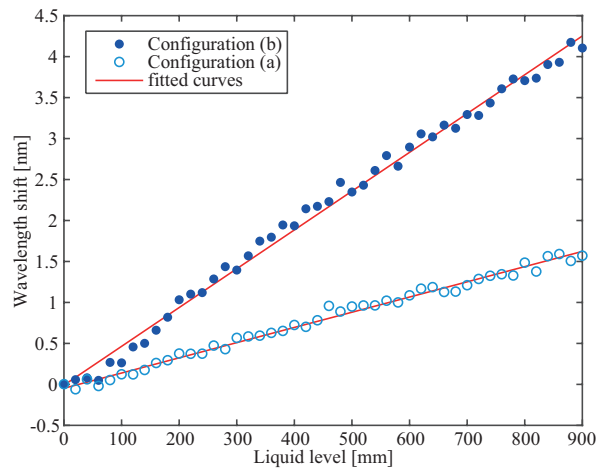


FIGURE 4.11: Wavelength shift as a function of liquid level for both configurations (a) and (b) Figure 4.8.

both cases, the sensitivity achieved for level rise is higher when compared with level fall. During the experiments, the temperature variations were monitored with a FBG-based reference sensor. Generally, the temperature was higher when rising the liquid level. Therefore, this difference of sensitivities could be attributed that polyurethane resin behaving differently when temperature varies, i.e. at higher temperature it deforms more easily than at lower temperatures. To verify this hypothesis, it is necessary to characterize the sensor as function of level, at several constant temperatures. Unfortunately, the current setup lacks liquid temperature control. However, this kind of validation will be addressed in the next chapter, where an industrial-like water plant is used to characterize a similar FOLLS.

TABLE 4.3: Level rise and fall sensitivities of configuration (a) and (b).

Configuration (a)	R^2	Sensitivity [pm/mm]	Wavelength Dip [nm]
Level rise	0.992	1.84 ± 0.04	1533.370
Level fall	0.993	1.81 ± 0.04	1533.155
Configuration (b)			
Level rise	0.995	4.84 ± 0.08	1531.855
Level fall	0.995	4.58 ± 0.06	1531.690

4.5 Discussion

The cost effective technique to fabricate the FPI micro-cavities presented in this chapter was adopted from [129]. In four simple steps it is possible to produce this kind of sensors, however, some issues are inherent on this technique. The first splicing step (Figure 4.2(a)) is crucial for the final bubble shape (Figure 4.2(d)). By using the same parameters in the splicing machine in each splicing process the preform (Figure 4.2(b)) can take several forms such as: large thin bullet, small, medium or big ellipsoid, even instead of expanding the core and create the preform cavities, the core can melting down and the preform cavities are not be produced. By assuming that the splicing machine performs the splicing process perfectly, this stochastic result could be attributed to the conventional cleaving process, which no guarantee both the same cleave angle at the endfaces of the fibers, and the same cleave position over the fuse effect cavities, allowing more or less air into the preform cavities. The big drop shape (Figure 4.2(b)) is the best of cases because simplify its cleaving process. However, in this step the same issue related with the cleave position over the preform bubble will affect the final shape of the FPI micro-cavity. As discussed before, the final volume of the bubble can be altered by applying several arcs achieving similar sizes. These issues lead on low repeatability of the sensors, even more, when compared with matured OFS such as FBG. On the other hand, this fabrication process is simple and inexpensive when compared with other FPI micro-cavities [122, 123], no special optical setup is required such as femtosecond laser micromachining technique requires. An inherent characteristic of this sensors is its robustness, which is reduced according to the bubble volume, since the core material is evaporated. Therefore, a thin external silica wall of tens of μm is able to support external mechanical perturbations. As a final remark of this sensor is its low temperature cross sensitivity and its high strain sensitivity which is more than an order when compared with FBG sensor as will be presented in the next chapter.

4.6 Conclusion

In this chapter was discussed a diaphragm-based FPI micro-cavity FOLLS. A cost-effective technique to fabricate the FPI micro-cavities by using a commercial splicing machine, standard SMF and recycled fiber after destroyed by the catastrophic fuse

effect, was presented. The strain and temperature sensitivity of these micro-cavities were analyzed in the ranges from $0 \mu\epsilon$ to $2540 \mu\epsilon$ and 5°C to 40°C , achieving sensitivities of $\sim 3.3 \text{ pm}/\mu\epsilon$ and $\sim 2.4 \text{ pm}/^\circ\text{C}$, respectively. After characterization, the FPI micro-cavity was embedded in the diaphragm resin in order to validate the liquid level measurements. The temperature cross sensitivity was determined as $\sim 61 \text{ pm}/^\circ\text{C}$, suggesting the use of a reference temperature sensor to mitigate this effect over the liquid level measurements. As a reference, a FBG sensor was used which after characterization reported a sensitivity of $\sim 9 \text{ pm}/^\circ\text{C}$. In order to avoid external mechanic deformation, this sensor was shield into a metallic pipe and was installed close to the FOLLS. Two configurations were tested: (a) on the one hand, the FOLLS was fixed in a PTFE structure (which has a cavity of 19 mm diameter and 3.7 mm deep) and immersed into the water tank; (b) on the other hand, the FOLLS was anchored at a lateral wall of the reservoir which has a hole with the same diameter as the PTFE structure. The achieved sensitivities were $1.83 \text{ pm}/\text{mm}$ and $4.7 \text{ pm}/\text{mm}$ for the configuration (a) and (b), respectively.

Chapter 5

FBG–embedded Diaphragms with Temperature Compensation

5.1 Introduction

In this section is addressed a FOLLS based on a silica fiber Bragg grating embedded into an epoxy resin diaphragm coupled to a temperature reference sensor, used to compensate the temperature cross-sensitivity for improving the liquid level measurement accuracy. The proposed sensor was tested in an industrial water tank with heating and recirculation. The results demonstrated a temperature cross-sensitivity reduction, enhancing the liquid level measurement thermal stability by a factor of 9, when compared to some single head sensor configurations reported in literature.

5.2 Operation Principle and Sensor Design

5.2.1 FBG sensor

A photosensitive single mode fiber (ThorLabs GF1B) was used to record the FBG sensor using the phase mask technique with a KrF UV Excimer laser emitting at 248 nm (BraggStar Industrial model from Coherent). The parameters used during the inscribing process were 5 mJ energy pulses with a repetition frequency of 500Hz. The time exposition was during 15 seconds and the FBG spectrum was monitored with the interrogator Micron optics SM125. The physical length of the FBG was

3 mm and it was embedded into an epoxy resin cylindrical diaphragm of 1.1 mm thickness and 50 mm diameter.

5.2.2 Diaphragm-based sensor fabrication

The diaphragm-based sensor was fabricated with a similar process to the one presented in Chapter 4 (subsection 4.3.1). First, the fiber acrylate protection was removed around 45 mm in the FBG fiber section, in order to improve the adhesion of the epoxy resin to the fiber, however, near the transition from the resin to the outside, the acrylate protection was preserved to improve the mechanical resistance between the diaphragm and the fixed fiber extremities. Second, the FBG sensor was both centered and prestressed into a container (plastic mold) which has the same dimensions of the epoxy resin diaphragm (1.1 mm wall height and 50 mm internal diameter).

5.2.3 Sensor header fabrication

The sensor support, made of Nylon, has a thickness of 3.1 mm by 50 mm diameter with a central hole of 19 mm diameter, which allows the diaphragm contact with the surrounding medium. 8 drilled holes of 3.8 mm and separated by 13.2 mm allow fixing the sensor over a flat surface with 8 screws. Figure 5.1 shows the structure of the liquid level sensor. One side of the diaphragm is in direct contact with the water, while the other is exposed to the outside air at atmospheric pressure. The liquid level difference causes a pressure difference on the diaphragm and this pressure is converted into strain in the optical fiber. In order to mitigate the temperature cross-sensitivity a temperature reference FBG-based sensor will be located as near as possible to the diaphragm sensor. The whole structure sensors will be presented in the next section.

5.2.4 Modeling the FBG-embedded diaphragm

When the pressure is applied on the diaphragm, its deformation can be approximated as a linear function of the pressure difference (Δ_p). Furthermore, the diaphragm material behavior is also assumed to be on the linear region. Applying

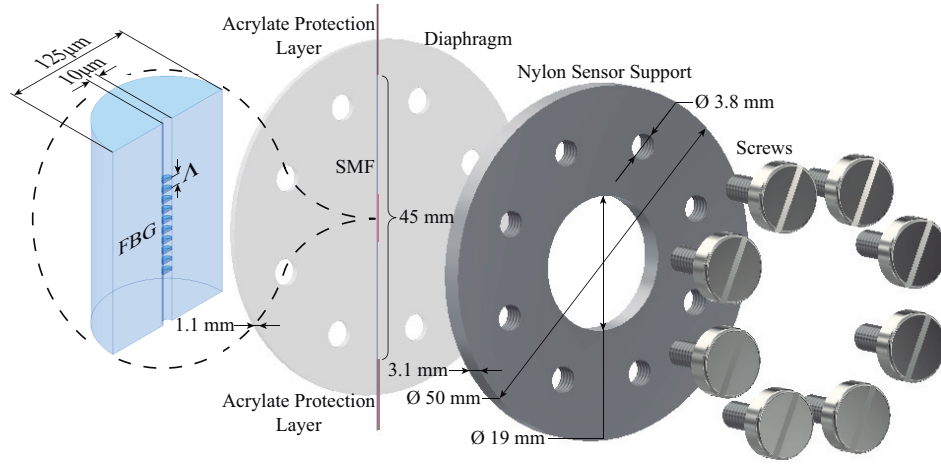


FIGURE 5.1: Structure of the proposed Sensor.

these assumptions, the diaphragm deformation (ε_{diap}) is given by [107]:

$$\varepsilon_{diap} = \frac{3}{8}(1 + \nu) \frac{\Delta_p a^2}{E_{res} t^2}, \quad (5.1)$$

where ν is the Poisson's ratio of the diaphragm material, t is the diaphragm thickness, a is the radius of the diaphragm cavity and E_{res} is the elastic modulus (Young's Modulus) of the epoxy resin. Moreover, the pressure difference happens due to the hydrostatic pressure, which is defined as [3]:

$$\Delta_p = \rho g h, \quad (5.2)$$

where ρ is the liquid density, g is the gravity acceleration and h is the liquid level.

The optical fiber is made of silica, which generally has an elastic modulus some orders of magnitude higher than epoxy diaphragms. For this reason, the optical fiber imposes restriction on the diaphragm deformation. Assuming a linear proportionality of the resultant strain on the fiber (ε_{fiber}) with the ratio between the elasticity modulus and diameters of the fiber and diaphragm, it is possible to obtain

$$\varepsilon_{fiber} = \varepsilon_{diap} \frac{E_{res} d_{res}}{E_{fiber} d_{fiber}}, \quad (5.3)$$

where d_{res} and d_{fiber} are the diameter of the diaphragm and the optical fiber, respectively, and E_{res} and E_{fiber} are the elastic modulus of the diaphragm and the silica fiber, respectively.

For the used silica optical fiber, $P_e = 0.22$, $d_{fiber} = 125 \mu\text{m}$, $E_{fiber} = 70 \text{ GPa}$. Whereas, for the epoxy resin diaphragm: $d_{res} = 50 \text{ mm}$, $E_{res} = 0.0016 \text{ GPa}$, $\nu = 0.47$, $t = 1.1 \text{ mm}$ and $a = 9.5 \text{ mm}$. In addition, $\rho = 1000 \text{ kg}\cdot\text{m}^{-3}$ and $g = 9.8 \text{ m}\cdot\text{s}^{-2}$ [107, 132].

If only the central wavelength is analyzed, the wavelength shift occurs due to longitudinal strains on the fiber. The pressure applied on the diaphragm leads to a longitudinal strain on the FBG as depicted in Figure 5.2 and the pressure increase results on the red shift of the Bragg wavelength. The transmission of strain proposed in Equation (5.3) relates the strain (provoked by the pressure) applied on the diaphragm diameter direction (solid arrows) with the strain that provokes the central wavelength shift on the FBG, i.e. the longitudinal strain, which is on the direction of the fiber diameter (dashed arrows).

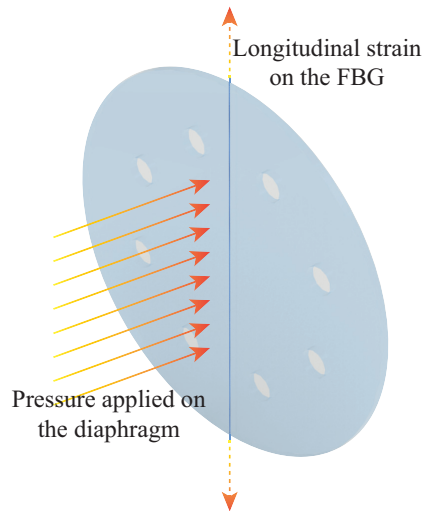


FIGURE 5.2: Direction of the applied pressure on the diaphragm and strain on the FBG.

As presented in Chapter 2, the FBG is also affected by the temperature. However, the effect of the temperature on the Bragg wavelength can be decoupled from the strain through Equation 2.40. As a result, it is possible to analyze the liquid level sensor response only with respect to the strain. Thus, Equation 2.31 can be rewritten to account the new wavelength shift ($\Delta\hat{\lambda}_B$) as [71]:

$$\Delta\hat{\lambda}_B = \lambda_B(1 - P_\varepsilon)\varepsilon_{fiber}. \quad (5.4)$$

where ε_{fiber} is the resultant strain over the fiber which is product of both the fiber strain itself and the strain over the diaphragm.

In order to evaluate the expected wavelength shift with the level increase, the parameters presented above are replaced on Equations (5.4) to (5.3), considering also $\lambda_{B,0} = 1537$ nm. Furthermore, the level (h) employed on this estimation ranges from 50 mm to 500 mm. The minimum level is 50 mm with the aim of cover both the pressure and reference temperature sensors. Figure 5.3 presents the simulated wavelength shift with the level analyzed given an estimated sensitivity of 2.8 pm/mm.

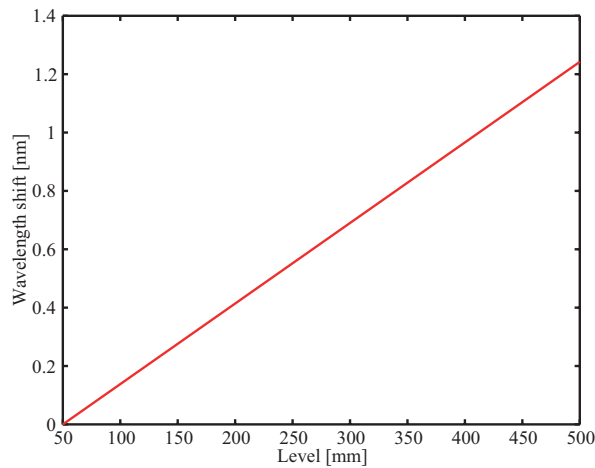


FIGURE 5.3: Simulation of the liquid level sensor response from 50mm to 500mm level.

5.3 Experimental Setup

5.3.1 Liquid level measurement

The sensor was tested in a water plant, composed by two closed metallic tanks with 400 mm diameter and 800 mm height which are located at different heights. The water is pumped from the recovery tank to the main water tank using a pump. The latter has an external rule used to measure the water level. Two valve actuators allow to control the water flow. Figure 5.4 depicts the setup used in the experiment.

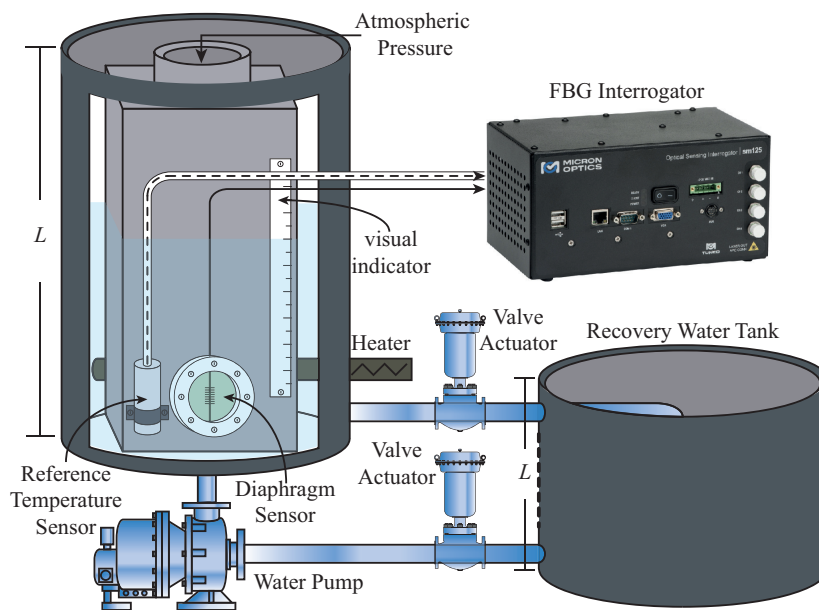


FIGURE 5.4: Schematic diagram of the experimental Setup.

The diaphragm sensor is fixed in a stainless steel hollow structure support and it is immersed into the liquid. The reference temperature FBG sensor is fixed as the same level of the diaphragm sensor in order to measure water temperature changes. A 2000 W resistor heats the water in the main tank. Both diaphragm and temperature sensors are monitored by the FBG interrogator from Micron Optics, model sm125, with a resolution of 1pm and sample rate of 0.5 Hz. The water plant devices are controlled by a Programmable Logic Controller (PLC) which is in open loop control mode.

In order to characterize the level sensor and determine the influence of the temperature over the level sensing, one experiment was performed using water as the sensed liquid. Three different water temperatures in steps of $\sim 10^\circ\text{C}$ from $\sim 27^\circ\text{C}$ to $\sim 47^\circ\text{C}$ were tested, with the tank level changing from 500 mm to 50 mm. The temperature reference sensor was located as near as possible to the liquid level sensor.

5.3.2 Pressure measurement

Because our sensor relates hydrostatic pressure with liquid level, in order to obtain the maximum liquid level supported by the diaphragm sensor an experiment using the pressure plant depicted in Figure 5.5 was performed. The diaphragm sensor is

fixed at the pressure chamber by a support with a central hole of 19 mm diameter, which is the same as used in the sensor support (Figure 5.1). Two manometers are used to measure the pressure into the plant and two valves allow control the pressure into the chamber. The same interrogator as previously was used to monitor the Bragg wavelength shift under pressure changes. Because this experiment is a destructive test, a new sensor was constructed with the same characteristics as the sensor used in the liquid level plant. The experiment was performed by increasing and decreasing the pressure into the chamber in steps of 1 Psi. Five realizations with different maximum values (8, 10, 12, 14 and 15 Psi) were made in order to characterize the pressure response.

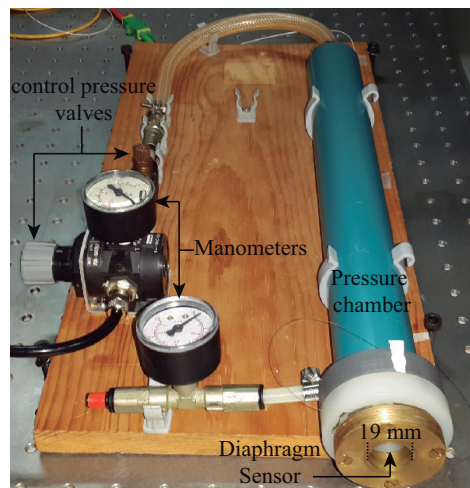


FIGURE 5.5: Experimental Setup for pressure characterization.

5.4 Results

Figure 5.6 presents the influence of the temperature over the level measurement. It can be observed the maximum level is around 500 mm and, changed in 50 mm steps. The higher the temperature, the larger are the observed wavelength offsets due to cross-sensitivity. Nonetheless, the level sensitivity remains virtually unchanged. The linear fitting curves to the wavelength shift as a function of the water level, allowed to estimate an average (for the three measurements) level sensitivity of 2.74 pm/mm with a coefficient of determination $R^2 > 0.999$. It is noteworthy the fact that the analytically estimated level sensitivity (2.8 pm/mm) was close to the one obtained experimentally with just 2% difference.

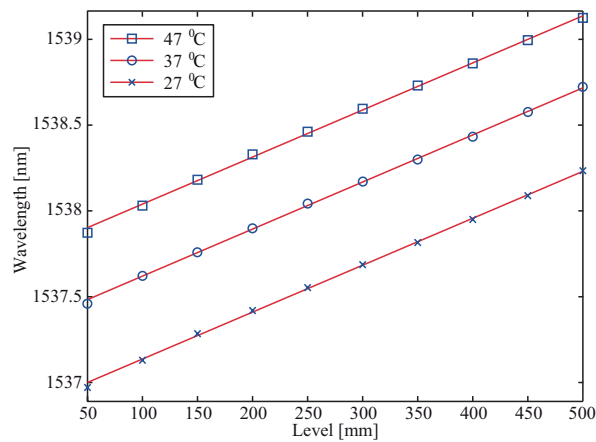


FIGURE 5.6: Level variation from 500 mm to 50 mm by three different temperatures.

In order to implement the cross-sensitivity mitigation, experiments under constant level were performed. Results for 50 cm liquid level and five different temperature values are presented in Figure 5.7. It is clear that the offset induced by the temperature over the level is fairly linear among this range (~ 25 °C to ~ 50 °C). However, for values higher than 50 °C the behavior of linearity is not conserved.

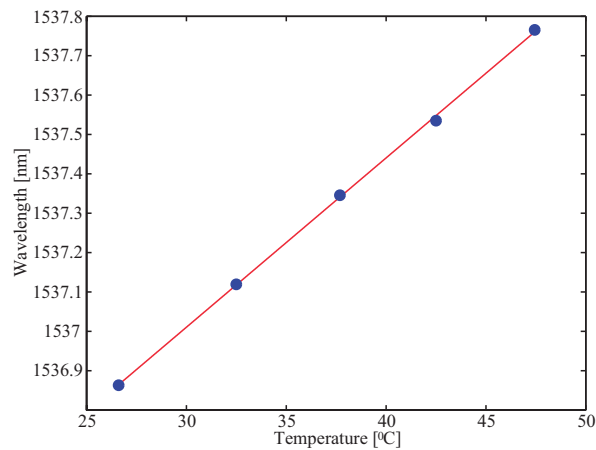


FIGURE 5.7: Sensor sensitivity of temperature over level.

The linear fit curve gives a sensitivity of 43.2 pm/°C with a correlation coefficient $R^2 > 0.999$. During the experiment, the reference temperature sensor showed a temperature error lower than 1.5 °C. In each water level stage measurement (from 500 mm to 50 mm), the temperature was acquired ten times, and the average value used to characterize the sensor.

Comparing both sensitivities, thermal and level, Figure 5.6 with Figure 5.7, the sensor exhibits a high temperature cross-sensitivity, meaning that disregarding temperatures changes can lead to erroneous level measurements. The level measurement error, referenced to temperature changes, was estimated to be 16 mm/°C.

By taking the experimental results, it is possible determine the coefficients of Equation (2.40) as:

$$\begin{bmatrix} \Delta_L \\ \Delta_T \end{bmatrix} = \begin{bmatrix} 0.0027 & \alpha * 0.0432 \\ 0 & 0.00882 \end{bmatrix}^{-1} \begin{bmatrix} \lambda_{B,L} \\ \lambda_{B,T} \end{bmatrix} - \begin{bmatrix} 1535.71323 \\ 1534.63371 \end{bmatrix}, \quad (5.5)$$

where α is the compensation constant. Thus, the variation of both the liquid level (Δ_L) and the temperature (Δ_T) can be determined simultaneously by measuring the backscattered Bragg peak of each FBG sensor ($\lambda_{B,L}$, $\lambda_{B,T}$).

From Equation (2.40) it is observed that the temperature is assumed to be equal by both the level and reference sensors. Unfortunately, in real situations it does not happen because the sensors are not exactly on the same point, therefore, there are exposed to slightly different temperatures and may need to be compensated. In our setup, the compensation constant, was experimentally estimated, yielding to a value of $\alpha = 1.037$, being within the range of the confidence bounds coefficients generated by the least squares (0.04095, 0.04559).

In order to obtain the liquid level response, in millimeters, in the presence of temperature changes, we applied Equation (5.5), to the data from the experiment depicted in Figure 5.8, which was performed in five steps. First, both temperature and liquid level were kept constant (region (I)). Second, only the liquid level was increased from 50 mm to 500 mm and it was maintained constant in the last value during 30 minutes (region (II)). Third, the liquid was returned to its initial value and was kept constant for approximately 45 minutes (region (III)). Fourth, the liquid level and temperature were increased at the same time from 50 mm to 500 mm and from ~ 29 °C to ~ 48 °C respectively, highlighted by the rectangle in region (IV). Finally, the water temperature was controlled (on-off) around ~ 48 °C.

Figure 5.8(a) depicted the wavelength shift error generated by the temperature variation in region (IV). As can be observed, the error is around 770 pm, which is according with a variation of 18 °C (Fig. 5.7). Figure 5.8(b) shows the liquid level

compensated in solid line, and the temperature variation in dashed line. As can be observed, the liquid level error generated by the temperature changes (Figure 5.8(a)) is strongly reduced by applying the Equation (5.5). Without compensation, the estimated liquid level error is around 15 mm/°C. On the other hand, by reducing the cross-sensitivity of temperature, the estimated liquid level error is drastically reduced to around 1.04 mm/°C.

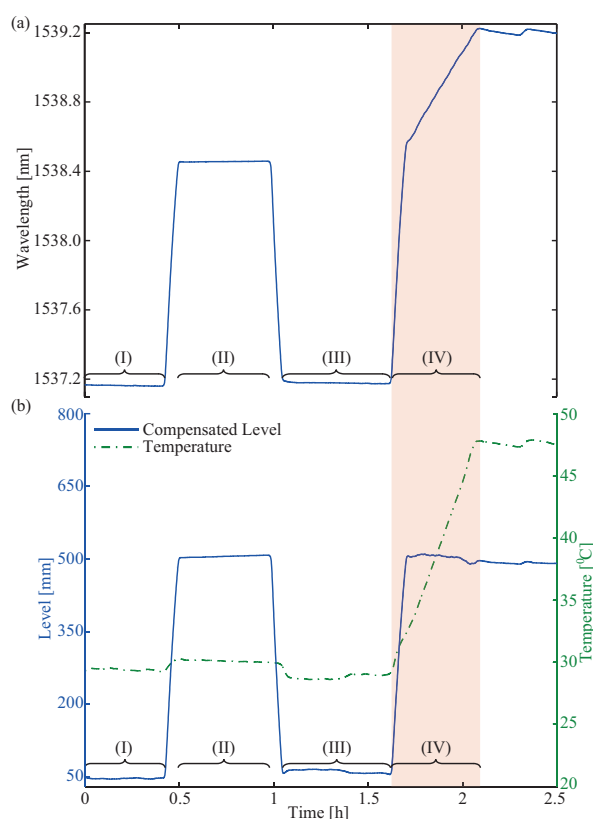


FIGURE 5.8: Cross-sensitivity compensation of the temperature over the liquid level measure.

It is possible to observe that in the regions (II) and (III) on Fig. 5.8(b) the temperature reference sensor shows some errors in its amplitude. It happens because at 50 mm of liquid level the reference temperature sensor is not completely immersed into the liquid. So, the temperature differences between the air and the water insert that error around 1.5 °C.

The temperature value was used as input into the model ($\lambda_{B,T}$ in Eq. 5.5), for very low levels, if the temperature sensor is not completely immersed on the liquid, it may generate the amplitude error in the compensated signal (observed in region

(III) of ~ 12 mm). Moreover, since an open-loop mode was employed for controlling the pump during the test, minor deviations of the liquid level may appear. However, these deviations are normally below 10 mm. It is important to highlight that similar variation were also perceived in the conventional liquid level measurement system present in the plant used.

Figure 5.9, depicted the result of the mean value between loading and unloading pressure for the measurements. The dashed, dotted, dash-dot, and solid lines represents the diaphragm sensor response from 0 Psi to 8, 10, 12, and 14 Psi, respectively. As can be observed, the sensor never achieved the plastic region during the experiment and returned to the zero value. When the value of 15 Psi was reached, the sensor broke. This pressure represents a liquid level of water around 10542 mm.

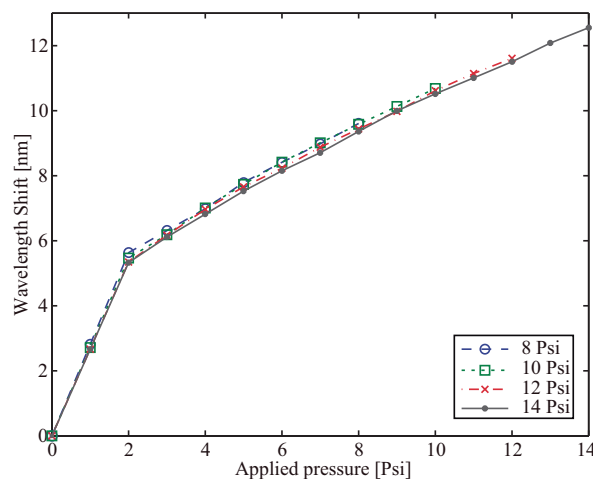


FIGURE 5.9: Characterization of maximum pressure value supported by the diaphragm-based sensor.

As depicted in Figure 5.9, the sensor's response is not linear. It can be attributed to the Young's modulus of the silica which is much greater than the modulus of the diaphragm. By increasing the pressure into the chamber the fiber will induce a transverse elongation restriction over the diaphragm that will reduce the strain in the region of the diaphragm and the FBG sensor. Furthermore, the no linearity could be attributed to the material's anisotropy. When the pressure on the diaphragm is increased, a transversal deformation over the diaphragm may appear due to stresses around of the main plane of the tensor in which the diaphragm is subjected may have higher values. In addition, the position of the FBG sensor into the diaphragm plays an important roll, which also can contributes to the no linearity.

5.5 Discussion

Table 5.1 shows the comparative between the proposed sensor and similar SMF structure sensors based on silica, FBG and circular diaphragm. A discussion of these sensors have been already addressed in the Chapter 2 (section 2.6.3). As can be seen, our sensor present both highest sensitivity and cross-sensitivity compensation of temperature among the analyzed FOLLS. Our maximum level liquid is basically limited by the dimensions of our water tank plant which have a 400 mm diameter and 800 mm height.

TABLE 5.1: Comparative of sensitivity and cross sensitivity of temperature and transverse pressure between several FOLLS.

FBG Sensor	Sensitivity pm/mm	cross-sensitivity mm/°C	Level tested mm
In this chapter	2.74	1.04	500
Ameen, et al. [75]	2.48	Not reported	1000
Marques, et al. [107]	1.021	9	750
Zou, et al. [106]	0.185	Not analized	10000

Depending on the fabrication characteristics of the sensors, the sensitivity can be increased. In the case of diaphragm-based sensors, the materials and dimensions (such as thickness and diameter) are relevant parameters. On the other hand, as presented in Chapter 2, other kind of structures based on FBGs to measure liquid level have been already proposed. Lai, et al. presented a pressure-based [94] and cantilever-based sensors [95] to measure liquid level, achieving a sensitivities of 0.136 pm/mm and 1.491 pm/mm, respectively. In both setups, a Fabry-Perot-based pressure sensor is used to compensate the atmospheric pressure. In the first case, both sensors should be enhanced, i.e., the softer polymer in a FBG pressure sensor and the thinner diaphragm in a Fabry-Perot pressure sensor could be designed to improve the sensors sensitivities and reduce the measurement errors. In the case of cantilevers, these kind of structures are not suitable for long liquid level range due to the difficult implementation. Since the liquid level sensitivities of the FOLLSs presented in Chapter 4 and the current chapter are superior when compared with the obtained in [94, 95], the same concept of atmospheric pressure compensation could be applied with the proposed sensors expecting better performance.

5.6 Conclusion

In this chapter a fiber optic level sensor based on a silica FBG technology embedded in an epoxy diaphragm was presented. A mathematical model was developed in order to analyze the induced pressure Bragg wavelength shift, which is related with the changes of the liquid level. A sensitivity of 2.74 pm/mm was determined experimentally, very similar to the one predicted by the simulation model (2.8 pm/mm). The sensor was experimentally tested and highly linear response to the liquid level was observed. The maximum level measured and tested was 500 mm, limited by the experimental setup, nonetheless the sensor is expected to work for higher liquid levels. Using an additional reference temperature FBG-based sensor, it was possible to compensating the temperature cross-sensitivity, achieving a value of 1.04 mm/°C enhancing the liquid level measurement and thermal stability by a factor of 9, when compared to a single sensor head configuration in literature [107]. A pressure plant was used in order to validate the maximum liquid level supported by the sensor. The maximum pressure value achieved without break the sensor was 14 Psi, which corresponds to more than 10000 mm of water level. This configuration can be successfully used in different industrial applications such as chemical processing, fuel storage and transportation systems, oil tanks/reservoirs, and treatment plants, due to the fiber optical sensors advantages.

Chapter 6

Edge-filter Based FBG Interrogator Using an In-fiber FPI micro-cavity

6.1 Introduction

FBGs backscattered spectrum shifts are by far the most used for measuring temperature and/or mechanical strain [71, 133]. Nonetheless, interrogation system are the most important drawback for their large commercial application, due to their high cost. Therefore, the development of new, and lower cost, interrogation alternatives are essential [119]. In this chapter a simple, compact, and stable in-line solution based on catastrophic fuse effect micro-cavity interferometers [129, 134] for fast FBG interrogation is presented. In this alternative solution the frequency-to-amplitude conversion of edge-filtering is performed, where the FBG spectrum goes through a slightly detuned broader filter, role usually performed by a FPI. In this technique, FBG's spectral variations are straightforwardly translated into optical power variations [108, 109, 135]. The micro-cavity process fabrication was already addressed in Chapter 3, where the in-line FPI was used as a FOLLS. At this time, its role is acts like an edge-filter instead as a sensor. FGB strain and temperature measurements are then presented to demonstrate, for the first time, the potential of these high contrast micro-cavities for building interrogation systems with high stability and repeatability.

6.2 Operation Principle

The principle of operation of the low cost FBG interrogator is depicted in Figure 6.1. The proposal setup is based on an amplified spontaneous emission (ASE) broadband light source (BBS) from 1520 nm to 1580 nm with -20 dBm of optical power (ALS-CL-17-B-FA, Amonics), one optical splitter 90/10 (F-CPL-B12351-FCAPC, Newport), two optical circulators (CIR-3-SCL-1-FA, OeMarket), one Peltier with its temperature controller (TEC), and two optical power meters (OPMs) OPM5 from AFL. The ASE signal is launched to the splitter, where 10% of the optical power is acquired by the first OPM which is used as a reference signal to compensate the ASE's fluctuations. The other 90% of optical power is launched into the FBG by using an optical circulator. The backscattered spectrum from the FBG is coupled to the in-line FPI by using a second optical circulator. Thus, the resulting optical power (Output), after crossing both the FBG and FPI, is detected by a second OPM. The in-line FPI micro-cavity is housed in a cooper structure to reduce external mechanical deformation and vibration. This special micro-cavity conveniently shows low temperature sensitivity compared to FBG's [129] regarding wavelength shift features. However, a temperature control (in a simple configuration just to keep the temperature constant) is used to improve the interrogation accuracy of this FPI-based method. Therefore, only the FBG will be exposed to external perturbations, which induces fiber Bragg wavelength shifts, which will be translated into output optical power variation by the FPI.

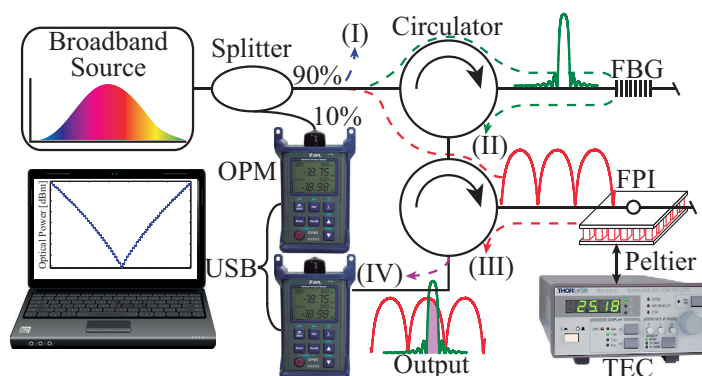


FIGURE 6.1: Setup for FPI-based low cost FBG interrogator. OPM: optical power meter, USB: universal serial bus, FBG: fiber Bragg grating, FPI: Fabry-Perot interferometer, TEC: thermoelectric controller.

6.3 Interrogator Experimental Implementation and Analytical Modeling

A 10 mm length FBG was selected to get more than 90% of reflectivity (see Chapter 2). The FPI micro-cavity was fabricated with the same process as presented in Chapter 3. Figure 6.2(a) shows the in-line FPI micro-cavity using an electronic microscopy with amplification of x50. An approximation of the cavity dimensions took from the image are $80.06 \mu\text{m}$ width, and $122.8 \mu\text{m}$ high. As is depicted in Figure 6.2(b), the spectrum of the micro-cavity acquired by a FBG interrogator Micron Optics SM125 with 1 pm of resolution, presents two important characteristics which enables it as an edge filter interrogator: the high contrast (23 dB) and a regular amplitude pattern. Furthermore, the spectrum allows estimating the actual length micro-cavity for modeling purposes with higher accuracy when compared with the dimensions taken by image due to the errors generated by the focus of the microscope over the micro-cavity.

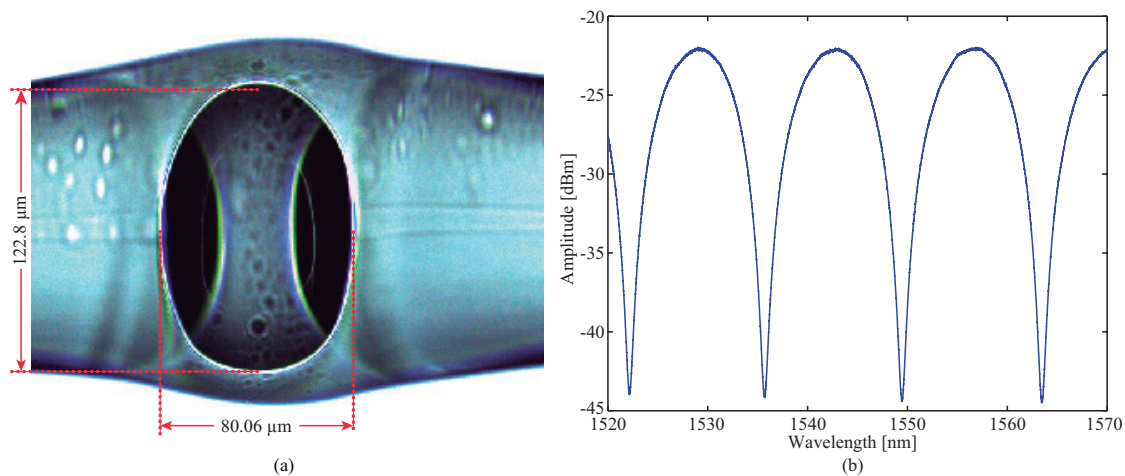


FIGURE 6.2: In-line FPI micro-cavity: (a) FPI electronic microscopy image of x50, (b) backscattered spectrum of the FPI.

Figure 6.3 shows the optical spectrum (OSA with 50 pm resolution) of individual components, as well as their combined effects, in this low cost FBG interrogator. First, it can be observed the input ASE with 60 nm of spectral bandwidth, and -20 dBm of optical power (I). Second, the ASE through the first circulator and the FBG sensor response was acquired. The Bragg wavelength of the FBG sensor is centered at 1546.92 nm with 20 dB of contrast (II). Third, The ASE signal goes to

the second circulator, and to the FPI operating in reflection mode (III). Finally, all devices were combined and the output spectrum was obtained, which is the result of both FBG and FPI spectra filtering (IV).

As can be observed in Figure 6.3, the interrogation range (highlighted from 1543.4 nm to 1549.4 nm) is limited by to 50% of the FPI FSR, due to the periodicity of the spectrum of the FPI. Considering a standard FBG sensor, which has a strain sensitivity around to $1.2 \text{ pm}/\mu\text{Strain}$, the edge-filtering technique allows stressing the FBG sensor nearly to $5000 \mu\text{Strain}$. It is more than the maximum value of strain supported by a standard FBG sensor. Due to the FBG sensor being centered at 1546.92 nm , in this case the maximum value of measurable strain is around $2000 \mu\text{Strain}$.

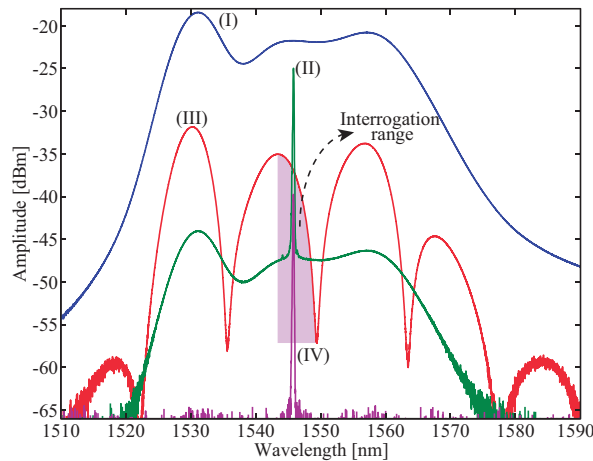


FIGURE 6.3: Spectrum of the proposed interrogation system, acquired by an OSA.

6.3.1 Analytical modeling

In Chapter 2 the analytical modeling of both FPI and FBG sensors were addressed where the backscattered optical power equations were deduced. In order to analyze the behavior of the proposed system interrogation, the FPI micro-cavity spectrum is kept constant and the FBG sensor is exposed to temperature and strain changes.

As is showed in Figure 6.1, the FPI's reflected spectrum is used in the system as an edge filter. By using the Equation 2.18 the portion of incident intensity that is

reflected by the micro-cavity can be rewrite as:

$$\frac{I_r}{I_i} = \zeta R_{r,\delta} = \hat{R}_{r,\delta}, \quad (6.1)$$

where ζ is an adjustment constant.

Figure 6.4 shows the normalized micro-cavity spectra of both analytical (dashed line) and the acquired by the FBG interrogator (solid line). The parameters used in the simulation were $L = 83.4\mu\text{m}$, $R = 0.45$, and $n = 1.0404$. The adjustment constant found was $\zeta = 0.52$. The minor differences can be attributed to the FPI simple model based on plane reflectors. As can be seen in Figure 6.2(a) the micro-cavity is actually an ellipsoid but the simplified model yields accurate results for most of the spectrum.

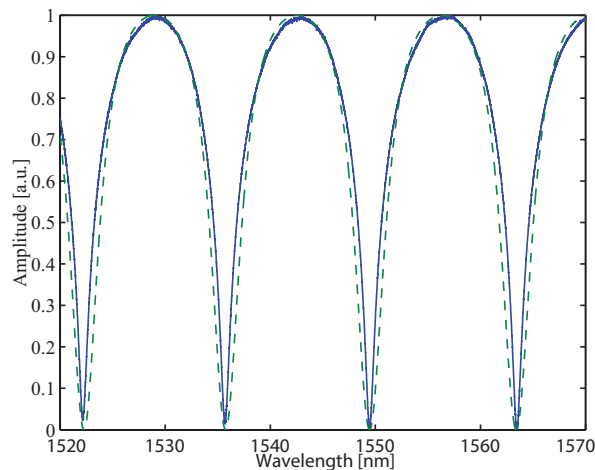


FIGURE 6.4: FPI simulation vs normalized spectra of the micro-cavity.

By applying Equation 2.22 the FSR obtained was 13.417 nm, in agreement with the resulting FSR measured from the FPI spectrum ~ 13.644 nm. The FPI is evidently sensitive to both strain (as presented in Chapter 2) and temperature variations, as will be show experimentally later on, but the corresponding modeling will not be performed for FPI as it will be kept under controlled conditions. Therefore, the FBG will be the sensor for these physical variables. The Bragg wavelength selected is the same as measured with the OSA in Figure 6.3 (1546.96 nm).

As discussed in Chapter 2, the FBG simulations were performed with both effects decoupled one from each other. The strain simulation was performed from 0 μStrain

to 1440 μStrain changed in 40 μStrain steps and the temperature simulation was performed from 5 $^{\circ}\text{C}$ to 50 $^{\circ}\text{C}$ changed in 5 $^{\circ}\text{C}$ steps.

The output of the FPI edge-filtering interrogation system can be seen as the combined effect of the FBG and the micro-cavity spectra, which means the product between Eq. 6.1 and Eq. 2.32. Then, the representation in the optical domain can be written as:

$$I_{Output} = R_{L,\lambda} \hat{R}_{r,\delta}. \quad (6.2)$$

Figure 6.5 depicted the red-shift FBG spectra of the strain simulation before (a) and after (b) the FPI edge-filtering effect. FBG reflectivity is around 93% and the shape of the edge filter induce an amplitude variation over the FBG spectrum resulting on a optical power change when the FBG sensor is stressed. The same effect over the FBG spectrum is observed when the temperature is altered. Because the simple interrogation is based on optical power measurement, it is necessary to integrate I_{Output} in order to obtain the detected optical power value.

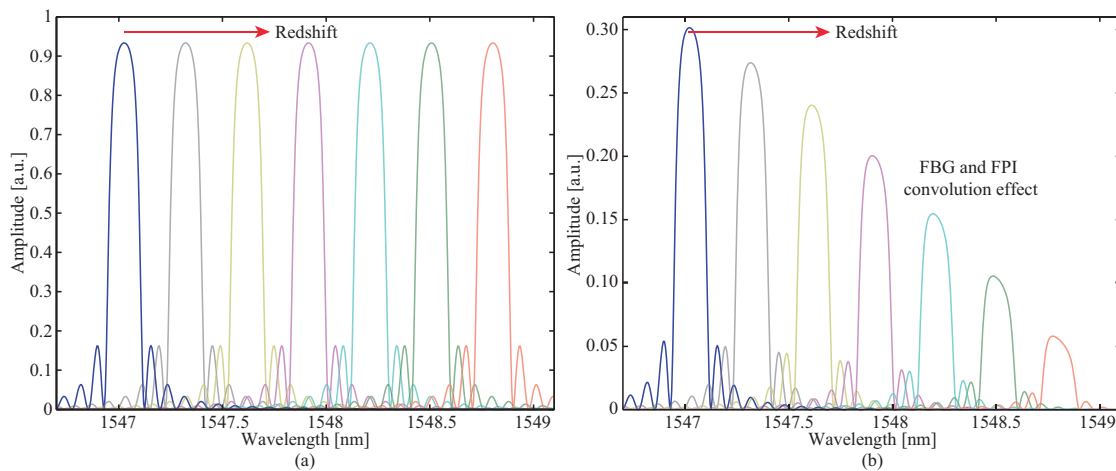


FIGURE 6.5: Simulation for the FBG strain variation (a) and (b) the corresponding FPI edge-filtering.

6.4 Experimental Apparatus for Characterization

First, the micro-cavity FPI and the FBG were characterized individually by using an interrogator Micron Optics SM125 with maximal resolution of 1 pm, and one temperature control system composed by one thermoelectric temperature controller

(TEC), and one temperature sensor header (TSH) based on Peltier effect (Figure 6.6). Second, the temperature response of the FBG sensor was characterized with the proposed interrogation system (depicted in Figure 6.1) by using two temperature systems, one for the FBG sensor which allows changing the FBG temperature and the second one for the micro-cavity which allows its temperature stabilization.

As can be observed in Figure 6.6, the TSH has 2 cooper platforms (top and front view). The Peltier support platform (PSP) has an U shape in order to house the Peltier and allows fixing the OFS extremities in a central longitudinal fringe (fixed points in top view). The sensor holder platform has rectangular shape and houses either the FPI micro-cavity or the FBG sensor, centered in a longitudinal fringe, which is aligned with the PSP fringe. The thermocouple (temperature reference sensor) is housed in a transversal fringe which is covered with a thin cooper sheet to create a chamber and avoid external perturbation. As it is well known, the Peltier has 2 sides with different temperatures, one face cold and the other one hot. The heat transfer process can be controlled by the current which feeds the Peltier module. The Peltier is sandwiched between both platforms which in turn are anchored by 4 nylon screws to avoid the temperature transference between them (evidenced in front view). In order to improve the heat transfer between the components (FBG, thermocouple and Peltier) with both the sensors holder and the Peltier support platforms, thermal paste was used. The TEC used was the TED200C by Thorlabs which allows high resolution, accuracy, and stability of $0.01\text{ }^{\circ}\text{C}$, $\pm 0.1\text{ }^{\circ}\text{C}$, and $< 0.002\text{ }^{\circ}\text{C}$, respectively.

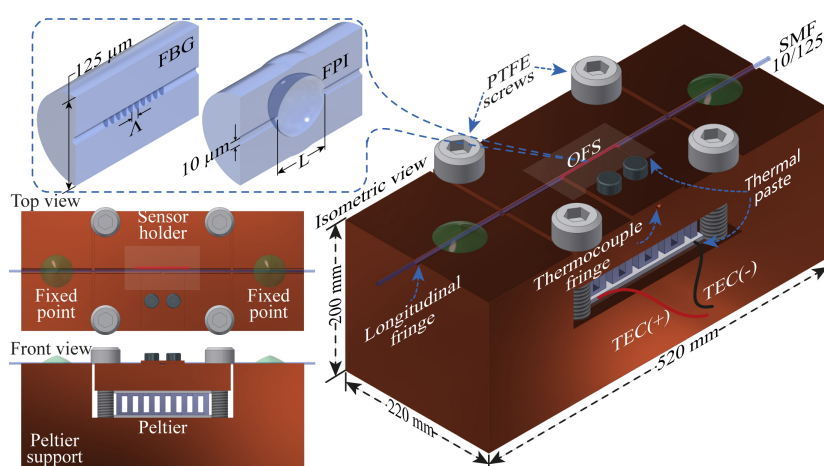


FIGURE 6.6: Temperature sensor header. FBG: Fiber Bragg grating, FPI: Fabry-Perot interferometer, PTFE: Polytetrafluoroethylene, OFS: optical fiber sensor, SMF: single mode fiber, TEC: thermoelectric controller.

A strain characterization of the FBG sensor, with the proposed interrogation system, was performed using the setup showed in Figure 6.7. The FBG sensor was fixed with Cyanoacrylate glue in its extremities between a rigid fixed platform and a linear axial translation stage. The selected distance between anchorage points was 250 mm. In order to improve the adhesion between the anchorage points and the platforms, the fiber acrylate protection was removed around these points. The strain characterization was performed from 0 μm to 360 μm by increasing the linear axial translation stage in steps of 10 μm , which means a strain response from 0 μStrain to 1440 μStrain in steps of 40 μStrain .

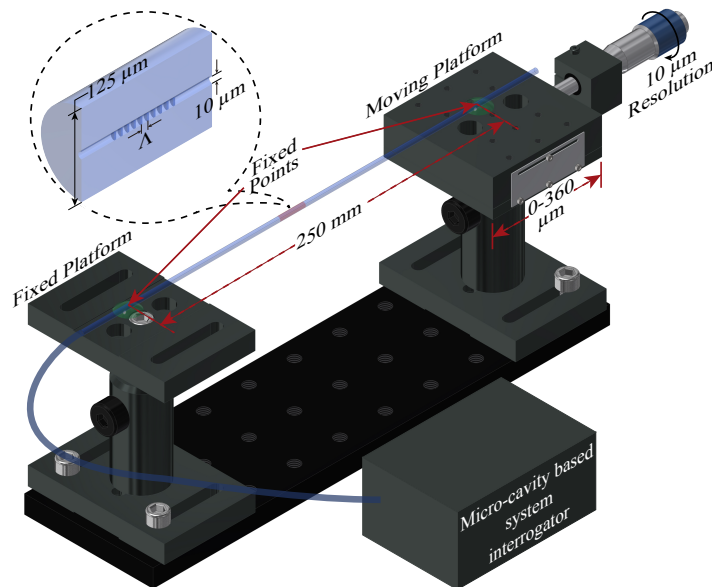


FIGURE 6.7: Setup for strain characterization of the FBG sensor.

6.5 Results

Figure 6.8 depicts temperature response, in terms of wavelength shift and amplitude, for both FPI micro-cavity and FBG sensor. The wavelength variations for both are represented by dashed lines whereas amplitude variations are presented with solid lines. As it is expected, the FBG sensor has a linear response, with a sensitivity of 9.62 pm/ $^{\circ}\text{C}$ with a coefficient of determination $R^2 > 0.998$ which agrees with the standard FBG sensor simulation (9.55 pm/ $^{\circ}\text{C}$). In contrast, the FPI sensor presents low temperature sensitivity around ± 0.55 pm. The amplitude variations for FBG is around ± 0.1 dB. For temperature range from 5 $^{\circ}\text{C}$ to 30 $^{\circ}\text{C}$ a mean FPI sensitivity

is around ± 0.025 dB. However, for higher temperatures values than 30 °C the FPI sensor showed an amplitude decrease around 0.6 dB. Therefore, in order to avoid temperature variations, impacting the measurement accuracy of the interrogation system, it is recommended the use of a temperature control.

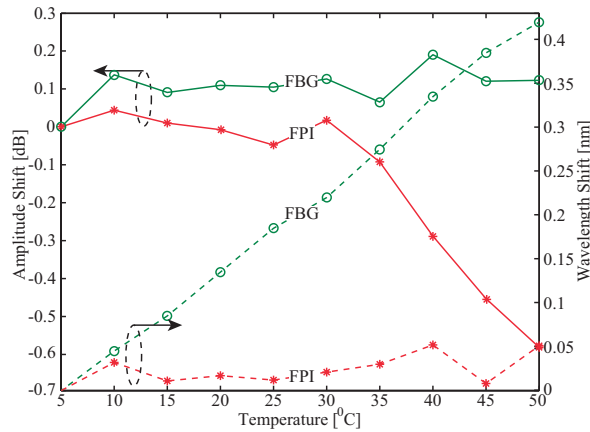


FIGURE 6.8: Temperature characterization of FPI and FBG.

Figure 6.9 presents both the experimental and simulated results of strain and temperature using the analytical model. As predicted by the analytical model (solid lines), the optical power variation is not linear due to the shape of the edge filter. To characterize both the temperature and the strain responses of the FBG sensor, the temperature of the micro-cavity was maintained constant at 25 °C. The experiment performed for temperature characterization consisted in changing the temperature from 50 °C to 5 °C in 5 °C steps. The strain characterization was performed from 0 μ strain to 1440 μ Strain in 40 μ strain steps. As observed in Figure 6.9 the analytical model predicts very closely the experimental response of the proposed interrogation system with a root mean square error (RMSE) of 0.045 and 0.014 for strain and temperature, respectively.

Because the system interrogation is based on optical power measurements, there are ASE temporal fluctuations that needs to be compensated. As presented in Fig. 6.1, 10% of the input signal was used for the reference arm.

To test repeatability and stability, temperature variations from and ~ 50 °C to ~ 5 °C and back to ~ 50 °C, were performed. Each step lasts 300 seconds with an OPM's acquisition rate at 2 samples per second. Figure 6.10(a) illustrates the ASE fluctuations over the output signal and its compensation in one cycle of the temperature

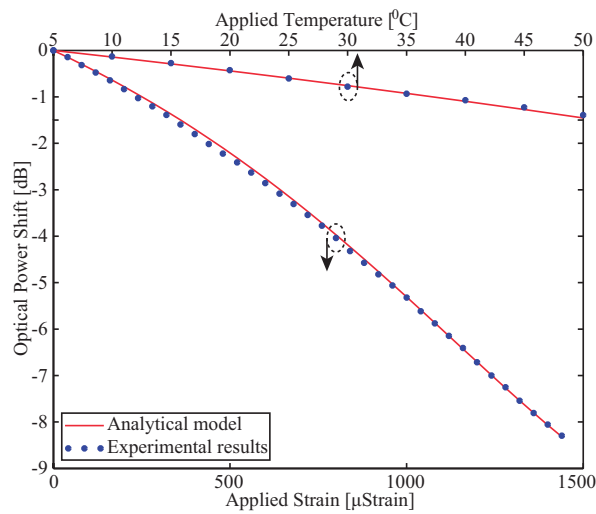


FIGURE 6.9: Analytical and experimental results of Strain and temperature measurements with the proposed interrogation system.

characterization. Otherwise, ASE power variations will induce errors over the temperature measurement (uncompensated curve). By using the information of the reference signal it is possible to reduce the temperature measurement error to obtain a stable temperature response (compensated). Figure 6.10(b) shows the temperature response for both measurement cycles. The compensated measurement remained stable along the steps, and the up and down temperature semi-cycles staircase meet at midpoint. The former shows evidences for stability whereas the latter repeatability of the proposed interrogation system.

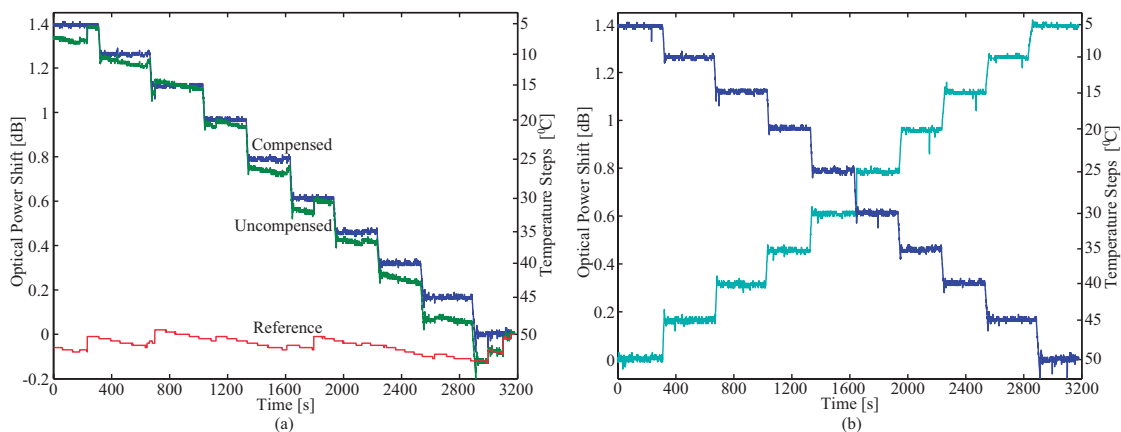


FIGURE 6.10: (a) up temperature characterization with ASE compensation and (b) up and down temperature response using the proposed interrogator.

The interrogation range of the proposed interrogation system is limited by half FSR of the micro-cavity (from 1543.4 nm to 1549.4 nm). If the strain or temperature variations are limited, it is convenient selecting a Bragg wavelength over the edge filter with higher sensitivity. Figure 6.11 compares two FBG sensors exposed to the same strain values. As expected, the FBG centered at 1545.82 nm shows lower sensitivity when compared with the FBG centered at 1546.92 nm because the second one is positioned over a higher slope of the micro-cavity spectrum allowing more sensitivity.

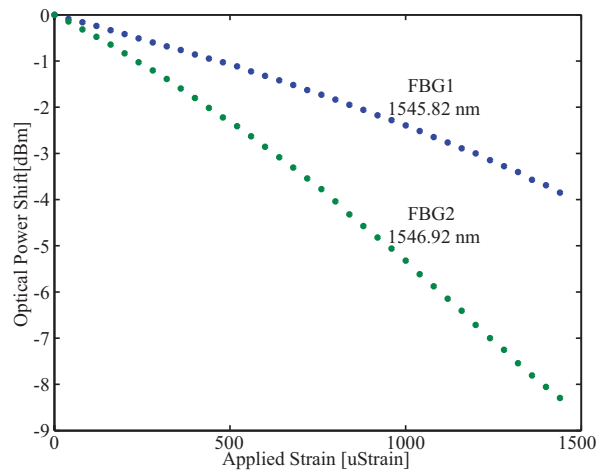


FIGURE 6.11: Strain comparison between two FBG sensors using the proposed interrogator.

6.6 Discussion

Table 6.1 summarizes relevant characteristics of edge-filter schemes in the state-of-the-art and the proposed approach. As it can be observed, the highest sensitivity is achieved with matched FBG-based filters, at a cost of very limited dynamic range. The most equilibrated relation between visibility and dynamic range is achieved with the proposed edge-filter. During the fabrication process it is possible to optimize the visibility and the FSR if the spectrum is monitored. In addition, the characteristic periodic spectrum and cost-effective fabrication make of the proposed edge-filter an excellent candidate to interrogate several FBGs by means of TDM, WDM or both techniques, with an unique micrometer size device, avoiding several matched FBG pairs, LPGs, CFBG and TFBG, or a large length of fiber used to create the edge-filter, as presented in the state-of-the-art.

TABLE 6.1: Comparison of relevant parameters of several edge-filter schemes and the proposed approach.

Sensor	Visibility [dB]	Dynamic range [nm]	Repeteability	Cost
This work	23	6	Medium	Very low
Tiwari, et al. [119]	10	10	High	Low
Wei, et al. [120]	2.8	2	High	Low
Yan, et al. [113]	>25	0.1	Very High	High
Rao, et al. [118]	~ 25	9	Very High	High
Deepa, et al. [115]	> 20	0.5	Very High	High

Although, in this test case, the system interrogation is composed by some expensive components, such as power meters, TEC and ASE source. As presented in [136] the OPMs have been replaced by lower cost photodetectors, which are amplified by an operational amplifiers (Op-Amp) in transimpedance configuration and are acquired by an analog to digital converter (ADC) module. This first modification leads to a considerably cost reduction. Nowadays, Op-Amp offers high bandwidth with high signal-to-noise (SNR) ratio allowing to sample high frequency signals around hundreds of MHz [137]. In addition, novel electronic devices such as microcontrollers allow sampling rate up to 500 ksps with 16 bits resolution for several channels with prices that oscillate from some to tens of dollar [138]. On the other hand, a simple electronic controller to keep the temperature constant can replacing the TEC used in this experimental implementation (TED200C), due to there is no need to change temperature with control. Ultracompact Thermoelectric Cooler (TEC) Controllers are the best solution in a single chip. This electronic devices offers extremely good long-term temperature stability which is maintained via an autonomous analog temperature PID control loop and the use of zero drift chopper amplifiers [139]. Finally, a smaller and lower cost optical source, such as a superluminescent diode (SLED) illuminating just the spectral region of interest can be used. The capabilities of this interrogation technique for dynamic measurement was already addressed in [136]. When dynamic applications are required, the issues related with temperature cross-sensitivity can be neglected or filtered with a bandpass filter, due to the temperature variations happens at a much lower frequencies than dynamic variations (frequencies > 1Hz).

Despite being suitable for dynamic measurements, the proposed approach presents

a limitation in the numbers of sensors that could be interrogated and the individual sensor resolution. Commercial interrogators offer solutions with several channels where tens of FBGs can be interrogated per each channel. In the case of interrogators based on scanning laser or scanning filters a resolution of 1 pm is commonly achieved, with scanning frequency varying from some Hz to tens of kHz. Alternatives solutions based on spectrometers allows even more interrogation speed with the price of just one channel but with same resolution. On the other hand, for specific applications where few FBGs and high rates are required the proposed interrogation system can be seen as an alternative and suitable cost-effective solution [136].

6.7 Conclusions

By recycling an optical fiber damaged by the catastrophic fuse effect, a cost effective fiber Bragg grating interrogator system based in an in-fiber FPI micro-cavity was built. The spectral characteristics of high visibility (23 dB) and a half FSR of 6 nm enabled the FPI micro-cavity to be used as an edge filter. The strain and temperature of the FBG sensor were measured from 0-1440 μ Strain and 5 °C to 50 °C, respectively, showing evidences of high repeatability and stability. Nevertheless, due to the 6 nm interrogation range, it is possible measuring a maximum strain of 5000 μ Strain and a temperatures of 600 °C which are values more that a standard FBG can supports. A trade-off between resolution and dynamic range was observed due to the nonlinear spectrum filter shape. The behavior of the interrogation response is very similar to the one predicted by the analytical model achieving a RMSE of 0.045 and 0.014 for strain and temperature, respectively. On the other hand, by changing the detection stage (OPMs) by lower cost photodetectors, it is possible to use the proposed approach for dynamic measurements.

Chapter 7

Conclusions and Future Work

7.1 Summary

The Thesis goal was to push forward new proposals for improving the relevant aspects in measuring liquid level. Intrinsic safety concerns in harsh environments, especially those with corrosive, and explosive or flammable atmospheres can be solved with optical in-fiber sensing. A large group of FOLLS to monitor this important parameter was discussed in the state-of-the-art and our contributions focused on three specific technologies: MZI, FPI and FBG. One chapter was dedicated for advances in sensors based on each of those technologies and another one combining FBG e FPI for a cost-effective interrogation system. Our outcomes were compared with similar FOLLS in order to highlight the scientific contributions, leading to publications in international journals and conferences.

In Chapter 2 were introduced key concepts of optical fiber sensors and a review of the state-of-the-art, focusing on the in-fiber MZI, the in-fiber FPI and the FBG sensors. One section was dedicated for each sensor, where the operational principle and the mathematical model were presented. The knowledge of this information is crucial to understand how the sensor works and what is expected from the experimental results.

Chapter 3 introduced an in-fiber MZI for liquid level measurement. This based-SRI sensor is a cost effective solution which is fabricated with a standard splicing machine and different kinds of optical fibers. No specialized setup is required to construct the sensor arrangement and a medium repeatability is achieved when

compared with other matured technologies, specifically FBG sensors. The key contribution of this chapter is not the sensor fabrication itself, despite being an alternative structure. As presented in the state-of-the-art, all the interrogation techniques are based on the tracking of individual peaks/dips of the transmitted spectrum. To highlight in this chapter, a novel interrogation technique based on the tracking of the envelope spectrum instead one peak/dip is introduced. A 120 mm sensor length was analyzed with both techniques, where was improve the resolution by more than an order. By tracking a dip centered at 1537.70 nm, a sensitivity of 2.29 pm/mm was achieved. On the other hand, by applying the envelope technique a sensitivity of 34.65 pm/mm was achieved. In addition, the traditional technique is limited to measure short sensor lengths, since, for large sensor length the FSR is reduced avoiding the correct identification of dip/peak shift when the sensor is immersed into the liquid.

In Chapter 4, another interferometer was proposed to measure liquid level. A low cost fabrication process was employed, where a standard splicing machine, a SMF and a fiber destroyed by the catastrophic fuse effect, were used to fabricate the in-fiber FPIs. This sensors exhibit high strain sensitivity and low temperature cross-sensitivity when compared with FBG sensors. Several FPIs were characterized for strain achieving sensitivities from 1.63 pm/ $\mu\epsilon$ to 3.31 pm/ $\mu\epsilon$, which are higher than standard FBG offers (~ 1.2 pm/ $\mu\epsilon$). With the criteria of maximum sensitivity just three sensors were characterized for temperature. The temperature sensitivity was experimentally determined as 2.4 pm/ $^{\circ}\text{C}$ which is several orders lower than standard FBG (~ 9 pm/ $^{\circ}\text{C}$). In the proposed approach in this work, the cavity is embedded into a polyurethane resin diaphragm of 1.1 mm wall height and 50 mm diameter, where 900 mm of liquid level was measured achieving a maximum sensitivity of 4.7 pm/mm. In addition, was necessary a temperature compensation because the diaphragm configuration increases considerably the temperature cross-sensitivity to ~ 61 pm/mm.

Notwithstanding the axial strain robustness offered by the micro-cavities, the transversal deformation over the diaphragm when exposed to liquid pressure, imposes both an axial strain over the fiber and a transversal deformation over the micro-cavity. Since, the micro-cavity has thin walls on transversal direction, it makes the sensor more fragile for this kind of applications. This inherent disadvantage can be solved with thicker diaphragms, which will reduce the sensor sensitivity.

An alternative solution was introduced in Chapter 5. By keeping the simple and cost-effective fabrication process of diaphragm-based sensors, a FBG sensor is embedded into the diaphragm instead the FPI micro-cavity. In this experimental setup an industrial plant was used and it is possible to measure liquid level under temperature variations. As expected, a temperature cross-sensitivity needs to be compensated. The adopted strategy is the same used in Chapter 4, a second FBG sensor shielded from external strain is used as a temperature reference sensor, by knowing the sensitivity of both sensors, reference and diaphragm, it is possible to decouple this undesired effect over the liquid level measurement. A sensitivity of 2.74 pm/mm was achieved. Beside, this configuration is more robust than the micro-cavity, thus, a pressure test up to 14 Psi was performed, which is equivalent to 10542 mm of liquid level.

The Table 7.1 summarizes the advantages and disadvantages between the sensor technologies studied in this Thesis. As expected the highest resolution was achieved with the MZI-based sensor. The highest temperature sensitivity was obtained with the diaphragm-based FPI sensor. Therefore, the temperature cross-sensitivity needs to be compensated. Despite the highest level sensitivity was obtained with the MZI, its resolution is limited by the OSA, which has 30 pm resolution. As observed in Table 7.1 the MZI of 470 mm length does not comply the Resolution requirement. Therefore, a trade-off between Range and both sensitivity and linearity is an inherent characteristic of this sensor.

The level range is limited by each setup, been the FPI the largest one. Both configurations tested with this sensor accomplish the resolution parameter. In terms of robustness, the FBG technology is better since no splicing process is performed. However, with the phase mask technique, the coating protection layer needs to be removed in the section where the FBG is recorded. In the point of view of cost fabrication no specialized setup is required to construct the interferometer sensors, however the repeatability is lower when compared with FBG. The interrogation cost is considerably improved for FPI and FBG sensors with the setup presented in Chapter 6, with the price of just one sensor can be interrogated at time.

Finally, in Chapter 6, a low cost interrogation for FBG sensors was presented. However, this technique can be also used to interrogate FPI sensors. The main advantages of this scheme were discussed and compared with similar techniques on the state-of-the-art. The main component on this approach is the FPI micro-cavity. Its

TABLE 7.1: Comparison of several parameters between the studied sensors.

Sensors	MZI	FPI	FBG
Level sensitivity [pm/mm]	33.75/17.17	4.71/1.83	2.74
Temperature sensitivity [pm/°C]	39	61	43.2
Resolution [mm]	0.88/1.76	0.21/0.54	0.36
Level [mm]	120/470	900	500
Robustness	low	medium	high
Cost effectiveness	low	high	high
Fabrication repeatability	low	low	high
Simplicity	high	high	low
Thermal cross-sensitivity	not compensated	compensated	compensated

high visibility, large dynamic range, periodicity, and cost effective fabrication, are the key characteristics to highlight, which become it as an excellent candidate to perform the edge-filtering task.

7.2 Future Work Perspectives

An interesting focus is proposes models in order to explain the interaction of high order modes with the SRI for the in-fiber MZI. As presented in Chapter 3, the envelope presents a redshift instead a blueshift as occurs with the individual peaks or dips of the whole spectrum. An hypothesis was suggested in Chapter 3, however, there is need for mathematical modeling to support this hypothesis. The complex interaction of high order modes in a three layer scheme is not a trivial task. In addition, with the inclusion of new optical fibers it is possible to propose new sensor arrangements, where several spectrum characteristics could be improved. Finally, cost-effective interrogation techniques may be addressed. Despite this sensors are extremely sensitivity, an OSA is usually used to interrogate them, which has several limits as was already discussed. Alternative processing signals could leads to novel interrogation techniques avoiding the use of OSA, allowing, portability, dynamic measurements and reduced cost.

For diaphragm-based sensors, multi-parameter measurements could be addressed. In application where the liquid does not have the same density, for instance in oil

tanks, where water, emulsion and oil are presented in the same tank, a system with several sensors could be a solution to detect the water–emulsion–oil interface layers, with high precision. In addition, diaphragm materials and different sensor heads configuration could be implemented. This can be done in order to improve parameters such as sensitivity and dynamic range. Furthermore, pressure sensors can be applied in several fields as reported in the state-of-the-art. The main drawback of the FBG or FPI sensors is the interrogation technique, which usually is expensive and limited for dynamic measurements. Therefore, research in that direction will allow to explore new applications of this kind of optical fiber sensors.

Finally, the proposed interrogator technique has two fronts. First, it is necessary improve the fabrication process of the edge–filters. Despite, the cost–effective fabrication is achieved, the repeatability is not comparable with matured process fabrication such as FBG recording process offers. To improve the actual methodology, it is suggested monitoring the reflected spectrum during fabrication process. By tracking spectrum changes could be created similar micro–cavities, which leads to similar spectral characteristics. Second, since this kind of micro–cavities present a periodic optical power modulation, the proposed interrogation technique could be expanded with TDM and WDM techniques to monitor dynamically several FBG sensors.

Doctoral Thesis written by —
Camilo A. R. Díaz

Bibliography

- [1] D. Sengupta and P. Kishore, "Continuous liquid level monitoring sensor system using fiber bragg grating", *Optical Engineering*, vol. 53, no. 1, p. 017 102, 2014. DOI: [10.1117/1.OE.53.1.017102](https://doi.org/10.1117/1.OE.53.1.017102).
- [2] B. Jin, X. Liu, Q. Bai, D. Wang, and Y. Wang, "Design and implementation of an intrinsically safe liquid-level sensor using coaxial cable", *Sensors*, vol. 15, no. 6, pp. 12 613–12 634, 2015, ISSN: 1424-8220. DOI: [10.3390/s150612613](https://doi.org/10.3390/s150612613).
- [3] D. Song, J. Zou, Z. Wei, Z. Chen, and H. Cui, "Liquid-level sensor using a fiber Bragg grating and carbon fiber composite diaphragm", *Optical Engineering*, vol. 50, no. 1, pp. 014 401–5, 2011. DOI: [10.1117/1.3525286](https://doi.org/10.1117/1.3525286).
- [4] L. Li, L. Xia, Z. Xie, and D. Liu, "All-fiber Mach-Zehnder interferometers for sensing applications", *Opt. Express*, vol. 20, no. 10, pp. 11 109–11 120, May 2012. DOI: [10.1364/OE.20.011109](https://doi.org/10.1364/OE.20.011109).
- [5] T. Zhu, D. Wu, M. Liu, and D.-W. Duan, "In-line fiber optic interferometric sensors in single-mode fibers", *Sensors*, vol. 12, no. 8, pp. 10 430–10 449, 2012, ISSN: 1424-8220. DOI: [10.3390/s120810430](https://doi.org/10.3390/s120810430).
- [6] H.-P. Chang, C.-M. Li, C.-L. Lee, and J.-M. Hsu, "Tapered fiber Mach-Zehnder interferometer for liquid level sensing", *Session 3A4 Design and Simulation of Electromagnetic and Optical Devices*, p. 446, 2013.
- [7] B. H. Lee, Y. H. Kim, K. S. Park, J. B. Eom, M. J. Kim, B. S. Rho, and H. Y. Choi, "Interferometric fiber optic sensors", *Sensors*, vol. 12, no. 3, pp. 2467–2486, 2012. DOI: [10.3390/s120302467](https://doi.org/10.3390/s120302467).
- [8] A. D. Kersey, M. A. Davis, H. J. Patrick, M. LeBlanc, K. Koo, C. Askins, M. Putnam, and E. J. Friebele, "Fiber grating sensors", *Journal of lightwave technology*, vol. 15, no. 8, pp. 1442–1463, 1997.
- [9] G. Kouroussis, D. Kinet, E. Mendoza, J. Dupuy, V. Moeyaert, and C. Caucheteur, "Edge-filter technique and dominant frequency analysis for high-speed railway monitoring with fiber bragg gratings", *Smart Materials and Structures*, vol. 25, no. 7, p. 075 029, 2016.

- [10] B. Lee, "Review of the present status of optical fiber sensors", *Optical Fiber Technology*, vol. 9, no. 2, pp. 57–79, 2003, ISSN: 1068-5200. DOI: [http://dx.doi.org/10.1016/S1068-5200\(02\)00527-8](http://dx.doi.org/10.1016/S1068-5200(02)00527-8).
- [11] IEC, *Explosive atmospheres - part 28: Protection of equipment and transmission systems using optical radiation*, 2015 (accessed May 15, 2018). [Online]. Available: https://webstore.iec.ch/preview/info_iec60079-28%7Bed2.0.RLV%7Den.pdf.
- [12] ———, *Safety of laser products – part 1: Equipment classification, requirements and user's guide*, 2001 (accessed May 15, 2018). [Online]. Available: https://shop.textalk.se/shop/ws26/40626/files/full_size_-_for_start_page_banner/iec60825-1%7Bed1.2%7Den.pdf.
- [13] C. A. Rodríguez, M. R. N. Ribeiro, A. Frizera-Neto, C. E. S. Castellani, and M. J. Pontes, "Envelope-based technique for liquid level sensors using an in-line fiber mach-zehnder interferometer", *Appl. Opt.*, vol. 55, no. 34, pp. 9803–9809, Dec. 2016. DOI: [10.1364/AO.55.009803](https://doi.org/10.1364/AO.55.009803).
- [14] C. A. R. Díaz, A. G. Leal-Junior, P. S. B. Andrdé, P. F. d. C. Antunes, M. J. Pontes, A. Frizera-Neto, and M. R. N. Ribeiro, "Liquid level measurement based on FBG-embedded diaphragms with temperature compensation", *IEEE Sensors Journal*, vol. 18, no. 1, pp. 193–200, Jan. 2018, ISSN: 1530-437X. DOI: [10.1109/JSEN.2017.2768510](https://doi.org/10.1109/JSEN.2017.2768510).
- [15] C. A. R. Díaz, C. A. F. Marques, M. F. F. Domingues, M. R. N. Ribeiro, A. F. Neto, M. J. Pontes, P. S. André, and P. F. C. Antunes, "A cost-effective edge-filter-based FBG strain interrogator using catastrophic fuse effect microcavity interferometers", in *Proc.SPIE*, vol. 10528, 2018, 105281W–4. DOI: [10.1117/12.2291042](https://doi.org/10.1117/12.2291042).
- [16] C. A. Díaz, C. A. Marques, M. F. F. Domingues, M. R. Ribeiro, A. Frizera-Neto, M. J. Pontes, P. S. André, and P. F. Antunes, "A cost-effective edge-filter based FBG interrogator using catastrophic fuse effect micro-cavity interferometers", *Measurement*, vol. 124, pp. 486–493, 2018, ISSN: 0263-2241. DOI: <https://doi.org/10.1016/j.measurement.2018.03.067>.
- [17] G. P. Agrawal, *Fiber-optic communication systems*, 4th ed. WILEY, 2010.
- [18] F. P. Kapron, D. B. Keck, and R. D. Maurer, "Radiation losses in glass optical waveguides", *Applied Physics Letters*, vol. 17, no. 10, pp. 423–425, 1970. DOI: [10.1063/1.1653255](https://doi.org/10.1063/1.1653255).
- [19] R. J. Sanferrare, *AT&T Tech. J.*, pp. 66–95, 1987.

- [20] A. E. Willner, *IEEE Journal of Selected Topics in Quantum Electronics*, vol. 6, p. 827, 2000.
- [21] D. Gloge, A. Albanese, C. A. Burrus, E. L. Chinnock, J. A. Copeland, A. G. Dentai, T. P. Lee, T. Li, and K. Ogawa, "High-speed digital lightwave communication using leds and pin photodiodes at 1.3 μm ", *The Bell System Technical Journal*, vol. 59, no. 8, pp. 1365–1382, Oct. 1980, ISSN: 0005-8580. DOI: [10.1002/j.1538-7305.1980.tb03369.x](https://doi.org/10.1002/j.1538-7305.1980.tb03369.x).
- [22] K. Nakagawa, *IEICE Transactions on Electronics*, vol. J78B, p. 713, 1995.
- [23] G. A. Thomas, B. I. Shraiman, P. F. Glodis, and M. J. Stephen, "Towards the clarity limit in optical fibre", *Nature*, vol. 404, pp. 262–264, Mar. 2000. DOI: [10.1038/35005034](https://doi.org/10.1038/35005034).
- [24] X. Zhou, J. Yu, M. F. Huang, Y. Shao, T. Wang, L. Nelson, P. Magill, M. Birk, P. I. Borel, D. W. Peckham, and R. Lingle, "64-tb/s (640x107-gb/s) pdm-36qam transmission over 320km using both pre- and post-transmission digital equalization", in *2010 Conference on Optical Fiber Communication (OFC/NFOEC), collocated National Fiber Optic Engineers Conference*, Mar. 2010, pp. 1–3.
- [25] V. Vali and R. W. Shorthill, "Fiber ring interferometer", *Appl. Opt.*, vol. 15, no. 5, pp. 1099–1100, May 1976. DOI: [10.1364/AO.15.001099](https://doi.org/10.1364/AO.15.001099).
- [26] J. H. Cole, R. L. Johnson, and P. G. Bhuta, "Fiber-optic detection of sound", *The Journal of the Acoustical Society of America*, vol. 62, no. 5, pp. 1136–1138, 1977. DOI: [10.1121/1.381647](https://doi.org/10.1121/1.381647).
- [27] B. Culshaw, "Optical fibre sensors: A current perspective", *The Open Optics Journal*, vol. 7, no. 1, pp. 21–31, 2013. DOI: [10.2174/1874328501307010021](https://doi.org/10.2174/1874328501307010021).
- [28] Z. Chen, S. Xiong, S. Gao, H. Zhang, L. Wan, X. Huang, B. Huang, Y. Feng, W. Liu, and Z. Li, "High-temperature sensor based on Fabry-Perot interferometer in microfiber tip", *Sensors*, vol. 18, no. 1, 2018, ISSN: 1424-8220. DOI: [10.3390/s18010202](https://doi.org/10.3390/s18010202).
- [29] R. da Silva Marques, A. R. Prado, P. F. da Costa Antunes, P. S. de Brito André, M. Ribeiro, A. Frizera-Neto, and M. J. Pontes, "Corrosion resistant FBG-based quasi-distributed sensor for crude oil tank dynamic temperature profile monitoring", *Sensors*, vol. 15, no. 12, pp. 30 693–30 703, 2015.

- [30] C. A. F. Marques, A. Pospori, D. Sáez-Rodríguez, K. Nielsen, O. Bang, and D. J. Webb, "Aviation fuel gauging sensor utilizing multiple diaphragm sensors incorporating polymer optical fiber bragg gratings", *IEEE Sensors Journal*, vol. 16, no. 15, pp. 6122–6129, Aug. 2016, ISSN: 1530-437X. DOI: [10.1109/JSEN.2016.2577782](https://doi.org/10.1109/JSEN.2016.2577782).
- [31] K. T. Wan and C. K. Y. Leung, "Durability tests of a fiber optic corrosion sensor", *Sensors*, vol. 12, no. 3, pp. 3656–3668, 2012, ISSN: 1424-8220. DOI: [10.3390/s120303656](https://doi.org/10.3390/s120303656).
- [32] K. T. Wan and C. K. Leung, "Durability tests of a fiber optic corrosion sensor", *Sensors*, vol. 12, no. 3, pp. 3656–3668, 2012, ISSN: 1424-8220. DOI: [10.3390/s120303656](https://doi.org/10.3390/s120303656).
- [33] C. A. Rodríguez, M. R. N. Ribeiro, A. Frizera, and M. J. Pontes, "Interrogation of optical fiber based on the fusion of OFDR and TRA techniques", *Optical and Quantum Electronics*, vol. 48, no. 4, p. 230, Mar. 2016, ISSN: 1572-817X. DOI: [10.1007/s11082-016-0501-6](https://doi.org/10.1007/s11082-016-0501-6).
- [34] L. Zhao L. and Jiang, S. Wang, H. Xiao, Y. Lu, and H.-L. Tsai, "A high-quality Mach-Zehnder interferometer fiber sensor by femtosecond laser one-step processing", *Sensors*, vol. 11, no. 1, pp. 54–61, 2011. DOI: <http://doi.org/10.3390/s110100054>.
- [35] G. Bolognini and A. Hartog, "Raman-based fibre sensors: Trends and applications", *Optical Fiber Technology*, vol. 19, no. 6, Part B, pp. 678–688, 2013, *Optical Fiber Sensors*, ISSN: 1068-5200. DOI: <https://doi.org/10.1016/j.yofte.2013.08.003>.
- [36] P. Healey, "Review of long wavelength single-mode optical fiber reflectometry techniques", *Journal of Lightwave Technology*, vol. 3, no. 4, pp. 876–886, Aug. 1985, ISSN: 0733-8724. DOI: [10.1109/JLT.1985.1074281](https://doi.org/10.1109/JLT.1985.1074281).
- [37] L. Palmieri and L. Schenato, "Distributed optical fiber sensing based on Rayleigh scattering", *The Open Optics Journal*, vol. 7, pp. 104–127, 2013, ISSN: 1068-5200. DOI: [10.2174/1874328501307010104](https://doi.org/10.2174/1874328501307010104).
- [38] E. Karamehmedović, "Incoherent optical frequency domain reflectometry for distributed thermal sensing", PhD thesis, Technical University of Denmark, 2009.

- [39] K. Yuksel, M. Wuilpart, V. Moeyaert, and P. Megret, "Optical frequency domain reflectometry: A review", in *2009 11th International Conference on Transparent Optical Networks*, Jun. 2009, pp. 1–5. DOI: [10.1109/ICTON.2009.5185111](https://doi.org/10.1109/ICTON.2009.5185111).
- [40] S. Liehr, "Fibre optic sensing techniques based on incoherent optical frequency domain reflectometry", PhD thesis, Technical University of Berlin, 2015.
- [41] A. Ukil, H. Braendle, and P. Krippner, "Distributed temperature sensing: Review of technology and applications", *IEEE Sensors Journal*, vol. 12, no. 5, pp. 885–892, May 2012, ISSN: 1530-437X. DOI: [10.1109/JSEN.2011.2162060](https://doi.org/10.1109/JSEN.2011.2162060).
- [42] R. Kashyap, "The fiber fuse - from a curious effect to a critical issue: A 25th year retrospective", *Opt. Express*, vol. 21, no. 5, pp. 6422–6441, Mar. 2013. DOI: [10.1364/OE.21.006422](https://doi.org/10.1364/OE.21.006422).
- [43] A. Cusano, D. Paladino, and A. Iadicicco, "Microstructured fiber bragg gratings", *J. Lightwave Technol.*, vol. 27, no. 11, pp. 1663–1697, Jun. 2009.
- [44] X. Wen, T. Ning, C. Li, Z. Kang, J. Li, H. You, T. Feng, J. Zheng, and W. Jian, "Liquid level measurement by applying the Mach-Zehnder interferometer based on up-tapers", *Appl. Opt.*, vol. 53, no. 1, pp. 71–75, Jan. 2014. DOI: [10.1364/AO.53.000071](https://doi.org/10.1364/AO.53.000071).
- [45] L. Chen, C. Chan, K. Ni, P. Hu, T. Li, W. Wong, P. Balamurali, R. Menon, M. Shaillender, B. Neu, C. Poh, X. Dong, X. Ang, P. Zu, Z. Tou, and K. Leong, "Label-free fiber-optic interferometric immunosensors based on waist-enlarged fusion taper", *Sensors and Actuators B: Chemical*, vol. 178, pp. 176–184, 2013, ISSN: 0925-4005. DOI: <http://dx.doi.org/10.1016/j.snb.2012.12.071>.
- [46] H. Fu, X. Shu, A. Zhang, W. Liu, L. Zhang, S. He, and I. Bennion, "Implementation and characterization of liquid-level sensor based on a long-period fiber grating Mach-Zehnder interferometer", *IEEE Sensors Journal*, vol. 11, no. 11, pp. 2878–2882, Nov. 2011, ISSN: 1530-437X. DOI: [10.1109/JSEN.2011.2145416](https://doi.org/10.1109/JSEN.2011.2145416).
- [47] P. Lu, L. Men, K. Sooley, and Q. Chen, "Tapered fiber Mach-Zehnder interferometer for simultaneous measurement of refractive index and temperature", *Applied Physics Letters*, vol. 94, no. 13, p. 131110, 2009. DOI: [10.1063/1.3115029](https://doi.org/10.1063/1.3115029). eprint: <http://dx.doi.org/10.1063/1.3115029>.

- [48] J. Chen, B. Liu, and H. Zhang, "Review of fiber bragg grating sensor technology", *Frontiers of Optoelectronics in China*, vol. 4, no. 2, pp. 204–212, Jun. 2011, ISSN: 1674-4594. DOI: [10.1007/s12200-011-0130-4](https://doi.org/10.1007/s12200-011-0130-4).
- [49] Z. Tian and S.-H. Yam, "In-line single-mode optical fiber interferometric refractive index sensors", *J. Lightwave Technol.*, vol. 27, no. 13, pp. 2296–2306, Jul. 2009.
- [50] T. Wei, X. Lan, and H. Xiao, "Fiber in-line core-cladding-mode Mach-Zehnder interferometer fabricated by two-point CO₂ laser irradiations", *IEEE Photonics Technology Letters*, vol. 21, no. 10, pp. 669–671, May 2009, ISSN: 1041-1135. DOI: [10.1109/LPT.2009.2016116](https://doi.org/10.1109/LPT.2009.2016116).
- [51] Z. Tian, S. S. H. Yam, and H. P. Loock, "Single-mode fiber refractive index sensor based on core-offset attenuators", *IEEE Photonics Technology Letters*, vol. 20, no. 16, pp. 1387–1389, Aug. 2008, ISSN: 1041-1135. DOI: [10.1109/LPT.2008.926832](https://doi.org/10.1109/LPT.2008.926832).
- [52] J. Zhou, C. Liao, Y. Wang, G. Yin, X. Zhong, K. Yang, B. Sun, G. Wang, and Z. Li, "Simultaneous measurement of strain and temperature by employing fiber Mach-Zehnder interferometer", *Opt. Express*, vol. 22, no. 2, pp. 1680–1686, Jan. 2014. DOI: [10.1364/OE.22.001680](https://doi.org/10.1364/OE.22.001680).
- [53] X. Ben, L. Jian-Qing, L. Yi, and D. Xin-Yong, "A thin-core fiber modal interferometer for liquid-level sensing", *Chinese Physics Letters*, vol. 29, no. 10, p. 104209, 2012.
- [54] H. Y. Choi, M. J. Kim, and B. H. Lee, "All-fiber Mach-Zehnder type interferometers formed in photonic crystal fiber", *Opt. Express*, vol. 15, no. 9, pp. 5711–5720, Apr. 2007. DOI: [10.1364/OE.15.005711](https://doi.org/10.1364/OE.15.005711).
- [55] D.-W. Duan, Y.-J. Rao, L.-C. Xu, T. Zhu, D. Wu, and J. Yao, "In-fiber Mach-Zehnder interferometer formed by large lateral offset fusion splicing for gases refractive index measurement with high sensitivity", *Sensors and Actuators B: Chemical*, vol. 160, no. 1, pp. 1198–1202, 2011, ISSN: 0925-4005. DOI: <https://doi.org/10.1016/j.snb.2011.09.048>.
- [56] L. Zhao, L. Jiang, S. Wang, H. Xiao, Y. Lu, and H.-L. Tsai, "A high-quality Mach-Zehnder interferometer fiber sensor by femtosecond laser one-step processing", *Sensors*, vol. 11, no. 1, pp. 54–61, 2011, ISSN: 1424-8220. DOI: [10.3390/s110100054](https://doi.org/10.3390/s110100054).
- [57] M. Bass and V. N. Mahajan, *Hand book of optics*, 3rd ed. Mc Graw Hill, 2010, vol. 1, ISBN: 978-0-07-162925-6.

- [58] Q. Rong, X. Qiao, Y. Du, H. Sun, D. Feng, R. Wang, M. Hu, and Z. Feng, "In-fiber quasi-Michelson interferometer for liquid level measurement with a core-cladding-modes fiber end-face mirror", *Optics and Lasers in Engineering*, vol. 57, pp. 53–57, 2014, ISSN: 0143-8166. DOI: <http://dx.doi.org/10.1016/j.optlaseng.2013.12.010>.
- [59] H. C. B. Ximenes, R. L. Silva, C. E. S. Castellani, M. E. V. Segatto, and M. J. Pontes, "All-fibre transmission liquid level sensor based on core-cladding propagation modes interference", in *Microwave and Optoelectronics Conference (IMOC), 2015 SBMO/IEEE MTT-S International*, Nov. 2015, pp. 1–4. DOI: [10.1109/IMOC.2015.7369159](https://doi.org/10.1109/IMOC.2015.7369159).
- [60] Z. Zhao, M. Tang, S. Fu, S. Liu, H. Wei, Y. Cheng, W. Tong, P. P. Shum, and D. Liu, "All-solid multi-core fiber-based multipath Mach-Zehnder interferometer for temperature sensing", *Applied Physics B*, vol. 112, no. 4, pp. 491–497, Sep. 2013, ISSN: 1432-0649. DOI: [10.1007/s00340-013-5634-8](https://doi.org/10.1007/s00340-013-5634-8).
- [61] G. Hernández, *Fabry-perot interferometers*, 3. Cambridge University Press, 1988.
- [62] A. Yariv and P. Yeh, *Photonics: Optical electronics in modern communications*. Oxford University Press New York, 2007, vol. 6.
- [63] M. A. Putman, T. A. Berkoff, A. D. Kersey, J. S. Sirkis, D. D. Brennan, and E. J. Friebele, "In-line fiber étalon for strain measurement", *Opt. Lett.*, vol. 18, no. 22, pp. 1973–1975, Nov. 1993. DOI: [10.1364/OL.18.001973](https://doi.org/10.1364/OL.18.001973).
- [64] M. R. Islam, M. M. Ali, M.-H. Lai, K.-S. Lim, and H. Ahmad, "Chronology of Fabry-Perot interferometer fiber-optic sensors and their applications: A review", *Sensors*, vol. 14, no. 4, pp. 7451–7488, 2014, ISSN: 1424-8220. DOI: [10.3390/s140407451](https://doi.org/10.3390/s140407451).
- [65] Y.-J. Rao, "Recent progress in fiber-optic extrinsic fabry-perot interferometric sensors", *Optical Fiber Technology*, vol. 12, no. 3, pp. 227–237, 2006, ISSN: 1068-5200. DOI: <https://doi.org/10.1016/j.yofte.2006.03.004>.
- [66] X. Li, Y. Shao, Y. Yu, Y. Zhang, and S. Wei, "A highly sensitive fiber-optic fabry-perot interferometer based on internal reflection mirrors for refractive index measurement", *Sensors*, vol. 16, no. 6, 2016, ISSN: 1424-8220. DOI: [10.3390/s16060794](https://doi.org/10.3390/s16060794).
- [67] H. A. Haus, *Waves and fields in optoelectronics*. Prentice-Hall, 1984.
- [68] A. Othonos and K. Kalli, *Fiber bragg gratings: Fundamentals and applications in telecommunications and sensing*. Artech House, 1999.

- [69] C. Holmes, L. G. Carpenter, J. C. Gates, and P. G. R. Smith, "Miniaturization of bragg-multiplexed membrane transducers", *Journal of Micromechanics and Microengineering*, vol. 22, no. 2, p. 025 017, 2012.
- [70] C. Holmes, J. C. Gates, and P. Smith, "Integrated optical differential pressure transducers achieved using thin buckled silica membranes and direct uv written planar bragg gratings", *Sensors and Actuators A: Physical*, vol. 168, no. 1, pp. 14–21, 2011, ISSN: 0924-4247. DOI: <https://doi.org/10.1016/j.sna.2011.03.030>.
- [71] K. O. Hill and G. Meltz, "Fiber bragg grating technology fundamentals and overview", *Journal of lightwave technology*, vol. 15, no. 8, pp. 1263–1276, 1997.
- [72] O. Hassoon, M. Tarfoui, and A. El Malk, "Numerical simulation of fiber bragg grating spectrum for mode-i delamination detection", *World Academy of Science, Engineering and Technology, International Journal of Mechanical, Aerospace, Industrial, Mechatronic and Manufacturing Engineering*, vol. 9, no. 1, pp. 144–149, 2015.
- [73] A. Ikhlef, R. Hedara, and M. Chikh-Bled, "Uniform fiber bragg grating modeling and simulation used matrix transfer method", *Int. J. Comput. Sci*, vol. 9, pp. 368–374, 2012.
- [74] J. Huang, Z. Zhou, X. Wen, and D. Zhang, "A diaphragm-type fiber bragg grating pressure sensor with temperature compensation", *Measurement*, vol. 46, no. 3, pp. 1041–1046, 2013, ISSN: 0263-2241. DOI: <http://dx.doi.org/10.1016/j.measurement.2012.10.010>.
- [75] O. F. Ameen, M. H. Younus, M. Aziz, A. I. Azmi, R. R. Ibrahim, and S. Ghoshal, "Graphene diaphragm integrated FBG sensors for simultaneous measurement of water level and temperature", *Sensors and Actuators A: Physical*, vol. 252, pp. 225–232, 2016, ISSN: 0924-4247. DOI: <https://doi.org/10.1016/j.sna.2016.10.018>.
- [76] O. Ameen, M. Younus, M. Aziz, and R. Ibrahim, "Temperature and water level measurement of liquid in a tank using fiber bragg grating", *Jurnal Teknologi*, vol. 78, no. 3, pp. 261–265, Mar. 2016, ISSN: 0127-9696. DOI: [10.11113/jt.v78.7529](https://doi.org/10.11113/jt.v78.7529).
- [77] W. Yuan, A. Stefani, and O. Bang, "Tunable polymer fiber bragg grating (FBG) inscription: Fabrication of dual-FBG temperature compensated polymer optical fiber strain sensors", *IEEE Photonics Technology Letters*, vol. 24,

- no. 5, pp. 401–403, Mar. 2012, ISSN: 1041-1135. DOI: [10.1109/LPT.2011.2179927](https://doi.org/10.1109/LPT.2011.2179927).
- [78] G. Woyessa, J. K. M. Pedersen, A. Fasano, K. Nielsen, C. Markos, H. K. Rasmussen, and O. Bang, “Zeonex-pmma microstructured polymer optical FBGs for simultaneous humidity and temperature sensing”, *Opt. Lett.*, vol. 42, no. 6, pp. 1161–1164, Mar. 2017. DOI: [10.1364/OL.42.001161](https://doi.org/10.1364/OL.42.001161).
- [79] K. O. Hill, “Photosensitivity in optical fiber waveguides: From discovery to commercialization”, *IEEE Journal of Selected Topics in Quantum Electronics*, vol. 6, no. 6, pp. 1186–1189, Nov. 2000, ISSN: 1077-260X. DOI: [10.1109/2944.902166](https://doi.org/10.1109/2944.902166).
- [80] T.-H. Xia, A. P. Zhang, B. Gu, and J.-J. Zhu, “Fiber-optic refractive-index sensors based on transmissive and reflective thin-core fiber modal interferometers”, *Optics Communications*, vol. 283, no. 10, pp. 2136–2139, 2010, ISSN: 0030-4018. DOI: <http://dx.doi.org/10.1016/j.optcom.2010.01.031>.
- [81] C. E. S. Castellani, H. C. B. Ximenes, R. L. Silva, A. Frizzera-Neto, M. R. N. Ribeiro, and M. J. Pontes, “Multi-parameter interferometric sensor based on a reduced diameter core axial offsetted fiber”, *IEEE Photonics Technology Letters*, vol. 29, no. 2, pp. 239–242, Jan. 2017, ISSN: 1041-1135. DOI: [10.1109/LPT.2016.2637870](https://doi.org/10.1109/LPT.2016.2637870).
- [82] C. Li, T. Ning, C. Zhang, J. Li, C. Zhang, X. Wen, H. Lin, and L. Pei, “All-fiber multipath Mach-Zehnder interferometer based on a four-core fiber for sensing applications”, *Sensors and Actuators A: Physical*, vol. 248, pp. 148–154, 2016, ISSN: 0924-4247. DOI: <http://dx.doi.org/10.1016/j.sna.2016.07.031>.
- [83] H. Gong, H. Song, S. Zhang, K. Ni, and X. Dong, “An optical liquid level sensor based on polarization-maintaining fiber modal interferometer”, *Sensors and Actuators A: Physical*, vol. 205, pp. 204–207, 2014, ISSN: 0924-4247. DOI: <http://dx.doi.org/10.1016/j.sna.2013.11.012>.
- [84] J. Yang, L. Jiang, S. Wang, Q. Chen, B. Li, and H. Xiao, “Highly sensitive refractive index optical fiber sensors fabricated by a femtosecond laser”, *IEEE Photonics Journal*, vol. 3, no. 6, pp. 1189–1197, Dec. 2011, ISSN: 1943-0655. DOI: [10.1109/JPHOT.2011.2176535](https://doi.org/10.1109/JPHOT.2011.2176535).
- [85] J. M. Hsu, C. L. Lee, H. P. Chang, W. C. Shih, and C. M. Li, “Highly sensitive tapered fiber Mach-Zehnder interferometer for liquid level sensing”, *IEEE*

- Photonics Technology Letters*, vol. 25, no. 14, pp. 1354–1357, Jul. 2013, ISSN: 1041-1135. DOI: [10.1109/LPT.2013.2265738](https://doi.org/10.1109/LPT.2013.2265738).
- [86] X. Zhang, W. Peng, Z. Liu, and Z. Gong, “Fiber optic liquid level sensor based on integration of lever principle and optical interferometry”, *IEEE Photonics Journal*, vol. 6, no. 2, pp. 1–7, Apr. 2014, ISSN: 1943-0655. DOI: [10.1109/JPHOT.2014.2310208](https://doi.org/10.1109/JPHOT.2014.2310208).
- [87] C. Li, T. Ning, J. Li, C. Zhang, C. Zhang, H. Lin, and L. Pei, “Fiber-optic laser sensor based on all-fiber multipath Mach-Zehnder interferometer”, *IEEE Photonics Technology Letters*, vol. 28, no. 18, pp. 1908–1911, Sep. 2016, ISSN: 1041-1135. DOI: [10.1109/LPT.2016.2574943](https://doi.org/10.1109/LPT.2016.2574943).
- [88] M. R. Islam, M. M. Ali, M.-H. Lai, K.-S. Lim, and H. Ahmad, “Chronology of Fabry-Perot interferometer fiber-optic sensors and their applications: A review”, *Sensors*, vol. 14, no. 4, pp. 7451–7488, 2014, ISSN: 1424-8220. DOI: [10.3390/s140407451](https://doi.org/10.3390/s140407451).
- [89] Q. Yu and X. Zhou, “Pressure sensor based on the fiber-optic extrinsic Fabry-Perot interferometer”, *Photonic Sensors*, vol. 1, no. 1, pp. 72–83, Mar. 2011, ISSN: 2190-7439. DOI: [10.1007/s13320-010-0017-9](https://doi.org/10.1007/s13320-010-0017-9).
- [90] T. Lü and S. Yang, “Extrinsic Fabry-Perot cavity optical fiber liquid-level sensor”, *Appl. Opt.*, vol. 46, no. 18, pp. 3682–3687, Jun. 2007. DOI: [10.1364/AO.46.003682](https://doi.org/10.1364/AO.46.003682).
- [91] T. Lü, Z. Li, D. Xia, K. He, and G. Zhang, “Asymmetric Fabry-Perot fiber-optic pressure sensor for liquid-level measurement”, *Review of Scientific Instruments*, vol. 80, no. 3, p. 033 104, 2009. DOI: [10.1063/1.3093808](https://doi.org/10.1063/1.3093808). eprint: <http://dx.doi.org/10.1063/1.3093808>.
- [92] W. Wang and F. Li, “Large-range liquid level sensor based on an optical fibre extrinsic Fabry-Perot interferometer”, *Optics and Lasers in Engineering*, vol. 52, pp. 201–205, 2014, ISSN: 0143–8166. DOI: <http://dx.doi.org/10.1016/j.optlaseng.2013.06.009>.
- [93] Q. Wang, W. Wang, X. Jiang, and Q. Yu, “Diaphragm-based extrinsic Fabry-Perot interferometric optical fiber pressure sensor”, vol. 7656, 2010, pp. 7656V–8. DOI: [10.1117/12.866925](https://doi.org/10.1117/12.866925).
- [94] C.-W. Lai, Y.-L. Lo, J.-P. Yur, W.-F. Liu, and C.-H. Chuang, “Application of fabry-perot and fiber bragg grating pressure sensors to simultaneous measurement of liquid level and specific gravity”, *Measurement*, vol. 45, no. 3,

- pp. 469–473, 2012, ISSN: 0263-2241. DOI: <https://doi.org/10.1016/j.measurement.2011.10.026>.
- [95] C. W. Lai, Y. L. Lo, J. P. Yur, and C. H. Chuang, “Application of fiber bragg grating level sensor and Fabry-Perot pressure sensor to simultaneous measurement of liquid level and specific gravity”, *IEEE Sensors Journal*, vol. 12, no. 4, pp. 827–831, Apr. 2012, ISSN: 1530-437X. DOI: [10.1109/JSEN.2011.2161075](https://doi.org/10.1109/JSEN.2011.2161075).
- [96] M. de Fátima F. Domingues, T. de Brito Paixão, E. F. T. Mesquita, N. Alberto, A. R. Frias, R. A. S. Ferreira, H. Varum, P. F. da Costa Antunes, and P. S. de Brito André, “Liquid hydrostatic pressure optical sensor based on micro-cavity produced by the catastrophic fuse effect”, *IEEE Sensors Journal*, vol. 15, no. 10, pp. 5654–5658, Oct. 2015, ISSN: 1530-437X. DOI: [10.1109/JSEN.2015.2446534](https://doi.org/10.1109/JSEN.2015.2446534).
- [97] T.-W. Fu, Y.-J. Yang, J.-H. Lin, T.-Y. Yeh, P. Han, and C. L. Lee, “A polymer-coated hollow core fiber Fabry-Perot interferometer for sensing liquid level”, in *2016 21st OptoElectronics and Communications Conference (OECC) held jointly with 2016 International Conference on Photonics in Switching (PS)*, Jul. 2016, pp. 1–3.
- [98] A. D. Kersey, *Interrogation and multiplexing techniques for fiber Bragg grating strain sensors*, 1993. DOI: [10.1117/12.165923](https://doi.org/10.1117/12.165923).
- [99] H. Y. Chang, Y. C. Chang, H. J. Sheng, M. Y. Fu, W. F. Liu, and R. Kashyap, “An ultra-sensitive liquid-level indicator based on an etched chirped-fiber bragg grating”, *IEEE Photonics Technology Letters*, vol. 28, no. 3, pp. 268–271, Feb. 2016, ISSN: 1041-1135. DOI: [10.1109/LPT.2015.2494611](https://doi.org/10.1109/LPT.2015.2494611).
- [100] X. Dong, H. Zhang, B. Liu, and Y. Miao, “Tilted fiber bragg gratings: Principle and sensing applications”, *Photonic Sensors*, vol. 1, no. 1, pp. 6–30, Mar. 2011, ISSN: 2190-7439. DOI: [10.1007/s13320-010-0016-x](https://doi.org/10.1007/s13320-010-0016-x).
- [101] C. Mou, K. Zhou, Z. Yan, H. Fu, and L. Zhang, “Liquid level sensor based on an excessively tilted fibre grating”, *Optics Communications*, vol. 305, pp. 271–275, 2013, ISSN: 0030-4018. DOI: [http://dx.doi.org/10.1016/j.optcom.2013.05.019](https://doi.org/10.1016/j.optcom.2013.05.019).
- [102] S. Khaliq, S. W. James, and R. P. Tatam, “Fiber-optic liquid-level sensor using a long-period grating”, *Opt. Lett.*, vol. 26, no. 16, pp. 1224–1226, Aug. 2001. DOI: [10.1364/OL.26.001224](https://doi.org/10.1364/OL.26.001224). [Online]. Available: <http://ol.osa.org/abstract.cfm?URI=ol-26-16-1224>.

- [103] B. Yun, N. Chen, and Y. Cui, "Highly sensitive liquid-level sensor based on etched fiber bragg grating", *IEEE Photonics Technology Letters*, vol. 19, no. 21, pp. 1747–1749, Nov. 2007, ISSN: 1041-1135. DOI: [10.1109/LPT.2007.905093](https://doi.org/10.1109/LPT.2007.905093).
- [104] L. F. Ferreira, P. F. C. Antunes, F. Domingues, P. A. Silva, R. N. Nogueira, J. L. Pinto, P. S. André, and J. Fortes, "Monitorization of sea sand transport in coastal areas using optical fiber sensors", in *2009 IEEE Sensors*, Oct. 2009, pp. 146–150. DOI: [10.1109/ICSENS.2009.5398211](https://doi.org/10.1109/ICSENS.2009.5398211).
- [105] M. de Fátima F. Domingues, C. Rodriguez, J. Martins, N. Alberto, C. Marques, P. André, P. Antunes, and M. F. Ferreira, "Cost effective in line optical fiber fabry perot interferometric pressure sensor", in *Advanced Photonics 2017 (IPR, NOMA, Sensors, Networks, SPPCom, PS)*, Optical Society of America, 2017, JTU4A.15. DOI: [10.1364/IPRSN.2017.JTu4A.15](https://doi.org/10.1364/IPRSN.2017.JTu4A.15).
- [106] D. Song, J. Zou, Z. Wei, Z. Chen, and H. Cui, "Liquid-level sensor using a fiber bragg grating and carbon fiber composite diaphragm", *Optical Engineering*, vol. 50, no. 1, pp. 014401–5, 2011. DOI: [10.1117/1.3525286](https://doi.org/10.1117/1.3525286).
- [107] C. A. Marques, G.-D. Peng, and D. J. Webb, "Highly sensitive liquid level monitoring system utilizing polymer fiber bragg gratings", *Optics express*, vol. 23, no. 5, pp. 6058–6072, Mar. 2015. DOI: [10.1364/OE.23.006058](https://doi.org/10.1364/OE.23.006058).
- [108] Y. Zhao and Y. Liao, "Discrimination methods and demodulation techniques for fiber bragg grating sensors", *Optics and lasers in Engineering*, vol. 41, no. 1, pp. 1–18, 2004, ISSN: 0143-8166. DOI: [http://dx.doi.org/10.1016/S0143-8166\(02\)00117-3](http://dx.doi.org/10.1016/S0143-8166(02)00117-3).
- [109] J. E. Alfonso, L. G. Cárdenas, C. A. Triana, and M. V. Durán, "Design of an optical sensing interrogator using an edge filter scheme", in *2013 SBMO/IEEE MTT-S International Microwave Optoelectronics Conference (IMOC)*, Aug. 2013, pp. 1–5. DOI: [10.1109/IMOC.2013.6646509](https://doi.org/10.1109/IMOC.2013.6646509).
- [110] Q. Wu, Y. Semenova, A. Sun, P. Wang, and G. Farrell, "High resolution temperature insensitive interrogation technique for FBG sensors", *Optics & Laser Technology*, vol. 42, no. 4, pp. 653–656, 2010, ISSN: 0030-3992. DOI: <http://dx.doi.org/10.1016/j.optlastec.2009.11.005>.
- [111] J. S. Roncancio, N. González, C. C. Cano, and M. Varón, "Low cost optical interrogation system based on FBG sensors", in *2015 SBMO/IEEE MTT-S International Microwave and Optoelectronics Conference (IMOC)*, Nov. 2015, pp. 1–5. DOI: [10.1109/IMOC.2015.7369152](https://doi.org/10.1109/IMOC.2015.7369152).

- [112] J. Cui, Y. Hu, K. Feng, J. Li, and J. Tan, "FBG interrogation method with high resolution and response speed based on a reflective-matched FBG scheme", *Sensors*, vol. 15, no. 7, pp. 16 516–16 535, 2015, ISSN: 1424-8220. DOI: [10 . 3390/s150716516](https://doi.org/10.3390/s150716516).
- [113] L. Yan, Z. Wu, Z. Zhang, W. Pan, B. Luo, and P. Wang, "High-speed FBG-based fiber sensor networks for semidistributed strain measurements", *IEEE Photonics Journal*, vol. 5, no. 2, pp. 7 200 507–7 200 507, Apr. 2013, ISSN: 1943-0655. DOI: [10 . 1109/JPHOT.2013.2258143](https://doi.org/10.1109/JPHOT.2013.2258143).
- [114] T. Guo, H.-Y. Tam, and J. Albert, "Chirped and tilted fiber bragg grating edge filter for in-fiber sensor interrogation", in *CLEO: Science and Innovations*, Optical Society of America, 2011, CThL3. DOI: [10 . 1364 /CLEO_SI . 2011 . CThL3](https://doi.org/10.1364/CLEO_SI.2011.CThL3).
- [115] D. Srivastava, R. Bhatnagar, A. Kumar, and V. Parmar, "Intensity modulation using chirped fiber Bragg grating as an edge filter for temperature sensing", *Microwave and Optical Technology Letters*, vol. 56, no. 12, pp. 2913–2915, 2014, ISSN: 1098-2760. DOI: [10 . 1002/mop.28737](https://doi.org/10.1002/mop.28737).
- [116] R. Fallon, L. Zhang, L. Everall, J. Williams, and I. Bennion, "All-fibre optical sensing system: Bragg grating sensor interrogated by a long-period grating", *Measurement Science and Technology*, vol. 9, no. 12, p. 1969, 1998.
- [117] V. R. Mamidi, S. Kamineni, L. N. S. P. Ravinuthala, S. S. Madhuvarasu, V. R. Thumu, V. R. Pachava, and K. Putha, "Fiber bragg grating-based high temperature sensor and its low cost interrogation system with enhanced resolution", *Optica Applicata*, vol. 44, no. 2, pp. 299–308, 2014. DOI: [10 . 5277 / oa140210](https://doi.org/10.5277/oa140210).
- [118] V. R. Pachava, S. Kamineni, S. S. Madhuvarasu, K. Putha, and V. R. Mamidi, "FBG based high sensitive pressure sensor and its low-cost interrogation system with enhanced resolution", *Photonic Sensors*, vol. 5, no. 4, pp. 321–329, Dec. 2015, ISSN: 2190-7439. DOI: [10 . 1007/s13320-015-0259-7](https://doi.org/10.1007/s13320-015-0259-7).
- [119] U. Tiwari, K. Thyagarajan, M. R. Shenoy, and S. C. Jain, "Edf-based edge-filter interrogation scheme for FBG sensors", *IEEE Sensors Journal*, vol. 13, no. 4, pp. 1315–1319, Apr. 2013, ISSN: 1530-437X. DOI: [10 . 1109/JSEN.2012 . 2235064](https://doi.org/10.1109/JSEN.2012.2235064).

- [120] L. Wei, A. Khattak, C. Martz, and D. P. Zhou, "Tunable multimode fiber based filter and its application in cost-effective interrogation of fiber-optic temperature sensors", *IEEE Photonics Journal*, vol. 9, no. 2, pp. 1–8, Apr. 2017, ISSN: 1943-0655. DOI: [10.1109/JPHOT.2017.2679601](https://doi.org/10.1109/JPHOT.2017.2679601).
- [121] S.-F. Wang, T.-H. Chen, L. Tsai, C.-C. Huang, and C.-C. Chiang, "A FBG intensity modulation system combined with an optical whispering gallery mode edge filter", *Applied Sciences*, vol. 6, no. 4, 2016, ISSN: 2076-3417. DOI: [10.3390/app6040092](https://doi.org/10.3390/app6040092).
- [122] C. Liao, T. Hu, and D. Wang, "Optical fiber Fabry-Perot interferometer cavity fabricated by femtosecond laser micromachining and fusion splicing for refractive index sensing", *Optics express*, vol. 20, no. 20, pp. 22 813–22 818, 2012. DOI: [10.1364/OE.20.022813](https://doi.org/10.1364/OE.20.022813).
- [123] Y. Zhang, L. Yuan, X. Lan, A. Kaur, J. Huang, and H. Xiao, "High-temperature fiber-optic interferometric pressure sensor fabricated by femtosecond laser", *Optics letters*, vol. 38, no. 22, pp. 4609–4612, 2013. DOI: [10.1364/OL.38.004609](https://doi.org/10.1364/OL.38.004609).
- [124] G. M. Phillips, *Interpolation and approximation by polynomials*, 1st ed. Springer Science & Business Media, 2003, vol. 14, ISBN: 0387002154,9780387002156,9780387216829.
- [125] B. Gu, W. Qi, Y. Zhou, Z. Wu, P. P. Shum, and F. Luan, "Reflective liquid level sensor based on modes conversion in thin-core fiber incorporating tilted fiber bragg grating", *Opt. Express*, vol. 22, no. 10, pp. 11 834–11 839, May 2014. DOI: [10.1364/OE.22.011834](https://doi.org/10.1364/OE.22.011834).
- [126] M. Sun, Y. Jin, and X. Dong, "All-fiber Mach–Zehnder interferometer for liquid level measurement", *IEEE Sensors Journal*, vol. 15, no. 7, pp. 3984–3988, Jul. 2015, ISSN: 1530-437X. DOI: [10.1109/JSEN.2015.2406872](https://doi.org/10.1109/JSEN.2015.2406872).
- [127] P. S. André, M. Facão, A. M. Rocha, P. Antunes, and A. Martins, "Evaluation of the fuse effect propagation in networks infrastructures with different types of fibers", in *Proc. OFC/NFOEC*, Mar. 2010, pp. 1–3.
- [128] A. M. Rocha, P. F. da Costa Antunes, F. D. Maria de Fátima, M. Facao, and P. S. de Brito André, "Detection of fiber fuse effect using FBG sensors", *IEEE Sensors J.*, vol. 11, no. 6, pp. 1390–1394, 2011. DOI: [10.1109/JSEN.2010.2094183](https://doi.org/10.1109/JSEN.2010.2094183).
- [129] P. F. Antunes, M. F. F. Domingues, N. J. Alberto, and P. André, "Optical fiber microcavity strain sensors produced by the catastrophic fuse effect", *IEEE*

- Photonics Technology Letters*, vol. 26, no. 1, pp. 78–81, 2014. DOI: [10.1109/LPT.2013.2288930](https://doi.org/10.1109/LPT.2013.2288930).
- [130] P. André, A. Rocha, F. Domingues, and M. Fação, “Thermal effects in optical fibres”, in *Developments in Heat Transfer*, M. A. D. S. Bernardes, Ed., University Campus STeP Ri Slavka Krautzeka 83/A 51000 Rijeka, Croatia: InTech, 2011, ch. 1, pp. 1–21.
- [131] J.-l. Zhu, M. Wang, C.-d. Yang, and T.-t. Wang, “Miniature fiber Fabry-Perot sensors based on fusion splicing”, *Optoelectronics Letters*, vol. 9, no. 2, pp. 85–88, Mar. 2013, ISSN: 1993-5013. DOI: [10.1007/s11801-013-2432-9](https://doi.org/10.1007/s11801-013-2432-9).
- [132] J. M. Gere, *Mechanics of materials*, 6th ed. Thomson-Engineering, 2003, ISBN: 0-534-41793-0.
- [133] D. Tosi, “Advanced interrogation of fiber-optic bragg grating and Fabry-Perot sensors with klt analysis”, *Sensors*, vol. 15, no. 11, pp. 27 470–27 492, 2015.
- [134] P. André, F. Domingues, N. Alberto, C. Marques, and P. Antunes, “Recycling optical fibers for sensing”, in *SPIE Photonics Europe*, International Society for Optics and Photonics, vol. 9899, 2016, 98991F–5. DOI: [10.1117/12.2225245](https://doi.org/10.1117/12.2225245).
- [135] F. Sun, P. Tsai, G. Xiao, Z. Zhang, and D. Ban, “Free spectral range matched scanning interrogator”, in *Conference on Lasers and Electro-Optics*, Optical Society of America, 2007, JThD75.
- [136] C. A. R. Díaz, C. Leitão, C. A. Marques, M. F. Domingues, N. Alberto, M. J. Pontes, A. Frizera, M. R. N. Ribeiro, P. S. B. André, and P. F. C. Antunes, “Low-cost interrogation technique for dynamic measurements with FBG-based devices”, *Sensors*, vol. 17, no. 2414, 2017, ISSN: 1424-8220. DOI: [10.3390/s17102414](https://doi.org/10.3390/s17102414).
- [137] *Tlv354x 200-mhz, rail-to-rail i/o, cmos operational amplifiers for cost-sensitive systems*, TLV3541, TLV3542, TLV3544, Texas Instruments, Oct. 2016.
- [138] *K20 sub-family*, K20P144M100SF2V2, Rev. 3, Freescale, Jun. 2013.
- [139] *Ultracompact, 1.5 a thermoelectric cooler (tec) controller*, ADN8834, Rev. A, Analog Devices, Aug. 2015.